NAVAL POSTGRADUATE SCHOOL

MONTEREY, CALIFORNIA

DISSERTATION

EVOLUTION OF A WESTERN ARCTIC ICE-OCEAN
BOUNDARY LAYER AND MIXED LAYER ACROSS A
DEVELOPING THERMODYNAMICALLY FORCED
MARGINAL ICE ZONE

by

Shawn G. Gallaher

September 2016

Dissertation Supervisor: Timothy P. Stanton

THIS PAGE INTENTIONALLY LEFT BLANK

REPORT DOCUMENTATION PAGE		*Form Approved OMB No. 0704–0188*

Public reporting burden for this collection of information is estimated to average 1 hour per response, including the time for reviewing instruction, searching existing data sources, gathering and maintaining the data needed, and completing and reviewing the collection of information. Send comments regarding this burden estimate or any other aspect of this collection of information, including suggestions for reducing this burden, to Washington headquarters Services, Directorate for Information Operations and Reports, 1215 Jefferson Davis Highway, Suite 1204, Arlington, VA 22202-4302, and to the Office of Management and Budget, Paperwork Reduction Project (0704-0188) Washington, DC 20503.

1. AGENCY USE ONLY *(Leave blank)*	2. REPORT DATE September 2016	3. REPORT TYPE AND DATES COVERED Dissertation	
4. TITLE AND SUBTITLE EVOLUTION OF A WESTERN ARCTIC ICE-OCEAN BOUNDARY LAYER AND MIXED LAYER ACROSS A DEVELOPING THERMODYNAMICALLY FORCED MARGINAL ICE ZONE		5. FUNDING NUMBERS N0001414WX20089 N0001415WX01195	
6. AUTHOR(S) Shawn G. Gallaher			
7. PERFORMING ORGANIZATION NAME(S) AND ADDRESS(ES) Naval Postgraduate School Monterey, CA 93943-5000		8. PERFORMING ORGANIZATION REPORT NUMBER	
9. SPONSORING /MONITORING AGENCY NAME(S) AND ADDRESS(ES) N/A		10. SPONSORING / MONITORING AGENCY REPORT NUMBER	
11. SUPPLEMENTARY NOTES The views expressed in this thesis are those of the author and do not reflect the official policy or position of the Department of Defense or the U.S. Government. IRB Protocol number ____N/A____.			
12a. DISTRIBUTION / AVAILABILITY STATEMENT Approved for public release. Distribution is unlimited.		12b. DISTRIBUTION CODE	

13. ABSTRACT (maximum 200 words)

A comprehensive set of autonomous, ice-ocean measurements were collected across the Canada Basin to study the summer evolution of the ice-ocean boundary layer (IOBL) and ocean mixed layer (OML). Evaluation of local heat and freshwater balances and associated turbulent forcing reveals that melt ponds strongly influence the summer IOBL-OML evolution. The areal expansion and drainage of melt ponds resulted in a substantial increase in upper ocean heat storage (39 MJm^{-2}) and development of the summer mixed layer and near-surface temperature maximum (NSTM). 1-D boundary layer model results show that melt pond drainage provided sufficient buoyancy to the summer halocline to prevent subsequent wind events from mixing out the NSTM. Ice Camp observations captured the development of a second shallower NSTM in late summer; however, meltwater contributions were inadequate to sustain this feature when winds increased. In the marginal ice zone (MIZ), thermal heterogeneities in the upper ocean led to large ocean-to-ice heat fluxes (100–200 Wm^{-2}) and enhanced basal ice melt (3–6 cm-day^{-1}). Calculation of the upper ocean heat budget shows that the extensive area of deteriorating sea ice observed away from the ice edge during the 2014 season, termed the "thermodynamically forced MIZ," was driven primarily by local solar radiative heat input.
.

14. SUBJECT TERMS ice-ocean boundary layer processes, thermodynamic evolution of the upper ocean, ephemeral pycnocline, Local Turbulence Closure model, Thermodynamic Marginal Ice Zone, turbulent heat flux, heat partitioning; melt pond drainage, through-ice radiative transmission, near-surface temperature maximum, summer halocline, summer mixed layer			15. NUMBER OF PAGES 133
			16. PRICE CODE
17. SECURITY CLASSIFICATION OF REPORT Unclassified	18. SECURITY CLASSIFICATION OF THIS PAGE Unclassified	19. SECURITY CLASSIFICATION OF ABSTRACT Unclassified	20. LIMITATION OF ABSTRACT UU

NSN 7540-01-280-5500

Standard Form 298 (Rev. 2-89)
Prescribed by ANSI Std. 239-18

THIS PAGE INTENTIONALLY LEFT BLANK

EVOLUTION OF A WESTERN ARCTIC ICE-OCEAN BOUNDARY LAYER AND MIXED LAYER ACROSS A DEVELOPING THERMODYNAMICALLY FORCED MARGINAL ICE ZONE

Shawn G. Gallaher
Commander, United States Navy
B.S., University of North Carolina at Asheville, 1995
M.S., Naval Postgraduate School, 2002

Submitted in partial fulfillment of the
requirements for the degree of

DOCTOR OF PHILOSOPHY IN PHYSICAL OCEANOGRAPHY

from the

NAVAL POSTGRADUATE SCHOOL
September 2016

Approved by:　　Timothy P. Stanton　　　　William J. Shaw
　　　　　　　　Research Professor of　　　　Research Associate Professor
　　　　　　　　Oceanography　　　　　　　of Oceanography
　　　　　　　　Dissertation Committee Chair

　　　　　　　　Timour Radko　　　　　　　Andrew Roberts
　　　　　　　　Associate Professor of　　　　Research Assistant Professor
　　　　　　　　Oceanography　　　　　　　of Oceanography

　　　　　　　　Peter S. Guest
　　　　　　　　Research Professor of
　　　　　　　　Meteorology

Approved by:　　Peter C. Chu, Chair, Department of Oceanography

Approved by:　　Douglas Moses, Vice Provost of Academic Affairs

iii

THIS PAGE INTENTIONALLY LEFT BLANK

ABSTRACT

A comprehensive set of autonomous, ice-ocean measurements were collected across the Canada Basin to study the summer evolution of the ice-ocean boundary layer (IOBL) and ocean mixed layer (OML). Evaluation of local heat and freshwater balances and associated turbulent forcing reveals that melt ponds strongly influence the summer IOBL-OML evolution. The areal expansion and drainage of melt ponds resulted in a substantial increase in upper ocean heat storage (39 MJm^{-2}) and development of the summer mixed layer and near-surface temperature maximum (NSTM). 1-D boundary layer model results show that melt pond drainage provided sufficient buoyancy to the summer halocline to prevent subsequent wind events from mixing out the NSTM. Ice Camp observations captured the development of a second shallower NSTM in late summer; however, meltwater contributions were inadequate to sustain this feature when winds increased. In the marginal ice zone (MIZ), thermal heterogeneities in the upper ocean led to large ocean-to-ice heat fluxes (100–200 Wm^{-2}) and enhanced basal ice melt (3–6 $cm\text{-}day^{-1}$). Calculation of the upper ocean heat budget shows that the extensive area of deteriorating sea ice observed away from the ice edge during the 2014 season, termed the "thermodynamically forced MIZ," was driven primarily by local solar radiative heat input.

THIS PAGE INTENTIONALLY LEFT BLANK

TABLE OF CONTENTS

ix

THIS PAGE INTENTIONALLY LEFT BLANK

LIST OF FIGURES

LIST OF ACRONYMS AND ABBREVIATIONS

AOFB	Autonomous Ocean Flux Buoy
AWS	Automated Weather Station
C2/3/4	instrument cluster 2/3/4
CFSR	Climate Forecast System Reanalysis
IMB	Ice Mass Balance instrument
IOBL	ice-ocean boundary layer
ITP-V	Ice-Tethered Profiler with velocity
KOPRI	Korea Polar Research Institute
LTC	Local Turbulence Closure
MIZ	marginal ice zone
NSTM	near-surface temperature maximum
OML	ocean mixed layer
ONR	Office of Naval Research
SAR	synthetic aperture radar
SIZ	seasonal ice zone
sML	summer mixed layer
TKE	Turbulent Kinetic Energy
wML	winter mixed layer
YD	year day

MATHEMATICAL NOTATION AND CONSTANTS

A_{MP}	areal coverage of melt ponds on sea ice
A_{OWF}	areal coverage of open water
α	albedo
Δb	Ri_{bulk} buoyancy ($\Delta b = g\Delta\rho/\rho_{sw}$)
$C_{d(air-water(10m))}$	10 m air-water bulk drag coefficient constant (0.00125)
$C_{d(air-ice(2m))}$	2 m air-ice drag coefficient
$C_{d(ice-ocn(4.5m))}$	4.5 m ice-ocean drag coefficient

$C_{d(ice-ocn(6.5m))}$	6.5 m ice-ocean drag coefficient
δT	departure from freezing
F_H	ocean turbulent heat flux
F_{rad}	incident solar radiative heat flux
$F_{rad-ocn}$	total ocean solar radiative heat flux
$F_{rad-owf}$	through-lead solar radiative heat flux
$F_{rad-underice}$	through-ice solar radiative heat flux
F_S, $<w'S'>$	kinematic salt flux
FWC_{oml}	freshwater storage
g	gravitational acceleration constant ($9.81\ ms^{-2}$)
K	extinction coefficient
K_m	eddy viscosity
λ	turbulent mixing length
N^2	buoyancy frequency squared
ρ_o	C2 reference density constant ($1023.5\ kgm^{-3}$)
ρ_{sw}	C5 reference density constant ($1022\ kgm^{-3}$)
Ri	Gradient Richardson number
Ri_{bulk}	Bulk Richardson number
Ri_c	Critical bulk Richardson number constant (0.65)
Q^h	LTC model distributed solar heating
Q_{lh}	latent heat energy
Q_{oml}	ocean mixed layer heat storage
$Q_{rad-ocn}$	solar radiative heat energy into the ocean
S_{ref}	reference salinity constant (28.7 psu)
τ_o	ice-ocean interface stress
u_*	turbulent friction velocity
ΔV^2	Ri_{bulk} Shear squared
V_{ice}	ice speed
w_p	sea ice percolation velocity
$<w'b'>$	turbulent buoyancy flux
z_o	under-ice roughness length constant (0.029 m)

ACKNOWLEDGMENTS

THIS PAGE INTENTIONALLY LEFT BLANK

I.   INTRODUCTION

A.   CHANGES IN ARCTIC SEA ICE

Passive microwave satellite observations document a decline in Arctic sea ice extent during summer. Between 1979 and 1996, the average sea ice extent decreased by ~3% per decade; however, sea ice decline accelerated in the decade following this period with sea ice extent decreasing by more than 10% between 1997 and 2007 (Comiso et al. 2008). In fact, the National Snow and Ice Data Center (NSIDC) 2014 Melt Season in Review reported that the lowest minimum sea ice extents on satellite record occurred during the preceding ten year period. Furthermore, Arctic sea ice thickness and type are changing, as the perennial ice zones are transitioning to seasonal ice zones at a rate of approximately 15% per decade (Comiso 2012). Perennial ice, having survived several melt seasons, is generally thick and has been subjected to ridging/keeling deformation events. Seasonal ice, on the other hand, does not survive the melt season and cycles between the fall/winter freeze up and the spring/summer melt out each year. As the seasonal sea ice retreats during summer, a transition region composed of numerous small ice floes develops between the compact ice and open water known as the marginal ice zone. Given these changes in seasonal sea ice cover, more research is required to anticipate the future ice conditions of the Arctic Ocean during summer.

B.   SEASONAL ICE LOSS IN THE CANADA BASIN

The Western Arctic seasonal ice zone is expanding. The seasonal ice zone (SIZ) is defined as the region between maximum sea ice extent in late spring and minimum sea ice extent in late summer. The largest growth of this region is occurring in the Beaufort Sea and Canada Basin where the SIZ area has increased by 5.2% and 3.6% per decade, respectively, between 1968 and 2008 (Tivy et al. 2011). The lower areal extent of sea ice during summer has led to a 2–4% per year increase in radiative input to the ocean mixed layer between 1979 and 2005 (Perovich et al. 2007a). Identifying the processes that drive SIZ expansion requires an understanding of how this incoming solar radiation is absorbed and redistributed within the ice-ocean system. In this study, summer observations from

the 2014 Office of Naval Research (ONR) Marginal Ice Zone (MIZ) experiment in the Canada Basin are used to investigate the evolution of the turbulent ice-ocean boundary layer and mixed layer, and consequent effects on the partitioning of absorbed radiation in the upper ocean.

C.   MARGINAL ICE ZONE EXPERIMENT

To gain a better understanding of the expanding Western Arctic SIZ and associated MIZ, the 2014 ONR MIZ field program collected a wide-range of *in-situ* and satellite-based observations in the Canada Basin. Five ice-based, multi-instrument "clusters" were deployed and programmed to observe the SIZ as it transitioned from compact ice cover in spring to a fully developed MIZ in late summer. Each cluster contained a tightly grouped set of autonomous platforms to measure atmospheric conditions, surface solar radiation, ice thickness and temperature, ocean hydrographic profiles, and ice-ocean turbulent fluxes. Clusters 1–4 were deployed in early spring along the 135°W meridian from small air-supported ice camps to allow the ice edge and associate MIZ to retreat through the sensor clusters (Fig. 1.1). Cluster 5 (C5) was deployed in late summer, further north, at the edge of the seasonal ice zone (Fig. 1.1) from the Korea Polar Research Institute (KOPRI) icebreaker Araon (R/V Araon). Coincident with the C5 deployment, a joint MIZ-KOPRI Ice Camp was established between year days (YD(s)) 221 and 226 (9-14 August) to make intensive manned observations of the air-ice-ocean system. *In-situ* observations were complemented by remote sensing products, which were targeted over cluster locations to determine ice conditions on large spatial scales. For a full description of the ONR MIZ experiment, see Lee et al. (2012).

D.   NAVAL RELEVANCE AND DISSERTATION FOCUS

The expansion of open water in the Arctic Ocean has significant implications for the U.S. Navy. Summer opening of the Northern Sea Route permitted 44 vessels to transit the Arctic Ocean in 2012 and shipping traffic is expected to increase tenfold by 2025 (U.S. Navy 2014). Given these expected increases in international shipping, the U. S. Navy must expand their limited operations in the Arctic to preserve national security

interests and respond to future contingencies in the region. To prepare, the U.S. Navy requires a predictive capability of future sea ice conditions during summer. Development of this predictive capability demands an understanding of the complex interactions and feedbacks that create and expand the Western Arctic SIZ.

To address this requirement, a combination of MIZ field experiment observations and numerical model simulations were used in this dissertation to investigate the Arctic air-ice-ocean system. Specific emphasis is placed on the influences melting sea ice has on turbulent processes within the ice-ocean boundary layer and the resulting radiative heat partitioning within the upper ocean. Chapter II is based on Gallaher et al. (2016) and focuses on the temporal evolution of the ice-ocean boundary layer and ocean mixed layer in the Canada Basin as it progresses from compact ice to a fully developed marginal ice zone during the summer melt season. Chapter III is based on Gallaher et al. (2016, *Elementa* submitted) and investigates the formation of near-surface temperature maximums in early and late summer using a 1-D turbulent boundary layer model. Chapter IV provides a summary of the new contributions made to Arctic ice-ocean science and recommended areas of future work.

THIS PAGE INTENTIONALLY LEFT BLANK

II.   TEMPORAL EVOLUTION OF THE ICE-OCEAN BOUNDARY LAYER IN THE CANADA BASIN SEASONAL ICE ZONE

A.   INTRODUCTION

1.   The Summer Seasonal Ice Zone in the Canada Basin

Large vertical fluxes of heat and freshwater occur in the SIZ ice-ocean system during the spring-summer transition from full ice cover to open water. In the Canada Basin, defined as the area in Fig. 2.1a enclosed by the 3000 m isobath (Lane 1997), fundamental changes to the thermodynamics of this system start near the summer solstice as sunlight enters the ocean through thin ice and leads. When melt ponds are present, solar radiative fluxes through thick sea ice can be significant as well (Light et al. 2008). In addition to facilitating upper ocean heating, melt pond drainage is a significant source of freshwater to the upper ocean. Melt pond water drains to the upper ocean through leads, cracks, enlarged brine channels (Polashenski et al. 2012), or by percolation through the sea ice (Eicken et al. 2002). Freshwater from Mackenzie River runoff has also been shown to reach the Southern Canada Basin under certain conditions (Macdonald et al. 1999); however, significant contributions of heat and freshwater are generally confined further southeast to the Beaufort Sea/Shelf (Nghiem et al. 2014).

As summer progresses, radiative input to the ocean increases in response to larger open water areas. Basal ice melt accelerates during this period, adding further to the freshwater storage of the upper ocean. The combined inputs of melt pond drainage and basal ice melt can lead to surface fresh layers. Shallow fresh (2-4 psu) layers were observed in leads by Paulson and Pegau (2001) during the Surface Heat Budget of the Arctic Ocean (SHEBA) experiment with depths that extended to 1.2 m and temperatures as high as +1.6°C. These findings were confirmed by Autonomous Underwater Vehicle (AUV) observations, which showed surface trapped meltwater layers developed during low wind stress conditions and extended beyond the lead when ice drafts were less than the depth of the surface fresh layers (Hayes and Morison 2008).

Ultimately, the SIZ transitions into a marginal ice zone (MIZ) environment. There is no clear definition of the MIZ (Lee et al. 2012). Wadhams (2000) refers to the MIZ as a buffer between open water and the ice pack (ice concentration >70%) where open water processes affect the sea ice cover. These large spatial variations in sea ice coverage and composition generate correspondingly large spatial gradients in upper ocean properties.

2.   The Ice-Ocean Boundary Layer and Heat Redistribution

The redistribution of solar radiative energy absorbed in the upper ocean depends largely on the vertical extent of the turbulent ice-ocean boundary layer. The ice-ocean boundary layer (IOBL) is the actively mixing portion of the ocean mixed layer (OML) where turbulent eddies, generated by shear between wind-forced ice motion and the upper ocean, efficiently transport momentum, heat, and salt (McPhee 2008). During winter, the IOBL is neutrally to unstably stratified, allowing strong wind events to deepen the IOBL beyond the previously established winter mixed layer (wML) depth. This deepening can result in IOBL warming, as heat trapped within the winter pycnocline stratification is entrained upward (Jackson et al. 2012). In spring, IOBL heating is augmented by radiative input absorbed directly into the upper few meters of the ocean. The amount of basal ice melt generated from these IOBL heat gains is dependent on the magnitude of turbulent heat flux, which is driven by turbulent shear velocity (u_*) and the water temperature above freezing (δT) (McPhee 1992).

In summer, upper ocean stratification increases and the IOBL shoals as turbulent eddies expend kinetic energy to erode near-surface stratification, limiting the penetration of turbulent mixing. Boundary layer model results show that the IOBL depth can contract to <10 m during summer in response to basal ice melt (Toole et al. 2010; Vivier et al. 2016); however, the effects of melt pond drainage on the IOBL have been largely unexplored. Ultimately, the fresh melt layer develops into the summer mixed layer (sML) resulting in the dynamic decoupling of the underlying wML.

Observations from 2004 to 2009 show that freshening within the Canada Basin has led to stronger stratification and shallower mixing/mixed layers, with average sML and wML depths of 16 and 24 m, respectively (Toole et al. 2010). Thinning of the IOBL

permits greater heat storage within the residual wML, as that layer is able to directly absorb incoming radiation without turbulent vertical mixing. This forms a near-surface temperature maximum (NSTM) in the stratified water just below the sML (Jackson et al. 2010). Heat storage observed in the Canada Basin between 1993 and 2009 has increased by 0.5°C in the wML and by 1.5°C in the NSTM (Jackson et al. 2011). An increase in the heat just beneath the Canadian Basin wML, associated with the intrusion of Pacific Summer Water, was also observed between 2003 and 2013 (Timmermans et al. 2014); however, this heat source is effectively isolated from the ice-ocean interface due to strong stratification below the wML, which limits entrainment to a <5 m mixing zone (Shaw et al. 2009). Thus, solar radiation is the primary source of heat to the OML in the Canada Basin SIZ during summer and is predominantly distributed between latent heat losses and mixed layer heat storage gains (sink terms). The relative radiative input to these two sinks is dependent on the characteristics of the IOBL.

In the MIZ environment, the high spatial variability of ice/water fractions lead to extreme radiative and turbulent fluxes in and out of the IOBL-OML system. Substantial ocean-to-ice heat fluxes and basal ice melt can result when winds accelerate sea ice over adjacent open water areas. In the Eastern Arctic MIZ, McPhee et al. (1987) found that turbulent heat flux could be as high as 200 Wm^{-2}. During that same experiment, Morison et al. (1987) found that large increases in stratification, caused by high basal ice melt, could inhibit turbulent heat and momentum transfer with the ice-ocean interface. These two observations demonstrate the intricate interplay between momentum, heat, and buoyancy in a MIZ environment and the potential for highly variable melt rates.

3. Objectives

Previous large-scale studies of ice-ocean interactions in a MIZ have been focused on areas with significant ocean wave forcing in the Eastern Arctic or the Bering Sea, (MIZEX Group 1986), before the widespread summer ice retreat started to occur in the Canada Basin during the past decade (Perovich et al. 2012). Although the Canada Basin MIZ can be mechanically forced by summer cyclones (Zhang et al. 2013), the 2014 summer mean wind forcing was low (~4 ms^{-1}) and close to the climatological mean (~3.7

7

ms^{-1}, Stegall and Zhang 2012). Furthermore, the Canada Basin MIZ exists in an enclosed basin not subject to long period swell until late in the ice retreat (Thomson and Rogers 2014). These characteristics suggest thermodynamics are an important part of the late summer condition in this region.

In this study, we use data from the Office of Naval Research MIZ program to explore upper ocean thermodynamics as ice-deployed autonomous sensors drift on ice floes melting and mechanically deteriorating over the course of the summer season. Our specific objectives are to: 1) provide a high resolution overview of the IOBL-ML system as it changes during the summer; 2) identify unique regimes when OML heat storage and/or latent heat losses are enhanced by IOBL processes; 3) determine the processes that lead to sML and NSTM development; and 4) explore processes leading to the large area of deteriorating sea ice observed away from the sea ice edge during the 2014 summer (Fig. 2.1b). Investigation of these objectives will provide a better understanding of the ice-ocean system beneath the Western Arctic SIZ and determine the specific air-ice-ocean interactions contributing to increased seasonal melt in the Canada Basin.

B. AIR-ICE-OCEAN OBSERVATIONS

1. Autonomous Ocean Flux Buoy (AOFB)

Observations of near-interface turbulent processes were obtained from the Naval Postgraduate School Autonomous Ocean Flux Buoy 33 (AOFB 33) located at MIZ cluster 2 (C2). The primary AOFB sensor was the custom-built ocean flux package, consisting of (with accuracies) a 4-path, three-dimensional acoustic travel-time current meter (ACM) ($\pm$ 0.25 mm s^{-1} RMS noise level), a free-flushing inductive conductivity cell ($\pm$ 0.002 mS cm^{-1}), and a fast low-noise thermistor ($\pm$ 1 mC). These sensors were integrated to form a 0.001 m^{-3} sample volume located initially at ~2.5 m below the ice-ocean interface (~4.5 m depth) (see Shaw et al. 2008 for full description). Data were reported at 2-Hz and allowed the direct estimation of oceanic vertical turbulent fluxes of momentum, heat, and salt using eddy correlation methods. The MIZ program sampling strategy typically enabled the instruments to run for 35 min every 2 h. At 2 m above the sea ice surface, wind velocity (Vaisala Multi-weather Sensor) and incident shortwave

solar irradiance (Hukseflux SR03) were collected every 15 min. The pyranometer measured incident solar irradiance over a spectral range between 280 and 3000 nm.

2.   Ice-Tethered Profiler with Velocity (ITP-V)

Observations of upper ocean salinity and temperature were provided by the Ice-Tethered Profiler (Krishfield et al. 2008; Toole et al. 2011). The Ice-Tethered Profiler was also equipped with a velocity sensor (ITP-V) to measure ocean velocities and upper ocean turbulence (Cole et al. 2014). Data from ITP-V 77 was used extensively in this study and co-located on the same ice floe with AOFB 33 at C2. The ITP-V provided profiles of in-situ temperature, salinity, and velocity every 0.25-m, which were binned to 1-m, using a CTD profiler package crawling along a weighted wire connected to a surface buoy. The ITP-V profiled between 7 and 250 m every 3 h. In addition, at roughly 6 h intervals, time-series data were collected at a fixed depth of 6.5 m (initially ~4.5 m below the ice-ocean interface) for 20 min periods from which turbulent fluxes of heat, salt, and momentum were estimated using eddy correlation methods. A full description of velocity data processing is provided in Cole et al. (2015). In addition, at 6 m depth, a fixed SeaBird SBE-37 MicroCAT sensor sampled salinity and temperature every 15 min (Krishfield et al. 2008).

3.   Ice Mass Balance (IMB)

Ice Mass Balance (IMB) instruments were deployed to measure sea ice temperature and thickness. Two different IMB systems were used: 1) the Scottish Association for Marine Science (SAMS) IMB 17 (see Jackson et al. 2013), and 2) the Cold Regions Research and Engineering Laboratory (CRREL) IMB 2014C (see Polashenski et al. 2011). These IMBs were deployed at the center of C2 on ~1.8 m thick sea ice with ~0.25 m thick snow cover. In this study, an average of the SAMS and CRREL IMB bottom interface observations were used to represent C2 ice base changes. All other sea ice observations are from the SAMS IMB. Fig. 2.2 shows the relative vertical positions of the AOFB, ITP-V, and IMB sensors.

4.   Satellite Imagery

In addition to these *in-situ* observations, several satellite resources were exploited to characterize surface sea ice conditions. Two SAR products, provided by the Center for Southeastern Tropical Advanced Remote Sensing (CSTARS), were used in this study: 1) TerraSAR-X images at 8.3-m pixel spacing used to calculate local area open water fractions about MIZ C2, and 2) RadarSat-2 images at 100-m pixel spacing to provide general regional area ice conditions. Declassified visible grayscale satellite images at 1-m resolution were also used to characterize the local surface sea ice conditions and estimate melt pond coverage.

5.   Other Data Sources

Webcam images, wind estimates, and pyranometer data complete the data set. Webcam images were taken every 6 h from wave buoy (WB) 211 stationed ~25 m from AOFB 33 and ITP-V 77 to show surface conditions in C2's immediate vicinity. Failure of the AOFB 33 wind sensor between year day (YD) 198 and YD 231 required use of the RM Young anemometer mounted ~2 m above the sea ice surface on Automated Weather Station 2 (AWS 2). Additionally, hourly pyranometer observations from AWS 3 (C3) were linearly interpolated into the AOFB 33 shortwave radiation flux time series between YDs 196.8 and 201.8 due to a temporary power outage. Data from the Climate Forecast System Reanalysis (CFSR) were used to provide 10-m winds at ITP-V 70 for air-water stress calculations. CFSR is a fully coupled modeling system assimilating *in-situ* and satellite derived air, ice, and ocean observations into a 0.313 degree reanalysis model (for a full description, see Saha et al. 2010).

In combination, the AOFB, ITP-V, IMBs, and satellite imagery provide key information for understanding air-ice-ocean interactions during the MIZ field program. This includes sea ice conditions on multiple spatial scales; shortwave radiative fluxes; ocean turbulent fluxes at 4.5 m and 6.5 m; and ocean temperature, salinity, and velocity between 4.5 and 250 m at 1-m resolution. These combined data sets were captured during an ice floe drift track through the Canada Basin SIZ and provide the most complete

geophysical representation of the temporal evolution of the IOBL and OML under a developing MIZ ever observed by autonomous means.

The focus of the present study is the period 30 May to 19 August 2014 (YDs 150–231). Instruments at MIZ clusters 2–4 (C2-C4) returned data throughout this period as they traversed the Canada Basin (Fig. 2.1a). ITP-V 70, a prototype MIZ asset deployed 1 year earlier, exhausted the battery on its underwater sensor on YD 196. C2 returned the most complete data set and is thus the focal point of this work. Data from C3, C4, and ITP-V 70 are used for regional comparisons. Data from C1 was not used in this study because there was not an ITP-V or AOFB deployed at this site. C5 was not used because it was not deployed until late summer. Observations from the ice-deployed instruments included both temporal and spatial variability of upper ocean properties; the primary attention here is on the temporal evolution.

C.   METHODS

1.   Turbulent Mixing Layer and Summer Season Mixed Layers

High-resolution salinity and velocity data of the upper ocean provided a means of tracking the maximum vertical extent of shear generated turbulence identifying the IOBL. We estimated the IOBL using the bulk Richardson number (e.g., Large et al. 1994)

$$Ri_{bulk} = \frac{g(\Delta\rho)}{\rho_o[(\Delta u)^2 + (\Delta v)^2]}\Delta z, \qquad (2.1)$$

where $\Delta\rho$, Δu, and Δv are the changes in density and horizontal velocity across water thickness Δz, g is the gravitational acceleration (9.81 ms^{-2}), and ρ_o is the reference density (1023 kgm^{-3}). Δu and Δv were calculated by taking the difference of AOFB/ITP-V velocities relative to the ice velocity, assuming that the upper level of the slab motion in the bulk Richardson number calculation was the ice velocity. When Ri_{bulk} exceeded a critical value (Ri_c), IOBL deepening was assumed to terminate as the mixed layer shear becomes insufficient to overcome upper ocean density jumps (pycnoclines). The critical value for Ri_{bulk} is not well defined; however, a numerical model study conducted by Price

11

et al. (1986) showed $Ri_c = 0.65$ effectively diagnosed the depth of the ocean mixed layer. Thus, the IOBL for this study is considered all depths shallower than $Ri_{bulk} = 0.65$.

The wML and sML were used as control volumes for the local heat and freshwater budgets, therefore, clear definitions of each of these features were required. The wML resided above a deep (~35-45 m) winter pycnocline defined for this study by the 1023.5 kgm^{-3} isopycnal. This material surface was selected because it tracked the upper portion of the winter pycnocline throughout the time series. For the pycnocline at the base of the sML, we used the terminology and method of Jackson et al. (2010), which defines the summer halocline by the maximum water column buoyancy frequency

$$N^2_{max} = -\frac{g}{\rho_o}\frac{d\rho}{dz}_{max} , \qquad (2.2)$$

where $d\rho/dz$ is the potential density gradient. However, because density gradients at the base of the sML during initial development were weak, we modified the definition from the water column N^2 maximum to the N^2 maximum above the deep winter pycnocline following development of the NSTM. The NSTM is defined by the following criteria: 1) a near-surface temperature maximum that is at least 0.1 °C above a deeper temperature minimum, 2) a salinity lower than 31 psu, and 3) at least a 0.2 °C temperature above freezing (Jackson et al. 2010). The wML, sML, and NSTM are overlaid in Fig. 2.8c and show their relative vertical extent.

2.   Open Water Fraction and Melt Pond Coverage

TerraSAR-X images collected over C2 were used to estimate the areal fraction of open water (A_{OWF}). For each image, a combination of median, Gaussian, and bilateral filters (Tomasi and Manduchi 1998) were applied to reduce speckle noise in the raw Synthetic Aperture Radar (SAR) images, and A_{OWF} was calculated using a parametric kernel graph cuts algorithm (Salah et al. 2011). Twenty-five images were processed for the focus period, five of which are presented in Fig. 2.3. Four images between YDs 217 and 226 were excluded due to large variability in derived A_{OWF}. Comparisons to 1-m visible imagery suggest that ice area may have been over-represented in the lower

12

resolution SAR imagery when extensive areas of small ice floes and brash were present. Estimates of A_{OWF} from the remaining 21 images were linearly interpolated between observations across the SAR image time-series (YDs 150–232).

The areal coverage of melt ponds (A_{MP}) on ice floes was approximated using high-resolution (1-m) visible satellite imagery. Since open water, melt ponds, and sea ice had large differences in visible wavelength albedo, a histogram of gray scale pixel intensities generally produced tri-modal distributions. Thresholds can be applied in the valleys of these three peaks to designate pixel cells into one of the three categories (Kim et al. 2013). Four 25 km^2 images were selected based on image availability, proximity to C2, and cloud contamination (Fig. 2.4). The image taken on YD 175 (Fig. 2.4a) was the only image not acquired directly over C2 (~35 km north), but was the only image available near the time of maximum melt pond coverage. Estimates of A_{MP} were linearly interpolated between observations across the visible image time-series (YDs 149–223). A_{MP} is assumed constant between YDs 223 and 231 due to the lack of visible imagery after YD 223.

3.   Mixed Layer Heat and Freshwater Budgets

A simple 1-D heat budget was calculated, at ~3-h intervals, to determine how ocean absorbed solar radiation (source term) was distributed between OML heat storage (sink term 1) and latent heat losses (sink term 2). Radiative input into the ocean was not directly observed during this study, thus, a combination of air-side shortwave radiation observations, satellite imagery, and published parameterizations were used to estimate solar radiation entering the upper ocean. Ocean radiative fluxes have an open-water and under-ice component. The open-water component was estimated by (e.g., Stanton et al. 2012)

$$F_{rad-owf} = F_{rad} A_{OWF} (1 - \alpha_{ocn}), \qquad (2.3)$$

13

where F_{rad} is the observed downwelling irradiance from the AOFB, A_{OWF} is the fraction of open water derived from SAR imagery, and α_{ocn} is the albedo of open water (0.066) (Pegau and Paulson 2001).

To calculate the under-ice component of ocean radiative flux, we used the Light et al. (2008) sea ice shortwave downwelling flux equation scaled by the ice cover fraction $(1 - A_{OWF})$ and the optical properties of the sea ice surface conditions to form:

$$F(z_{ice})_{rad-underice} = F_{rad}(1 - \mathrm{A_{OWF}})[\mathrm{A_{ice}}(1 - \alpha_{ice})\mathrm{I}_{ice} + \mathrm{A_{MP}}(1 - \alpha_{MP})\mathrm{I}_{MP}]. \quad (2.4)$$

A_{ice} is the fraction of total ice coverage that is unponded $(1 - A_{MP})$ and A_{MP} is the fraction of total ice coverage that is ponded derived from visible satellite imagery. The α_{ice} and α_{MP} terms are the albedos, and the I_{ice} and I_{MP} terms are the attenuation equations ($I = I_o exp(-Kz_{ice})$) for melting and ponded multi-year ice (predominate ice type at C2). For this study, the applicable Table 4 values from Light et al. (2008) were used to estimate albedo (α), surface transmission parameter (I_o), and extinction coefficient (K). Local sea ice thickness (z_{ice}) was derived from IMB observations. α, I, and K also have distinct values for the visible and near-infrared portions of the incoming solar energy. The pyranometer sampled both the visible and near-infrared spectra together. Hence, the solar data were partitioned as 0.7 (visible) and 0.3 (near-infrared), consistent with the approximately two-thirds to three-quarters of solar energy being in the visible range (Perovich and Polashenski 2012). Of note, $F_{rad-underice}$ was set to zero when dry snow was suspected to cover the sea ice (YDs 150–156).

The sum of Eqns. (2.3) and (2.4) provides the solar radiative source term for the heat balance calculation and is referred to as the total ocean radiative flux ($F_{rad-ocn}$), or integrated in time, the total ocean radiative energy ($Q_{rad-ocn}$). The sea ice characterization afforded by the MIZ space-based assets was remarkable and resulted in a robust $F_{rad-ocn}$ estimate. This method requires that we assume the A_{OWF} and A_{MP} determined at the larger spatial scales, 45 and 5 km square respectively, were representative of the solar radiative influence near C2. The author acknowledges that this local scale may not always be

appropriate for all conditions; however, comparisons of A_{OWF} to smaller area TerraSAR-X and 1-m visible satellite imagery show similar A_{OWF} results down to ~10 km square (not shown).

For the first sink term, OML heat storage per m^2 was calculated from the amalgamated fixed-depth AOFB and MicroCAT CTD, and profiled ITP data by

$$Q_{oml} = c_p \rho_o \int_{z_2}^{z_1} \delta\mathrm{T(s,p)} dz,$$ (2.5)

where c_p is the specific heat capacity of sea water (~3986 J kg^{-1}C^{-1}), and δT is the *in-situ* temperature above freezing ($T - T_f$). Given that T_f changes with salinity, a reference salinity (S_{ref}) of 28.7 psu was assumed and yields a freezing temperature of ~-1.57 °C (UNESCO 1983). S_{ref} is the approximate average salinity along the 1023.5 kgm^{-3} isopycnal (winter pycnocline). Use of a reference freezing temperature allowed for a heat as opposed to a temperature budget. Comparison of the heat storage results between local and referenced freezing temperatures yielded a difference of ~6 MJm^{-2} over the study period. All salinity and temperature data from the AOFB and ITP profiler were calibrated to the MicroCAT CTD. Just 31 of 639 profiles were missing from the ITP-V profiling CTD, thus data were linearly interpolated across all time gaps. The upper level of integration (z_1) is the shallowest observed temperature and salinity depth (4.5 m) and the lower limit (z_2) is the material surface defined by the winter pycnocline. After the sML forms around YD 192, z_2 becomes the base of the sML identified by the summer halocline depth. For evaluation of the wML during this period, the base of sML becomes z_1 and the winter pycnocline becomes z_2. The OML is defined as the entire ocean volume down to the winter pycnocline. The OML before YD 192 is equal to the wML; however, the OML after YD 192 is the combined sML and wML.

For the second sink term, latent heat losses per m^2 from the IMB data were calculated by

$$Q_{lh} = q_{lh} \rho_{ice} \Delta z_{ice},$$ (2.6)

15

where q_{lh} is the latent heat of fusion for sea ice (3×10^5 J kg^{-1}), ρ_{ice} is the density of sea ice (910 kg m^{-3}), and Δz_{ice} is the change in the bottom sea ice interface in m^3/m^2.

The flux form of the sink terms are presented in the results and were determined by dividing Eqns. (2.5) and (2.6) by the analysis time interval (Δt=~3 h). Also, we assume upper ocean heat changes due to the long-wave radiation balance, air-water latent heat exchange, and air-water sensible heat exchange are small due to the high areal fraction of sea ice and near equal air-water temperatures observed during the study (Persson et al. 2002).

Similar to the heat budget, a 1-D freshwater budget was calculated comparing sea ice melt (source) to OML freshwater storage (sink). The freshwater source term (FWC_{ice}) was determined from the combined observed surface and basal sea ice melt calculated by $(\rho_{ice}/\rho_{fw})\Delta z_{ice}$, where ρ_{fw} is the density of freshwater (1000 kgm^{-3}). For snow melt, ρ_{ice} is replaced by ρ_{snow} (360 kgm^{-3}).

To calculate OML freshwater storage per m^2, we used the Proshutinsky et al. (2009) freshwater content equation

$$FWC_{oml} = \int_{z_2}^{z_1} \frac{[S_{ref} - S(z)]}{S_{ref}} dz, \tag{2.7}$$

where S_{ref} is the reference salinity (28.7 psu), and $S(z)$ is the salinity at water depth z. To partition FWC_{oml} into sML and wML components, we use the same upper and lower integration limits as in Eqn. (2.5). The flux form of the freshwater source and sink terms will also be presented in the results section.

In summary, this simple 1-D approach tests the local budgets in order to identify trends in ocean heating and freshening during the summer evolution. We then attempt to associate these trends with changes in the IOBL, wML, sML, and/or the sea ice. Significant residuals of heat and freshwater will be assumed due to radiative flux estimate

errors, lateral advection, or potentially vertical diffusion from below the OML material surface.

4. Turbulent Exchange of Heat, Salt, and Momentum

To identify active and inactive periods of mixing, heat exchange, and salt exchange with the ice-ocean interface, turbulent fluxes of momentum, heat, and salt were calculated from the fixed-depth flux packages using eddy correlation methods. Spectral covariance estimates of perturbation pairs were determined across a selected frequency range to avoid contamination from surface gravity waves, package vibration, and potentially internal gravity waves. For the AOFB, a cross spectral analysis was performed on each 35-min sample. Flux estimates $(<w'x'>)$ were calculated by summing the covariance in the spectral bins spanning the outer scale turbulent eddy frequencies by (Shaw and Trowbridge 2001)

$$\langle w'x' \rangle \Big|_{f_1}^{f_2} = \int_{f_1}^{f_2} Co_{wx}(f)df, \qquad (2.8)$$

where Co is the cospectrum, w is the vertical velocity perturbation, x is the vector (u, v) or scalar (T, S) perturbation variables, and f_1 and f_2 are the low- and high-frequency limits of the energy-containing range (0.0029-0.12 Hz in this study). For the ITP-V, fluxes were calculated by averaging covariance results over each 20-min sample, after each variable was detrended and low-pass filtered at 4 s.

Turbulent fluxes of heat and salt in the vertical were then given by

$$F_H = c_p \rho_o \langle w'T' \rangle, \qquad (2.9)$$

$$F_s = \langle w'S' \rangle, \qquad (2.10)$$

where $<w'T'>$ and $<w'S'>$ are the kinematic heat and salt fluxes from Eqn. (2.8) respectively. Freshwater flux at 4.5 m was derived from $<w'S'>_{(4.5m)}$ observations and was calculated using a modified form of Eqn. (2.7) and the local salinity for S_{ref}. The

magnitude of the turbulent momentum flux was represented by the friction velocity (e.g., McPhee 2008)

$$u_* = (\langle u'w' \rangle^2 + \langle v'w' \rangle^2)^{0.25}, \tag{2.11}$$

where $<u'w'>$ and $<v'w'>$ represent the vertical transport of horizontal momentum.

Two additional quantities near the ice-ocean interface were considered. To determine periods when sufficient conditions for shear generated instabilities existed, the gradient Richardson number ($Ri = N^2/S^2$, where S is the shear) was calculated between the AOFB and ITP-V at 5.5 m. Secondly, the ratio of ice speed to friction velocity (V_{ice}/u_*) was calculated to evaluate the momentum coupling between the ice-ocean interface and the 4.5 m layer. Calculation of the drag coefficient was considered but not included, because observations at the 4.5 m level were not always indicative of the ocean/ice-interface stresses owing to near-surface stratification.

The term "ephemeral" pycnocline will be used to denote stratification present at the base of a near-surface fresh layer. Although salinity was not observed between the sea ice and the 4.5 m sensor at this site, we attempt to demonstrate the existence of the ephemeral pycnocline from estimates of turbulent parameters and freshwater storage just below this layer, and from temperature data inside the layer.

5. Sea Ice Divergence

Open water areas can expand quickly in the SIZ during summer. To distinguish periods when this expansion was driven primarily by wind conditions and not lateral/basal ice melt, surface stresses (τ_{total}) were calculated from *in-situ* observations. These surface stresses were partitioned between air-ice and ice-water interfaces following Yang (2006)

$$\tau_{total} = (1 - A_{OWF})\tau_{ice-water} + A_{OWF}\tau_{air-water}, \tag{2.12}$$

where A_{OWF} is the open water fraction at C2, and $\tau_{ice\text{-}water}$ and $\tau_{air\text{-}water}$ are the ice-water and air-water stresses. Interface stresses (τ) were calculated by using the drag law relationship

$$\tau = C_d \left| U \right| U, \tag{2.13}$$

where C_d is the drag coefficient and U is the flow speed relative to the fluid. For $\tau_{air\text{-}water}$, U was estimated from the observed 2 m winds at each MIZ cluster corrected to 10 m (Hsu et al. 1994). For $\tau_{ice\text{-}water}$, U was calculated by differencing the ice speed (U_{ice}) from the 6.5 m ocean velocity ($U_{6.5m}$). A constant $C_{d(air\text{-}water(10m))}$ of 0.00125 (Yang 2006) was assumed for air-water stresses and a time-varying $C_{d(ice\text{-}ocn(6.5m))}$ was used for the ice-water stresses calculated by

$$C_{d\,(ice-ocn(6.5m))} = \frac{u_*^2}{\bar{U}^2}, \tag{2.14}$$

where u_* is the 6.5 m friction velocity observation from the ITP-V, and $\bar{U}$ is the 1 day mean ice-water flow speed ($U_{ice} - U_{6.5m}$). To ensure turbulence was fully developed at the 6.5 m depth, only u_* values greater than 0.004 ms^{-1} were used. Wind, ocean, and ice velocities were taken from the AOFBs, ITP-Vs, and AWSs deployed at clusters 2–4 and ITP-V 70. Ocean velocities were assumed zero when current data were not available. Winds were not observed at the ITP-V 70 site, thus 10 m winds from the Climate Forecast System Reanalysis were used. After surface stresses were calculated for each site, the wind stress curl was determined by

$$curl(\tau_o) = \frac{\partial}{\partial x}(\tau_{oy}) - \frac{\partial}{\partial y}(\tau_{ox}), \tag{2.15}$$

where τ_{ox} and τ_{oy} are the horizontal components of the interface stresses. The author acknowledges that the orientation of MIZ instruments (Fig. 2.1a) prevents calculation of wind stress curl directly over MIZ C2, but the calculation should provide a sufficient

regional characterization of the mode (convergent (<0) / divergent (>0)) and magnitude of the wind-forced sea ice divergence.

D.   RESULTS

1.   Stages of the Summer Evolution

The observations reported here cover a three-month period spanning the summer evolution of the coupled ocean-ice-atmosphere system, during which the ice cover surrounding C2 changed from compact ice (winter conditions) to a fully developed MIZ (summer conditions). Although C2 drifted approximately 500 km in total across the Canadian Basin, the period from 29 June to 3 August (YDs 180–215) was dominated by largely circuitous ice motion (Fig. 2.1a, zoomed area). During this period, the instrument array remained within a relatively tight 100 km square region near the middle of the Canada Basin away from bathymetric boundaries. This period of the time series is important because the influence of spatial gradients were presumably limited; nevertheless, substantial changes occurred in the IOBL and OML.

We divide the summer evolution into four stages in Figs. 2.6–2.10: Stage I, 30 May to 21 June (YDs 150–172), is the Early Summer Ice-Ocean Boundary Layer; Stage II, 22 June to 10 July (YDs 173–191), is Mixed Layer Freshening and Warming; Stage III, 11–27 July (YDs 192–208), is Development of the Summer Mixed Layer and NSTM; and Stage IV, 28 July to 19 August (YDs 209–231), is the Marginal Ice Zone Ice-Ocean Boundary Layer. These stages were established based on the following conditions/events:

1.   Stage I: Ocean mixed layer initial condition representative of spring conditions;

2.   Stage I to II transition: Concurrent increases in OML heat (Fig. 2.9a) and freshwater storage (Fig. 2.10a), and decrease in IOBL depth (Fig. 2.7c);

3.   Stage II to III transition: Formation of the sML and NSTM (Fig. 2.8c); and

4.   Stage III to IV transition: C2 entering the MIZ defined as the buffer zone between compact ice (ice concentration $> 70\%$) and open water ($A_{OWF} > 0.3$, Fig. 2.6b).

20

In the following subsections, an overview of sea ice conditions and solar radiative forcing (Fig. 2.6); IOBL processes (Fig. 2.7) and ice-ocean properties (Fig. 2.8); local heat balances (Fig. 2.9); and local freshwater balances (Fig. 2.10) will be provided in succession for each stage.

a.   Stage I: The Early Summer Ice-Ocean Boundary Layer

Throughout Stage I, there was very little open water, but the surface condition of the sea ice evolved substantially. Visible satellite imagery and buoy webcam images from YD 157, (Figs. 2.5a and 2.5c) observed snow/ice cover with no visible surface meltwater. By the end of this stage, Figs. 2.5b and 2.5d confirm the development of melt ponds at C2. Although incoming solar irradiance was at its maximum during Stage I (Fig. 2.6a), radiative flux to the ocean was small (12 Wm^{-2}) with most entering through what little open water existed.

The IOBL exhibited near-neutral conditions with deep turbulent penetration (Fig. 2.7c), strong air-ice-ocean momentum coupling (Fig. 2.7d), and weak wML stratification (Fig. 2.8d). The wML was "winter-like" with temperatures close to the *in-situ* freezing point (Fig. 2.8b), a thickness of about 40 m, and underlain by a strong winter pycnocline (Fig. 2.8d). The depth of the winter pycnocline suggests that heat associated with the previous summer NSTM had been completely ventilated over the winter.

The local heat budget indicated good agreement between radiative heat input (Fig. 2.9a, black line) and the sum of latent heat losses (blue area) and wML heat storage (gray area). Stage-averaged turbulent heat fluxes at 4.5 m were low (3 Wm^{-2}), with only one notable event around YD 169 (45 Wm^{-2}, Fig 2.9d) associated with a 10 ms^{-1} wind maximum (Fig. 2.7a). A series of deep entrainment events occurred as a result, as evidenced by the nearly 40 m maximum turbulent penetration depth (Fig. 2.7c) and observed feathering of heat across the winter pycnocline (Fig. 2.8b). Limited basal melt occurred (1-2 cm) demonstrating the challenge of heat exchange across a deep winter mixed layer during the early melt season. Following the YD 169 wind event, a mesoscale front or eddy feature shoaled and weakened the winter pycnocline through the end of the stage (Fig. 2.8d). This mesoscale activity caused a temporary imbalance in the wML

freshwater budget between YDs 170 and 175 (Fig. 2.10a). Sea ice total FW fluxes were low (<1 cm^3/cm^2 day^{-1}, Fig. 2.10d); however, surface melting increased substantially toward the end of the stage (Fig. 2.10c, light blue area), consistent with melt pond formation.

b.   Stage II: Mixed Layer Freshening and Warming

Melt pond development continued during Stage II, leading to large increases in pond areal extent. Melt pond coverage, as determined from remote satellite imagery, exceeded 60% by YD 175 (Fig. 2.6b). Webcam images indicate that melt pond coverage peaked on YD 178 (Fig. 2.11a), and they subsequently confirmed melt pond drainage, with all visible surface ponds emptying by YD 187 (Fig. 2.11b). Visible satellite imagery taken on YDs 182 and 196 further document the drainage of melt pond that occurred in the vicinity of C2 (Fig. 2.11c and 2.11d). In response to expanded melt pond coverage, stage-averaged ocean radiative flux increased by 19 Wm^{-2} due largely to increases in the through-ice component (Fig. 2.6d, blue area). This increase in ocean radiative flux occurred irrespective of the ~50 Wm^{-2} decrease in stage-average solar irradiance and low A_{OWF}. This demonstrates how areal expansion of surface melt ponding significantly impacts solar input into the early summer OML.

The IOBL changed substantially during Stage II. The maximum depth of the IOBL, as estimated by Eqn. (2.1), shoaled by almost 20 m compared to the previous stage (Fig. 2.7c). This shoaling is probably underestimated, because changes in buoyancy above 4.5 m were not accounted for. These changes in IOBL depth occurred even though wind forcing was largely unchanged from Stage I and indicate that near-surface stratification was strongly affecting shear-related turbulent mixing. Figs. 2.7b and 2.7d confirm this is the case with a noticeable decrease in u_* and increase of V_{ice}/u_* and Ri, particularly after YD 185. The combined surface (46 cm of snow and ice) and basal (15 cm) melt observed during the stage (Fig. 2.8a) suggests that the source of this stratification was meltwater from the sea ice. Although deepening events below the 4.5 m sensor did occur, e.g., YDs 176, 180, and 184 (Fig. 2.7c), no significant pycnocline developed indicating that shallow stratification was periodically mixed out, but rapidly

re-established after the surface stresses reduced. Few observations were available above 4.5 m to verify the increase in stratification near the surface; however, warm water (-0.6° C) was observed just beneath the sea ice in the IMB beginning on YD 189 (Fig. 2.8a). Coincident with this observation was an increase in 5.5 m Ri values (Fig. 2.7d) indicating stronger stratification near the surface. The timing of this event follows significant melt pond drainage on the sea ice surface and suggests this warm water signal was likely a melt pond drainage event to the OML via a nearby crack or flaw in the sea ice (Polashenski et al. 2012). The NSTM formed near the same date and further suggests the presence of a near-surface (ephemeral) pycnocline.

Heat budget comparisons in Fig. 2.9a show well-matched increases in both the source and sink terms during Stage II. Heat storage and latent heat fluxes were nearly equal during the stage (Fig. 2.9c), resulting in heat equivalent increases of 39 and 41 MJm^{-2} respectively. A rough estimate of the heat content contributed by drained melt pond water shows that this was not a significant source of heat (0.3 m x 1000kgm^{-3} x 4000Jkg^{-1}°C^{-1} x 1°C = ~1 MJm^{-2}) to these sink terms, implying the absorption of through-ice solar radiation was the primary heat source. Interestingly, turbulent heat flux measurements at 4.5 and 6.5 m (Fig. 2.9d) were well below the latent heat losses observed. This suggests that most of the heat responsible for the observed basal ice melt came from solar radiation absorbed above 4.5 m depth and that mixing within this thin surface layer was frequently active. Overall, sinks exceeded source by 18% through the first two stages. Comparison of the combined sink terms in Fig. 2.9d (gray line) shows this imbalance occurred while melt ponds were present around the C2 sensors (YDs 175–187) indicating through-ice radiative flux (Eqn. (2.4)) was likely underestimated during this period. This may have been the consequence of IMB sensors being deployed preferentially in thick ice (for survivability) resulting in z_{ice} in Eqn. (2.4) being greater than the larger area mean ice thickness.

Consistent with the melt pond drainage observed, freshwater flux from the sea ice surface was the highest of any stage (Fig. 2.10c). Turbulent freshwater fluxes at 4.5 m show that these increases to wML freshwater storage were well correlated with the mixing events on YDs 176, 180, and 184 (Fig. 2.10d). In general, increases to OML

freshwater storage exceeded the total freshwater inputs from the sea ice (Fig. 2.10d, gray line). This resulted in a 0.36 m imbalance in the freshwater budget at the end of Stage II (Fig. 2.10a). Fig. 2.8c suggests that this imbalance at the end of the stage was enhanced by the brief passage of a fresh mixed layer front around YD 191. The imbalances observed earlier in the stage were likely the result of a combination of lateral advections and the challenge of single point IMB observations in capturing the areal mean meltwater flux from a heterogeneous ponded sea ice surface.

c.   Stage III: Development of the Summer Mixed Layer and NSTM

During Stage III, melt pond coverage decreased to less than 40% and A_{OWF} increased from 5% to 26% (Fig. 2.6b). The 21% increase in A_{OWF} occurred in just 9 days (YD 191 to 200) and was coincident with a significant increase in positive wind stress curl around YD 193 (Fig. 2.12a). Divergence of the sea ice resulted in a stage-to-stage average increase of 14 Wm^{-2} in ocean absorbed solar radiation (Fig 2.6d) and highlights the importance of winds to the heat balance in late summer.

The IOBL and OML transitioned to summer conditions with the formation of the sML. In the IOBL, moderate wind forcing deepened the turbulent mixing layer just after the start of Stage III (Fig. 2.7c). Overall during this stage, momentum fluxes increased (Fig. 2.7b) and the ratio of V_{ice}/u_* decreased (Fig. 2.7d) to Stage I values showing well mixed conditions down past the 4.5 m sensor depth. In the OML, a secondary N^2_{max} appeared in the upper 15 m around YD 192 (Fig. 2.8d), consistent with freshwater from the surface mixing down, and marked the development of the sML and associated summer halocline. Initially, the summer halocline was weak and its depth was variable, alternating between 4.5 and 15 m. By YD 196, it became more defined and steadied at a depth of about 10 m. The sML deepened by ~1 m/day, to 20 m by the end of Stage III, which was reasonably consistent with the maximum turbulent penetration estimates (Fig. 2.7c). As expected, the NSTM, which was present just prior to sML development, remained just below the new sML in the summer halocline (Fig. 2.8c).

Latent heat losses dominated the local heat budget following the onset of summer conditions. As expected, the increase in turbulent mixing and open water areas during

this period resulted in larger stage-averaged basal melt rates (1.1 cm day^{-1}). Not expected however, was the decrease in wML heat storage. The NSTM layer, located in the summer halocline stratification at the top of the wML, was assumed to be dynamically isolated from the ice. NSTM heat storage was expected to be retained and slowly increase as small amounts of penetrating solar radiation warm the layer, yet wML observations showed heat storage losses. These heat storage losses were small (~8 MJ m^{-2}, Fig. 2.9a) and may have been the result of weak lateral advections; however, Fig. 2.9c shows modest heat losses (gray line) associated with the YD 196 and 203 mixing events. This suggests a portion of the wML heat loss may have been due to a deepening sML. Negative turbulent heat fluxes were observed at the 6.5 m sensor (Fig. 2.9d, green line) during weak winds and negative dT/dz. The cause of these negative heat fluxes are not explicitly known, but were likely the result of small scale reversals in the local temperature gradient as the sensor passed through the developing summer halocline. Overall, the 1-D heat budget essentially balanced during Stage III with solar radiative input exceeding the combined sink terms by only 4%.

Immediately after the summer halocline developed, between YDs 192 and 194, freshwater storage in both the wML and sML increased, 6 and 20 cm, respectively (Figs. 2.10a and 2.10b). This suggests that roughly ~0.25 m of meltwater was mixed down from the near-surface layer above 4.5 m to facilitate summer halocline formation. This is further evident by the high turbulent freshwater fluxes observed when wind-driven forcing generated sufficiently strong turbulence (Fig. 2.10d) to mix the near-surface fresh layer down past the AOFB sensor. In fact, the highest kinematic salt flux of the time series occurred around YD 196 of 3.8 x 10^{-5} psu-ms^{-1}, the equivalent of 0.12 m^3/m^2 day^{-1}, and was coincident with the observed strengthening of the summer halocline on that same date.

d.   *Stage IV: Marginal Ice Zone Ice-Ocean Boundary Layer*

By the start of Stage IV, A_{OWF} had increased to 0.3 and rapidly expanded to almost 0.5 by the end of time series (Fig. 2.6b) when the instruments were essentially in open water. Stage-averaged incoming solar irradiance was ~100 Wm^{-2} less than that of

the summer solstice maximum (Figure 2.6a), but stage-averaged radiative heat fluxes into the ocean increased five-fold to 63 Wm^{-2} as a direct result of larger open water areas. A little less than 50% (121 MJm^{-2}) of the total ocean radiative input for the melt season occurred during Stage IV. Basal melt rates were irregular with a single 4-day event (YDs 211–215) responsible for 32% (17 cm) of the stage melt (Fig. 2.8a). Outside of this event, melt rates were steady averaging 1.9 $cm\text{-}day^{-1}$ and resulted in 52 cm of total melt during the final stage.

Several warm pulses were observed in the sML during the first 7 days of the stage (Fig. 2.8b). Wind forcing was sporadic (Fig. 2.7a), with predominately weak winds interrupted by moderate events. As expected, large heat fluxes resulted from these conditions, often exceeding 100 Wm^{-2} (Fig. 2.9d). After YD 215, u_* observations (Fig. 2.7b) indicate the sML was strongly mixed; however, the strength of the summer halocline stratification constrained the sML to a relatively thin layer (15-20 m). During weak winds, however, 5.5 m Ri values (Fig. 2.7d) exceeded the critical value (0.25) on several occasions during the stage. This suggests that strong basal melt during Stage IV facilitated the development of near-surface fresh layers and ephemeral pycnoclines, but these were quickly mixed out when interface stresses increased. After YD 220, these near-surface fresh layers seemed to prevail and supported "slippery layers" as seen in the large increase in ice speed relative to wind speed (Fig. 2.7a) and increase to V_{ice}/u_* ratios (Fig. 2.7d). This is further validated by the near-surface warming (Fig. 2.8b) and 14 MJm^{-2} increase in sML heat storage observed between YDs 221 and 227 (Fig. 2.9b). These near-surface fresh layers are less evident in the IMB temperature data (Fig. 2.8a) due to the higher ice speeds (Fig. 2.7a) which mix the limited basal meltwater through the 1–4.5 m volume. In general, turbulent fluxes were highly variable in this strongly stratified MIZ environment with large friction velocity variations ($\sigma^2_{IV} = 2.5\sigma^2_{I\text{-}III}$) and occasional large turbulent heat fluxes (maximum $F_H = \sim 200 \; Wm^{-2}$).

The 1-D heat budget remained reasonably balanced throughout most of the final stage, with the exception of the large melting event between YDs 211–215. Fig. 2.9d highlights this imbalance in the local heat budget, during which observed sink fluxes (gray line) exceeded radiative source fluxes by nearly 70 Wm^{-2} on average over the 4

days (peak imbalance = 148 Wm^{-2}). This imbalance integrated to 24 MJm^{-2} over the period and was accompanied by large turbulent heat fluxes. Moderate turbulent heat fluxes (50-100 Wm^{-2}) were observed at the end of the stage as well, but appeared to be due to higher u_* and OML heat storage values.

Overall, freshwater storage decreased during the final stage (Fig. 2.10a) as a result of increased wML salinity and wML thinning. Investigation of Figs. 2.8b-d indicates that these changes were likely the result of winter pycnocline weakening allowing salt and heat to diffuse into the wML above. Unlike previous stages, turbulent freshwater fluxes were less intermittent as result of the increased mixing in Stage IV and compared reasonably well to total freshwater fluxes from the sea ice (Fig. 2.10d).

2. Enhanced Basal Ice Melt Event

A significant basal ice melt event occurred between YDs 211–215 associated with large turbulent heat fluxes (Fig. 2.9d). This suggests that two different IOBL-OML regimes existed during the MIZ Stage, one supporting the predominate mean melt rate (~1.9 $cm\text{-}day^{-1}$) and another supporting the enhanced melt rate (~4.3 $cm\text{-}day^{-1}$). To investigate, we considered two case studies within Stage IV under different conditions. The goal was to characterize conditions upstream of MIZ C2 to determine factors that led to the short-term imbalances in the local heat budget. This was done by overlaying GPS tracks of C2 over Radarsat-2 imagery (Figs. 2.13d and 2.14d). Since Radarsat-2 imagery was only available every 5 days or so, several days of track information were plotted on a single image (red track). This limitation required that we assumed the ice field around C2 is "frozen," i.e., the general fraction and direction of open water around the C2 ice floe did not change during the case study. Additionally, we ignored upper ocean currents since the distances between C2 and the adjacent leads were small (<5 km) and ice speeds were large compared to ocean currents. To orient the reader on the direction of C2 ice floe motion, vector triangles with direction arrows are placed over the C2 position when the image was acquired and are color coded to the appropriate GPS track sections. These same color codes were overlaid on adjacent supporting plots to associate *in-situ* observations to the specific track periods.

CASE I examines the period between YDs 206 and 216 to study the temporary condition that supported high basal melt rates (Fig. 2.13). Beginning on YD 206 (Fig. 2.13d, black triangle marker), C2 moves southwestward along a classic inertially oscillating track leading up to the YD 211–215 event. Substantial peaks in the 4.5 m δT were observed on YDs 209, 213, and 215 (Fig. 2.13a). These peaks correlate well to periods when C2 was moving in the direction of large open water areas around the C2 ice floe (Fig. 2.13d). These observations suggest that during periods of slow ice motion, differential heating of the ice-covered and open-water upper ocean generated small horizontal scale temperature gradients in the sML budget control volume. Large turbulent heat fluxes (>150 Wm^{-2}, Fig. 2.13b) occurred when the sea ice moved over these warm open water areas resulting in significant latent heat fluxes (Fig. 2.13c). This suggests that basal melt was spatially variable during these thermally heterogeneous conditions, and was strongly dependent on the time history of ice floe displacements relative to open water areas directly around the ice floe. The substantial heat imbalance observed between YDs 211 and 215 (Fig. 2.9d, gray line) indicates that the areal scale (45 km square) of the satellite products used to estimate $F_{rad-ocn}$ were too large during these condition. For example, to estimate the appropriate incoming ocean radiative flux for the YD 211–215 event, the A_{OWF} would have to be almost tripled from 30% to 80% in Eqn. (2.3). This is the approximate A_{OWF} of the 10 km square area just north of the ice floe seen in Fig. 2.13d.

CASE II (Fig. 2.14) investigates the period between YDs 218 and 225 to study the predominate condition that supported the mean melt rate. Observations indicate that changes occurred in both the wind forcing and ice-ocean system over this period. Ice speeds increased around YD 218 (~20 cms^{-1}), and ice direction became persistently westward. A black box is drawn around the 10-day track of the previous case (Fig. 2.14d, upper right) to highlight the large change in ice motion character and spatial scale between the two events. Although C2 moved toward a large area of open water between YDs 219 and 221 (Fig. 2.14d, blue cone), 4.5 m δT observations were virtually unchanged (Fig. 2.14a) indicating upstream conditions were homogeneous. Momentum fluxes were large during this period, yet basal melt rates and turbulent heat fluxes (Figs.

28

2.14b-c) remained low compared to the previous heterogeneous case study, and had little dependence on upstream surface conditions. These findings suggest that during persistent, moderately-strong ice motions, the sML thermal structure is horizontally homogeneous to the first order due to the redistribution of lateral temperature gradients in response to increased mixing and stirring.

3.   Summer Season Overview

In the previous section, we estimated local budgets during each stage of the summer evolution; however, it is important to integrate these budget terms over the entire summer to determine the influence each had on the overall IOBL-ML system. At MIZ C2, a total of 261 MJm^{-2} of heat was estimated to have entered the ocean, with 64% entering through leads ($F_{rad\text{-}owf}$) and 36% penetrating through the ice ($F_{rad\text{-}underice}$). About 65% of the through-ice component was estimated to have come through surface melt ponds, primarily during Stage II. The local heat budget (Fig. 2.9) shows that heat input was partitioned unevenly in the IOBL-OML system, with 77% distributed to latent heat losses (247 $\pm$6 MJm^{-2}) and 23% toward OML heat storage gains (75 MJm^{-2}), similar to the findings of Toole et al. (2010). Sea ice top and bottom interface losses were roughly equal, with 80 $\pm$2 cm (30 cm (snow)/50 cm (ice)) of surface ablation and 91 $\pm$2 cm of basal ice melt.

Given the long duration (81 days) and large spatial distances covered (~500 km), the heat balance closed relatively well, with sink terms exceeding the estimated radiative source term by 19%. Almost half of this imbalance (24 MJm^{-2}) came from the YD 211–215 melting event. This suggests that at least 89% of the total OML heating came from local solar radiative fluxes. The remaining 11% was likely a combination of through-ice radiative parameterization errors and advection of heat from outside the OML control volume. These results are slightly higher than the 0.8/0.2 partitioning found by Steele et al. (2010) in the Pacific Sector of the Western Arctic. These differences are likely due to the geographic location of the current study away from the strong ocean currents near the Bering Strait and north coast of Alaska that influence the Pacific Sector. In summary,

these results indicate the changes observed in the late summer CB SIZ are primarily driven by local thermodynamic process.

4. Regional Variability of the Summer Evolution

To determine the regional variability of the summer evolution across the Canada Basin, the findings from C2 are compared to the ITP-V 70, C3, and C4 locations (see Fig. 2.1a). Upper ocean N^2, freshwater storage, and heat storage were evaluated for each site and are presented on Fig. 2.15. These results were analyzed using methods defined in Section II.C.3 with the exception that the upper limit of integration for the budget control volume was adjusted to the shallowest ITP-V observation (6 m).

The date of sML development showed remarkable consistency across the Canada Basin. The vertical dashed line in Figs. 2.15a-d shows that the summer halocline appeared at all sites around YD 192 (±1 day) and with roughly the same pace of initial deepening. The average depth of the summer halocline, evaluated for each station between YDs 192 and 218, showed increasing depths toward the east (C2 = 17.6 m, C3 = 19.3 m, and C4 = 19.9 m). These differences in sML depth appear to be the result of stronger mixing and weaker stratification at C3 and C4. Estimates of ice-water drag, using Eqn. (2.14) during near-neutral conditions (March to May), indicate that $C_{d(ice-ocn(6.5m))}$ at C3 and C4 (4.6 and 5.9 x 10–^{3}) were significantly larger than $C_{d(ice-ocn(6.5m))}$ values at C2 (3.0 x 10–^{3}). Additionally, mean OML N^2 after YD 192 was lower at C3 and C4 (1.8 and 2.4 x 10–^{4} s^{-2}) as compared to C2 (3.2 x 10–^{4} s^{-2}). This is consistent with the longitudinal orientation of the clusters in early season, with C4 furthest north (~75°N) and C2 furthest south (~73°N). This likely placed C4 in a region of more deformed MYI and C2 in a younger thinner mixture of MYI and FYI. This hypothesis is further supported by the temporary disappearance of the NSTM at C3 and C4 (Figs. 2.15h and 2.15i) during the YD 203 mixing event.

Fig. 2.15e shows similar increases in OML freshwater storage at C2-C4 during the Stage II period of the IOBL-OML evolution. However, the rate of freshwater storage increase at C3 and C4 was slower and may have been the result of the variability in sea ice type/condition mentioned previously. Differences in sea ice age can affect melt pond

30

coverage (Perovich et al. 2002; Perovich and Polashenski 2012) and possibly affect the rate at which drainage occurred locally (Polashenski et al. 2012). ITP-V 70 showed very little correlation to the other sites. The large salinity increases observed at this site around YD 166 (not shown) suggests these differences were possibly due to a lateral front as this site approached the Northwind Ridge. These results suggest that melt ponds drained to the upper ocean on comparable time scales across the Canada Basin SIZ.

OML heat storage comparisons showed even stronger similarities. Fig. 2.15j shows that the large heat storage gains observed at C2 during Stage II of the summer evolution (black box) were also observed at C3 and C4 with nearly identical timing and magnitude. These increases of heat storage were even observed at ITP-V 70, some 250–500 km (depending on YD) northwest of C2. As was the case for C2, heat storage increases at C3 and C4 during Stage II accounted for ~50% of the total time series heat storage gain. Likewise, the NSTM developed at C2, C3, and C4 around YD 190 and immediately prior to sML development. Flattening of the OML heat storage curve after YD 192 at C2-C4 indicates that the shift in heat partitioning away from heat storage and toward latent heat losses was part of a regional, not local, IOBL-OML system change. Heat storage gains between YDs 192 and 218 at C3 and C4 were comparable to C2 and consistent with the estimated radiative input expected below the summer halocline depth (<1 MJ-day^{-1}, following Frey et al. (2011)). These results show that redistribution of solar radiative input within the IOBL-OML system evolved in similar ways across the Canada Basin SIZ throughout the 2014 summer season.

Stage-averaged profiles of N^2, freshwater storage, and δT for C2, C3, and C4 are presented in Fig. 2.16 for a more comprehensive look at the temporal changes in stratification and OML heat content. These results show that changes in the upper ocean profiles are essentially equal through the first three stages of the evolution at each site. This demonstrates that each of the first three stages were distinctive and occur on similar time scales and magnitudes, regardless of their geographic location in the Canada Basin SIZ.

Stage IV also showed unique profiles at all sites with a prominent summer halocline and NSTM; however, some differences do exist. For instance at C2, the NSTM

is slightly warmer and the sML is fresher than at the other two sites. Additionally, C2 was saltier and warmer in the layer beneath the sML and above the winter pycnocline. This was likely due to weakening of the winter pycnocline stratification (Fig. 2.16a), permitting salt (Fig. 2.16d), and heat (Fig. 2.16g) to diffuse upward. During strong mixing between YDs 229 and 231, the sML deepened into this warm layer (Fig. 2.15g) resulting in 4.5 m turbulent heat fluxes of ~100 Wm^{-2} (Fig. 2.9d). These results suggest that upper ocean properties during late summer have some dependency upon their location in the SIZ. This dependency is likely a result of the large variability in open water fraction across the MIZ, which in turn drives changes in basal melt rates and the degree of air-ocean interaction.

E.   DISCUSSION

1.   Causes and Consequences of the IOBL-OML Evolution

The IOBL and OML evolved through four distinct regimes during the summer melt season. In this section, we explore the geophysical forcing responsible for stage development and the influences these forcings have on the larger coupled ice-ocean system.

a.   *Early Season Influences: Melt Ponds*

Melt ponds strongly affected the underlying ocean during early summer. Melt pond development at the beginning of Stage II increased through-ice radiative fluxes, allowing more sunlight to penetrate through the ice cover. This increase in thermal forcing doubled basal melt rates as compared to Stage I. By itself, however, this increased solar heat input did not substantially change the character of the IOBL because interface stresses were still able to mix the near-surface stratification generated by basal melting throughout the larger wML volume (refer to process schematic Fig. 2.17).

As melt ponds began to drain after YD 178, freshwater storage in the ocean mixed layer exceeded the amount provided by basal melting. This enhanced freshwater input from melt pond drainage immediately affected the dynamics of the IOBL. Mixing at and below the 4.5 m observation depth was greatly reduced (Fig. 2.7b), suggesting that the

32

IOBL shoaled to depths above the observation level. The shoaling of the IOBL brought the residual portion of the wML closer to ice-ocean interface, which then warmed due to the stronger radiative fluxes near the surface.

The upper ocean gained a significant amount of heat in the 19 days leading up to NSTM development. In the wML, 39 MJm^{-2} of heat accumulated during this period (Stage II), accounting for 52% of the total OML heat storage observed for the summer. These results are consistent with summer observations from previous Canada Basin studies of melt pond evolutions (Perovich et al. 2002; Perovich et al. 2007b; Perovich and Polashenski 2012) and upper ocean heat content (Jackson et al. 2010; Toole et al. 2010; Jackson et al. 2012; Timmermans 2015), which when compared together, shows that melt pond development and drainage are roughly coincident with the large OML heat storage gains observed in mid-to-late June. We believe that the similarities between this study and previous work provides strong evidence that the early summer upper ocean evolution observed in this study occurs each summer and is closely linked to the evolution of melt ponds in the Canada Basin SIZ.

Linkage of the melt pond evolution with the early summer upper ocean evolution raises interesting questions about the variability of solar radiative input to the ocean under different ice types. Perovich and Polashenski (2012) show that seasonal sea ice has substantially larger melt pond coverage areas (as high as 0.7) and much smaller albedos (as low as 0.32) as compared to multi-year ice (0.3-0.4 and 0.5, respectively). Given these large differences between multi-year and seasonal sea ice and the high solar irradiance in early summer, we speculate that early summer OML heat storage will increase as the Canada Basin SIZ sea ice becomes younger.

b.   *Summer Mixed Layer and NSTM Development*

The sML developed on YD 192 during a modest wind event (7 ms^{-1}, Fig. 2.7a). Interestingly, a similar wind event on YD 184 did not create a substantial near-surface N^2 maximum. This difference in response suggests that insufficient freshwater was available to develop the summer halocline between the YD 180 and YD 184 mixing events. Following the YD 184 mixing event, calm winds prevailed until the sML developed on

YD 192. Although few observations exist above 4.5 m, several observations suggest the presence of a thin, fresh actively mixing layer above a near-surface ephemeral pycnocline based on

1. Large increase in 5.5 m Ri and 4.5 m V_{ice}/u_* ratio;

2. Lack of change in wML N^2 despite significant freshwater input from the ice;

3. Basal latent heat flux greatly exceeded the 4.5 m and 6.5 m turbulent heat flux estimates; and

4. Large increases to freshwater storage and $<w'S'>$ after sML development.

The confinement of shear mixing to this shallow fresh layer had important consequences for the development of the NSTM and sML that later occurred in Stage III (refer to Fig. 2.17 process schematic for follow on discussion). Calm winds after the YD 184 mixing event permitted sea ice meltwater to collect under the ice-ocean interface forming a near-surface fresh layer and associated ephemeral pycnocline. The primary source of this meltwater into the ephemeral layer is suspected to be melt pond drainage based on the timing of surface drainage events from webcam and satellite imagery. A particularly large melt pond drainage event is believed to have occurred around YD 189 when warm water began to collect under the sea ice (Fig. 2.8a). When winds increased on YD 192, u_* values increased also as the near-surface active mixing layer deepens past the 4.5 m sensor forming the sML. The large increase in 4.5 m turbulent salt fluxes and sML freshwater storage after YD 192 indicates a substantial amount of freshwater was sequestered above the budget control volume prior to sML development. This freshwater is important for the development and survivability of the sML, since it prevents subsequent wind events from mixing out summer halocline stratification.

To further examine the importance of the fresh ephemeral layer to the development and strengthening of the summer halocline, Fig. 2.18 shows upper ocean temperature, density and 4.5 m turbulent salt fluxes. Salinity data was not observed between the base of the sea ice and 4.5 m; however, temperature data was available all the way up to the ice-ocean interface. Several warm pulses are observed in the AOFB temperature data near the base of the sea ice between YDs 186–196 (Fig. 2.18a) and in

34

the IMB data around YD 189 (Fig. 2.8a). Normally, temperature data alone cannot be used as a proxy for fresher water in the near-freezing ocean; however, the sharp increases in turbulent salt flux at the 4.5 m (Fig. 2.18b) during the subsequent wind events suggests these warm pulses are likely near-interface meltwater. The YD 184 mixing event yielded low turbulent salt fluxes and no isopycnal tightening indicating limited freshwater was available in the near-surface layer during this time. Conversely, a strong turbulent salt flux response was observed during a similar magnitude wind event on YD 192 and resulted in the development of a weak pycnocline (summer halocline) around 15 m. The YD 196 mixing event followed the warmest near-surface temperature observations and generated the largest turbulent salt fluxes of the time series, almost twice the YD 192 measurement. Strengthening of the summer halocline can be seen around 10 m during this time as fresher water near the interface was mixed down. The buoyancy provided by this mixed down meltwater was able to survive strong mixing associated with the >10 ms^{-1} wind event that occurred on YD 203.

For the NSTM, the results from Stage II show there were near equal allocations of radiative input between latent heat losses and wML heat storage gains. For this to occur, stage-averaged radiative input into the ocean would have to be equally partitioned between the IOBL exchanging heat with the ice-ocean interface and the unmixed portion of the wML. Vertical integration of $F_{rad-ocn}$ using an average of the Frey et al. (2011) visible light absorption coefficients ($K = \sim 0.2$) show that this equal partitioning occurs around 3 m below the sea ice. This is the approximate depth of the 4.5 m sensor and consistent with the weak turbulent fluxes observed at this level. These observations suggest that shoaling of the IOBL and the large areal fraction of melt ponds during Stage II were responsible for the emerging NSTM that appeared on YD 190.

c.   Late Summer Influences: Mixing, Wind Stress, and Open Water Fraction

The increase in friction velocity (u_*) observed in Stages III and IV indicate turbulent mixing intensified following sML development. These increases in u_* were not a consequence of stronger winds during the last half of time series. Evaluation of u$_*$ and winds during periods when the 4.5 m turbulence package was within the active surface

mixing layer ($V_{ice}/u_* < 100$) shows post-sML average u_* was 43% more than pre-sML average u_* (0.0045 and 0.0032 ms^{-1}, respectively), although average winds were nearly equal (4.2 and 4.4 ms^{-1}) (Fig. 2.19). These observations show that turbulent drag between the atmosphere through the ice to the ocean in the presence of the thin sML was higher than that of the thicker wML. We were unable to identify the exact cause of this increased mixing with the observations from this study; however, we hypothesize that the post-sML increase in turbulent mixing was likely due to the concentration of interface transported momentum into a smaller boundary layer volume. For the same wind input, more energy was transferred to the ocean with the sML in place.

The development of the sML was accompanied by an expansion of the open water areas around C2, as evident in the evolution of ice condtions in Fig. 2.3. A_{OWF} expanded from 0.05 to 0.26 between the YD 191 and 200 SAR image estimates (Fig. 2.6b) and resulted in a 45% increase in stage-averaged ocean radiative fluxes from Stage II to Stage III (31 to 45 Wm^{-2}, Fig. 2.6d). Even with these increases to solar radiative input, it is unlikely that thermodynamic processes alone generated the observed 21% decrease in ice coverage in just 9 days. During this same 9-day period, divergent conditions were seen in the local wind stress curl field (Fig. 2.12a). We assessed the relative role of lateral melting and wind-forced divergence by calculating the divergent opening of the ice cover following Stanton et al. (2012). In this method, the difference between triangle areas are divided by the total triangle area to estimate open water fraction ($A_{OWF} = [A(t) - A_o(t)]/A(t)$). We apply this method to two separate cluster array configurations: the triangle area made by C2, C3, and ITP-V 70, and the triangle area made by C2, C4, and ITP-V 70. The results of this calculation show that divergence of the cluster configurations increased open water fraction by as much as 0.11 between YDs 191 and 200 (Fig 2.12b). This indicates that approximately 50% of the increase in the observed A_{OWF} was due to wind-forced divergence.

These observations are consistent with the numerous atmospheric low pressure systems that transited the Canada Basin in the Climate Forecast System Reanalysis data during Stage III (not shown). MIZ cluster GPS tracks show the random ice motions generated by these systems (Fig. 2.1a), which were preceded and followed by the more

36

typical westward trajectories expected on the south side of the Beaufort Gyre. These observations are also consistent with the seasonal weakening of anti-cyclonic winds and ice motion during summer in the Western Arctic (Yang 2006).

The combination of increased ocean radiative input and enhanced mixing increased basal melt rates by 300% following sML development (~1.5 cm-day^{-1} without the YD 211–215 event) when compared to pre-sML development (~0.5 cm-day^{-1}). Increased stress in the sML also altered the partitioning of ocean absorbed radiative heat to 0.86/0.14, with 191 MJm^{-2} going toward latent heat losses and only 30 MJm^{-2} toward OML heat storage gains (Fig. 2.9b). These results indicate the IOBL-OML system was very efficient at converting incoming solar radiation to latent heat loss after the sML developed and likely contributed to the overall ice-ocean feedback within the inner Canada Basin pack ice.

2.   Radiative Parameterizations: Use of Large-Scale Imagery

This work shows that solar radiative fluxes into the ocean can be reasonably estimated using large-scale areal averages of open water and melt pond fractions derived from satellite imagery. Use of this radiative parameterization demonstrates the significance of through-ice radiative input to the summer heat balance, which for this study came to 94 MJm^{-2} of heat absorbed in the upper ocean. This suggests that radiative parameterizations that only consider the open-water component underestimate the radiative input by 36% over the summer season. Radiative parameterizations that included open water fraction and sea ice but exclude melt ponds only reduce this error to 23%. Of note, these errors could be higher since heat imbalances observed during high melt pond coverage in Stage II (Fig. 2.9d) suggest through-ice radiative contributions were underestimated by our parameterization. Visible satellite imagery is a valuable tool for determining melt pond coverage and associated radiative input; however, this product is often hampered by cloud contamination, is less available, and has relatively small spatial footprints. Given the importance of melt ponds to the upper ocean heat balance and the limitations inherent to visible satellite imagery, development of accurate melt pond fractions from SAR imagery is essential.

F.   SUMMARY AND CONCLUSIONS

We have examined the summer evolution of the ice-ocean boundary layer and ocean mixed layer (IOBL-OML) system in the Canada Basin seasonal ice zone. The development of melt ponds in early summer (Stage II) marks the start of significant changes to the dynamic and thermodynamic structure of the upper ocean. Dynamically, stronger near-surface stratification limits the vertical extent of the ice-ocean boundary layer. Through evaluation of freshwater budgets, we find that the buoyancy source for this increased stratification is greater than that supplied by basal melting alone. The additional buoyancy required is likely due to the drainage of melt ponds. In this IOBL-OML regime, radiative input, primarily from transmittance of sunlight through melt ponds, is evenly distributed between the shallow active mixing layer and heat storage in the residual winter mixed layer. Increases to winter mixed layer heat storage during this period accounted for over 50% of the total summer heat input and is the primary source of heat to the developing near-surface temperature maximum.

A near-surface fresh layer and associated ephemeral pycnocline develop under the sea ice during periods of calm winds and melt pond drainage. We infer that meltwater accumulates above this ephemeral pycnocline until wind forcing deepens the layer through shear-driven turbulent processes to form the summer mixed layer (Stage III). We find that the amount of freshwater sequestered in this shallow active mixing layer is critical for the development and survivability of the summer mixed layer to prevent subsequent wind events from mixing out summer halocline stratification.

The partitioning of solar radiative heat input within the IOBL-OML system changes following development of the summer mixed layer. Stronger turbulent mixing leads to larger ocean-to-ice heat fluxes and higher basal melt rates. In this study, radiative input was redistributed 0.86/0.14 between latent heat losses and ocean mixed layer heat storage after the summer mixed layer developed. Concurrent with these changes in the IOBL-OML system, wind-forced divergence in the sea ice marked an important transition in radiative input as larger open water areas allowed more radiative fluxes into the ocean. This occurred despite the lower solar irradiance in late summer and decrease in melt pond coverage.

During the marginal ice zone portion of the drift (Stage IV), continued expansion of open water areas further increased ocean radiative forcing. We estimated that solar input to the ocean during this period accounted for almost half of the total summer radiative input. Basal melt rates were high and variability was large. A single 4-day event, during which turbulent heat fluxes attained values as high as 200 Wm^{-2}, accounted for ~20% of the total summer basal melt. Weak circuitous motion of the sea ice, driven by mid-summer atmospheric conditions, allows differential heating of the under-ice and open-water summer mixed layers. These spatially heterogeneous conditions can lead to patches of enhanced melting on the underside of the ice cover, well away from the Canada Basin seasonal ice zone ice edge (100-200 km). During stronger more persistent forcing, typical under an established Beaufort High, the upper ocean is well mixed horizontally and basal melting is expected to be more uniform.

Overall, these results suggest that the early summer upper ocean evolution is closely linked to the evolution of melt ponds on the sea ice surface. In late summer, the influence of melt ponds reduces and the upper ocean evolution is driven primarily by the increase in turbulent mixing in the summer mixed layer and the fraction of open water in the marginal ice zone.

Regional comparisons conducted across the Canada Basin show that the upper ocean evolution described above was similar across much of the Basin. Heat and freshwater storage gains in early summer were nearly identical in timing and magnitude. The subsequent development of the summer mixed layer and NSTM occurred on nearly the same day throughout the seasonal ice zone. In late summer, properties of the upper ocean are more dependent on seasonal ice zone location, with differences attributed to variations in the open water fraction across the extensive Canada Basin marginal ice zone. These results suggest that the dominant processes driving the thermodynamics of the Canada Basin seasonal ice zone are regional in scale prior to marginal ice zone development, with more localized influences afterward.

1-D local mixed layer heat budgets closed reasonably well, with solar radiative input (source) accounting for at least 89% of the latent heat losses (sink #1) and heat storage gains (sink #2) observed at cluster 2 (sink terms partitioned 0.77/0.23,

respectively). These results suggest that the seasonal ice zone system receives enough local solar radiative input into the upper ocean to achieve the observed late summer conditions, without substantial advective contributions from the ice edge. We term this inside-out method of ice melt the "thermodynamically forced marginal ice zone," which stands in contrast to the outside-in development typical of an Eastern Arctic marginal ice zone where thinning sea ice diminishes under a combination of mechanical and thermodynamic edge effects. This could explain the large area of deteriorating sea ice observed in the Canada Basin seasonal ice zone away from the sea ice edge during the 2014 summer season (Fig. 2.1b).

III. FIELD OBSERVATIONS AND 1-D BOUNDARY LAYER MODEL RESULTS OF DEVELOPING EARLY AND LATE SUMMER NEAR-SURFACE TEMPERATURE MAXIMUMS

A. INTRODUCTION

Recent changes in the Arctic ice-ocean system have led to an increase in upper ocean heating. The primary source of this heating is the two-fold rise in ocean absorbed solar radiation (Perovich et al. 2007) that results from rapidly declining summer sea ice extent (Comiso et al. 2008; Steele et al. 2010). Recent studies in the Canada Basin show that this absorbed solar heating is partitioned 0.23/0.78 between ocean heat storage and latent heat loss (basal ice melt), respectively (Toole et al. 2010; Gallaher et al. 2016). Most of the oceanic heat is accumulated in near-surface temperature maximum (NSTM) features. The NSTM is defined as an upper ocean (< 50m) temperature maximum that: 1) is at least 0.2 ^{o}C above freezing (δT); 2) has a salinity <31 psu; and 3) resides above a cooler water layer by at least 0.1 ^{o}C (Jackson et al. 2010). Jackson et al. (2010) attribute NSTM development to the absorption of solar radiation in shallow, stratified layers beneath melting sea ice and open water during summer. Steele et al. (2011) present an additional formation process caused by cooling of the near-surface ocean under open water areas in late summer, which leaves behind a warmer subsurface layer. Although NSTM heat is gained in the summer, the release of this heat often occurs in later seasons. Observations in the Canada Basin show that the NSTM often survives into fall, and that heat from this layer can be mixed into the surface mixed layer to delay or slow freeze up (Timmermans 2015; Jackson et al. 2012; Jackson et al. 2010; Steele et al. 2011; Steele et al. 2008).

Earlier studies of the NSTM during AIDJEX (Maykut and McPhee 1995) and SHEBA (McPhee et al. 1998) found that the layer was present directly below the summer surface mixed layer, at depths between 25 and 35 m. However, the Canada Basin upper ocean is freshening (McPhee et al. 2009) through a combination of sea ice melt, river runoff, and convergence of Ekman boundary layer transports under the Beaufort Gyre (Yamamoto-Kawai et al. 2009; MacDonald et al. 1999; Proshutinsky et al. 2009). This

freshening decreases the thickness of the surface mixed layer as turbulent length scales decrease under the effects of stabilizing buoyancy fluxes (McPhee 1994). In the current century, the base of the summer surface mixed layer has shoaled to an average depth of 16 m (Toole et al. 2010) and the NSTM has freshened by 4 psu and warmed by 1.5° C (Jackson et al. 2011). To anticipate how these changes in upper ocean properties will affect heat storage in the Canada Basin requires an understanding of the processes that form and sustain the NSTM.

In previous studies, the NSTM has been studied primarily from a seasonal evolution and inter-annual variability perspective. However, comprehensive, *in-situ* observations of a developing NSTM have not, to date, been made. In this study, we use data from the ONR MIZ field program and the MIZ-KOPRI Ice Camp along with a one-dimensional (1-D) turbulent boundary layer model to investigate NSTM formation. We have three objectives: 1) determine the relative contributions of solar radiative forcing, buoyancy forcing, and shear-generated turbulent processes to the development of the NSTM; 2) establish criteria for atmosphere-ice-ocean system events that initiate NSTM development; and 3) identify factors that affect NSTM survivability. In the first part of this study, we focus on the processes that form and preserve/erode the late summer NSTM based on observations collected during the MIZ-KOPRI Ice Camp at MIZ cluster 5 (C5) (Fig. 3.1). Then we compare these findings to a modeling study of the early summer NSTM which formed at MIZ cluster 2 (C2).

B. IN-SITU OBSERVATIONS

1. Data Sources

The air-ice-ocean observations at MIZ C5 came from shipboard and on-ice instruments (Fig. 3.1b and Fig. 3.2) made between 9–14 August (YD 221–226). Starting on the air-side, surface winds were measured by a RM Young anemometer on the Scottish Association for Marine Science Automated Weather System 5 (AWS 5) and a Vaisala Multi-Weather System on Autonomous Ocean Flux Buoy 29 (AOFB 29). Fluxes of down-going shortwave radiation were measured by an Apogee SP-110 pyranometer on AWS 5 and a Hukseflux SR03 pyranometer on AOFB 29. AOFB 29 was not deployed

until YD 224; therefore, hourly AWS 5 data were used between YDs 221.8 and 224, and an average of the 1 h AWS 5 data and the linearly interpolated 15 min AOFB 29 anemometer and pyranometer data were used between YD 224 and YD 225.8. AOFB 29 was also equipped with a Thies Clima 3-D sonic anemometer that provided estimates of air-ice wind stress every 3 h. All of the meteorological sensors were mounted approximately 2 m above the sea ice surface.

In the ice, a 16-element, 30-cm spacing temperature string on AOFB 29 measured thermal gradients in the sea ice and the near-surface ocean. Along with these *in-situ* in-ice measurements, surface-ice conditions were observed remotely using declassified visible grayscale satellite images at 1-m resolution. These images were analyzed to characterize open water, sea ice, and melt pond areal coverage in the vicinity of C5.

In the ocean, *in-situ* salinity and temperature profiles where obtained from R/V Araon CTD measurements (SeaBird SBE 911 plus), which were conducted in a lead located off the starboard side of the ship (see Fig. 3.1b). CTD profiles between 1 and 600 m were taken every 2 hours during the study period.

Observations of turbulent processes in the ice-ocean boundary layer (IOBL) were made from the Naval Postgraduate School (NPS) Turbulence Frame, which was deployed through a 24-in hydrohole beneath the NPS Ice Hut located ~200 m from the R/V Araon (Fig. 3.1b). The frame was equipped with two custom-built ocean flux packages with the same specifications as AOFB 33 described in Chapter II (Section II.B.1). The flux packages, fp1 (top) and fp2 (bottom), were mounted on each end of a 6 m vertical frame (Fig. 3.2). The frame instruments sampled at 4-Hz and ran continuously between YDs 221.8 and 225.8 during which the frame was repositioned in the vertical, by an electric winch, to straddle the base of the surface mixed layer. This sampling strategy allowed direct estimation of turbulent parameters (using eddy-correlation and spectral methods) just above and within the surface mixed layer pycnocline. Measurements from the fixed-depth flux package on AOFB 29 were unavailable until YD 226; however, turbulence data from a high wind event on YD 251 were used to make comparisons with Flux Frame observations. The relative vertical positions of the various MIZ-KOPRI Ice Camp sensors at MIZ C5 are presented in Fig. 3.2.

43

2. Defining the Early and Late Summer NSTMs

The CTD profiles from R/V Araon reveal that two NSTMs were present in the surface ocean (<35 m) during the last two days of the MIZ-KOPRI Ice Camp. These features, at ~25 m and ~10 m (Fig. 3.3c), were found at depths with increased halocline stratification (Figs. 3.3a and 3.3b). The 25-m depth feature will be referred to as the early summer NSTM, since its depth corresponds well with the August depths of the NSTMs observed at MIZ clusters 2–4, which developed in early July (Gallaher et al. 2016). The 10 m feature will be referred to as the late summer NSTM, given that it developed during the late summer observation period, around YD 224 (12 August). The early summer NSTM had a strong temperature maximum (δT = ~0.5 ^{o}C) and easily met the Jackson et al. (2010) NSTM criteria; however, the late summer NSTM was weak and did not meet these criteria. Therefore, the δT > 0.2°C criteria was relaxed to δT > 0.17°C for the late summer NSTM. Upper ocean haloclines associated with the early and late summer NSTMs will be likewise referred to as the early and late summer haloclines (Figs. 3.3a-b).

3. NSTM Heat Content and Upper Ocean Freshwater Storage

To investigate NSTM development, we track changes in upper ocean heat content, stratification, and freshwater content that occur in response to radiative, buoyancy, and dynamic forcing. The heat content of the late summer NSTM layer is calculated as

$$Q_{oml} = c_p \rho_{sw} \int_{z_2}^{z_1} \delta T(s,p)dz, \qquad (3.1)$$

where c_p is the specific heat of seawater (3986 Jkg^{-1}K^{-1}), ρ_{sw} is the reference density (1022 kgm^{-3}) of the upper ocean, and δT is the temperature above the local freezing temperature, which was integrated over the control volume between depths z_1 and z_2. For this time series, the control volume for the late summer NSTM layer is defined as the average observed NSTM depth (12 m) plus or minus 5 m (7-17 m).

To track the late summer halocline we use the depth of the maximum, near-surface buoyancy frequency following the first appearance of the NSTM,

$$N^2{}_{max} = -\frac{g}{\rho_o}\frac{d\rho}{dz}{}_{max},$$ (3.2)

where $d\rho/dz$ is the potential density gradient and g is the gravitational acceleration (9.81 ms^{-2}).

Freshwater storage is calculated to determine the amount of buoyancy added to the near-surface ocean and to estimate the total (i.e., from basal, surface, and lateral melting) amount of freshwater input from the sea ice. Choice of the appropriate control volume for this calculation was a challenge since the surface freshwater inputs were in close proximity to the early summer halocline (~25 m). As a result, application of a constant depth control volume was not suitable since surface freshwater was mixed below and/or early summer halocline salt was entrained above the lower boundary during wind events. Therefore, a variable depth control volume was used based on the 1022 kgm^{-3} isopycnal near the base of the surface mixed layer (magenta line on Fig. 3.4b). To calculate surface freshwater input, we used the Proshutinsky et al. (2009) freshwater content equation

$$FWC = \int_{z_2}^{z_1} \frac{[S_{ref} - S(z)]}{S_{ref}} dz,$$ (3.3)

where S_{ref} is reference salinity (27.5 psu), $S(z)$ is the salinity at water depth z, and z_1 and z_2 are the upper (1 m) and lower (1022 kgm^{-3} isopycnal) boundaries of the FWC control volume.

C.   LOCAL TURBULENCE CLOSURE (LTC) MODEL

1.   Similarity Based Closure and Flux Calculations

To fill in observational gaps and to better understand the dynamics responsible for development of the NSTM, we employ the McPhee (1999; 2008) Local Turbulence

Closure (LTC) model. The basic premise behind the LTC modeling approach is that vertical profiles of turbulent mixing length (λ) may be determined using similarity scaling that accounts for rotational and buoyancy effects on the IOBL (McPhee et al. 1987). The eddy viscosity (K_m) and eddy diffusion ($K_{h/s}$) terms in the first-order closure equations are then determined from the product of λ with the local friction scale velocity (u_*). Estimates of turbulent flux are then obtained from the product of these diffusivities with the local gradients of velocity, temperature, and salinity. LTC model kinematic fluxes were calculated through the following relationship

$$< w'x' >= -K_x \nabla_z x, \tag{3.4}$$

where $<w'x'>$ is the vertical component of kinematic flux, x is the appropriate scalar (T, S) or vector (u,v) property of the fluid, and K is the eddy diffusivity (K_h or K_s) or eddy viscosity (K_m). Dynamic heat fluxes were calculated by

$$F_H = c_p \rho_{sw} \langle w'T' \rangle. \tag{3.5}$$

Kinematic salt fluxes ($<w'S'>$) were converted to buoyancy fluxes to identify vertical layers where the turbulent redistribution of fresher water enhanced local buoyancy. Buoyancy fluxes ($<w'b'>$) were calculated by

$$< w'b' >= \frac{g}{\rho_{sw}} \langle w'\rho' \rangle, \tag{3.6}$$

where ρ' is the density perturbation derived from local density changes associated with kinematic salt and heat fluxes in the equation of state.

To estimate the depth of the actively mixing ice-ocean boundary layer (IOBL) and to characterize summer halocline stratification, the bulk Richardson number (Ri_{bulk}) is calculated by (e.g., Large et al. 1994)

$$Ri_{bulk} = \frac{g(\Delta \rho)}{\rho_{sw}[(\Delta u)^2 + (\Delta v)^2]} \Delta z, \tag{3.7}$$

where $\Delta \rho$, Δu, and Δv are the changes in density and horizontal velocity across a water thickness Δz. Δu and Δv were calculated by taking the difference of the LTC upper ocean velocities against the ocean velocity at the first vertical level below the sea ice in the LTC model (0.6 m). When Ri_{bulk} exceeded a critical value (Ri_c) of 0.65 (Price et al. 1986), deepening due to turbulent mixing was assumed to terminate. Thus, the depth of the active mixing layer for this study is considered all depths shallower than $Ri_{bulk} = 0.65$.

2.   Boundary Conditions

The LTC model is forced by momentum, heat, and mass (salt) boundary conditions through an ice-ocean interface submodel. Full descriptions of these boundary conditions are provided in the subsections below along with the methods and observations that were used to drive them.

a.   *Interface Stresses*

Ice-ocean interface stresses (τ_o) were calculated from ice speeds driven by observed 2 m winds and scaled by the appropriate air-ice and ice-ocean drag coefficients. The air-ice drag coefficient was calculated by

$$C_{d(\text{air}-\text{ice}(2m))} = \frac{u^2_{*(2m)}}{U^2_{(2m)}}, \tag{3.8}$$

where $u_{*(2m)}$ is the friction velocity computed from the AOFB 29 sonic anemometer wind stresses and U is the mean wind at 2 m relative to the sea ice. For this study, a 30-day average (YDs 224–253) $Cd_{(air\text{-}ice(2m))}$ of 3.4 x 10^{-3} was used. Under-ice drag within the LTC ocean surface layer is controlled by the roughness length constant (z_o), which is a measure of the length scale of under-ice roughness elements. Roughness length was calculated by (McPhee 2002)

$$z_o = he^{-\kappa/\sqrt{C_{d(h)}}}, \tag{3.9}$$

where κ is the Von Karman's constant (0.4) and h is the distance from the interface. Similar to the air-ice C_d, a 30-day average (YDs 226–255) ice-ocean $C_{d(ice-ocn(4.5m))}$ of 6.3 x 10^{-3} was estimated from the flux package onboard AOFB 29 which resulted in an average z_o value of 0.029 m for the under-ice surface.

b. *Interface Submodel*

The LTC submodel calculates the kinematic heat and salt balances at the ice-ocean interface to estimate the amount of melting or freezing at the ice base and supplies the resulting freshwater/salt to the ocean boundary layer. The submodel kinematic heat balance is calculated by (McPhee 2008)

$$-\dot{q}+ <w'\mathrm{T'}>_o = w_o Q_L, \tag{3.10}$$

where $\dot{q}$ is the kinematic sea ice conductive flux and $<w'T'>_o$ is the interface kinematic ocean-to-ice heat flux. The imbalance of these two terms yields the kinematic latent heat flux ($w_o Q_L$) which determines the basal melt/freeze rate. The w_o term is the interface velocity (melt rate) and Q_L is latent heat term corrected for sea ice salinity (Maykut 1985). The LTC model uses the following relation to calculate sea ice conductive flux,

$$\dot{q} = \frac{-K_{ice}\dfrac{dT}{dz}}{\rho_{sw}c_p}, \tag{3.11}$$

where dT/dz is the vertical thermal gradient in the sea ice and K_{ice} is the thermal conductivity of sea ice using the approximation of Untersteiner (1961) ($\sim$2 $Jm^{-1}K^{-1}s^{-1}$). For this study, in-ice temperature string data from AOFB 29 was linearly interpolated to the 15 min time steps of the LTC model to represent dT/dz in Eqn. (3.11).

The submodel kinematic salt balance is calculated by

$$< w\,'\mathrm{S}' >_{o} + w(S_{ice} - S_{o}) = 0, \tag{3.12}$$

where $<w'S'>_o$ is the oceanic turbulent salt flux, S_{ice} is the sea ice salinity, and S_o is the interface salinity. The sum of the basal melt rate (w_o) and the rate of meltwater drainage through the sea ice (w_p) represent the total interface velocity ($w = w_o + w_p$). For this study, we generalize w_p to represent all freshwater sources other than basal melt (lateral melt and/or drained surface sea ice melt) by,

$$w_p = w_{fwc} - w_o, \tag{3.13}$$

where w_{fwc} is the total upper ocean freshwater storage (*FWC*) calculated from Eqn. (3.3) divided by the CTD cast time interval (*FWC/Δt*), and w_o is the basal melt rate/velocity predicted by the LTC model.

3.   Initial Conditions

Upper ocean initial conditions were specified by 0.25-m-binned salinity and temperature CTD data that were linearly interpolated to the 100 vertical levels in the LTC model domain between 0 and 60 m (0.6 m resolution). Sea ice thickness was set to 2 m based on the average values of the ice surveys conducted around the study site ice floe (Fig. 3.5). Ice type in the vicinity of Ice Camp was a mixture of first-year and multi-year ice, therefore a bulk sea ice salinity of 4 psu was used in the LTC submodel (Vancoppenolle et al. 2006).

The LTC also allows for distributed absorption of incoming solar radiation over the water column (Q^H), which is calculated with the extinction relation

$$Q^H = \frac{f_{sw} F_{rad}}{z_{sw}} e^{\frac{z}{z_{sw}}}, \tag{3.14}$$

49

where f_{sw} is the fraction of solar radiation that penetrates the sea ice, F_{rad} is the incident solar radiative fluxes from the AWS 5 and AOFB 29 pyranometers, z is the depth of the water beneath the ice base, and z_{sw} is the e-folding depth equal to 4 m (McPhee 2008). Providing a good estimate of f_{sw} is critical to the LTC model mixed layer heat balance. Therefore, we follow the methods of Gallaher et al. (2016) to threshold visible satellite imagery pixel values and estimate the through-open-water (Eqn. (2.3)) and through-ice (Eqn. (2.4)) solar radiative fluxes to the ocean. Results of the visible imagery mask (Fig. 3.6) estimate areal coverage of open water at 0.07 and melt pond coverage at 0.23, leaving a 0.7 areal fraction of bare ice cover. The average f_{sw}, or transmittance, of short-wave radiation to the ocean over the 4 day Ice Camp was estimate at 0.12.

D.   RESULTS

1.   Ice Camp Observations

In general, winds were light during the MIZ-KOPRI Ice Camp. Mostly clear skies resulted in downwelled shortwave radiative fluxes approaching 400 Wm^{-2} (Fig. 3.4a). At the start of the time series (YD 221.8), the surface boundary layer was well mixed and extended to a depth of ~20 m (Figs. 3.4b and 3.4c). This surface layer was underlain by the early summer halocline and NSTM, around 23-m depth, with no evidence of a shallower NSTM feature. A moderate, 6 ms^{-1}, wind event occured on YD 223.4 and generated surface mixing that added ~6 cm of freshwater to the ocean volume above the 1022 kgm^{-3} isopycnal (Fig. 3.4d).

Upper ocean properties changed after the YD 223.4 mixing event. Starting on YD 223.7, the upper 20 m warmed. At YD 224.0, the late summer NSTM criteria ($\delta T > 0.17°C$) was met briefly (Fig. 3.4c, red dot). At the same time, surface ocean stratification increased and the occurence of the near-surface N^2 maxima (Fig. 3.4b, yellow dots) indicates that the late summer halocline developed at ~10 m depth. During the final two days of the time series, freshwater storage gradually increased (Fig. 3.4d) and the late summer halocline strengthened. At YD 224.6, a temperature maximum appeared between 10 and 15 m depth (Fig. 3.4c) marking the formation of the late summer NSTM. The late summer NSTM maintained an average depth of ~12 m through the end of the time series

making the NSTM layer the control volume between 7 and 17 m (Fig. 3.4c, black dashed lines). Heat storage calculations within this control volume (Fig. 3.4d) show that the NSTM layer accumulated ~1.1 MJm^{-2} of heat by YD 225, before a heat loss toward the end of study period. Observations from the Ice-Tethered Profiler 80 (ITP-V 80, Krishfield et al., 2008), deployed ~200 m from R/V Araon on YD 226, indicate the late summer NSTM survived for another 10 days under the C5 ice floe (not shown), but was then mixed out by strong winds in late August. Although the late summer NSTM was weak compared to the early summer NSTM, the signal was distinctive and similar to the early summer NSTM. In the following results subsections, we use these high-resolution observations and LTC model output to identify mechanisms that led to NSTM development at the C5 site. The analysis is then extended to a modeling study of the early summer NSTM at MIZ C2, to gain an overall understanding of NSTM formation processes.

2.   LTC Model Representation

To validate the LTC model and model inputs, we test if it can reasonably represent the upper ocean conditions observed during the MIZ-KOPRI Ice Camp. Employing the methods outlined in Section III.C, we ran the LTC model in two freshwater input modes. In mode one (Figs. 3.7a-c), only the model derived basal melt rate (w_o) is included as a freshwater source to the ocean boundary layer ($w_p = 0$). Salinity and δT outputs (Figs. 3.7a-b) indicate freshwater from basal melt alone could not reproduce the late summer NSTM and halocline. Evaluation of the bulk Richardson number (Ri_{bulk}, Fig. 3.7c) shows that turbulent penetration was shallow; however, during the final two days of the simulation, the active mixing layer extended about half way through the NSTM layer, and likely mixed the absorbed solar heat input.

For mode two (Figs. 3.7d-f), freshwater from all sources was included in the boundary conditions ($w_o + w_p$). Salinity and δT outputs for this simulation (Figs. 3.7d-e) yield a realistic depiction of the observed late summer NSTM and halocline. Additionally, the model NSTM (small red dots) and N^2 maximums (small black circles) share similar depths to the observed NSTM (large red dots) and N^2 maximums (large

51

yellow dots). Ri_{bulk} calculations (Fig. 3.7f) show similar conditions to mode one out to the YD 223.4 wind event; however, during the final two days of the simulation, the depth of turbulent penetration was limited to depths above the NSTM layer. These results suggest that the late summer NSTM was developed by local processes and that this temperature maximum was not the result of lateral advections of heat into the study site. They also provide confidence that the processes responsible for development of the observed NSTM were captured in the one-dimensional LTC model physics and that the imposed initial and surface boundary conditions are accurate.

3.   LTC Model Fluxes

To further elucidate boundary layer processes affecting the evolution of the late summer NSTM, we examine fluxes of radiation, momentum, heat, and buoyancy in the LTC. The exponential decay of visible light energy with depth limited the magnitude of radiative fluxes reaching the NSTM layer. Absorbed solar heat fluxes averaged only ~0.6 Wm^{-2}/m in the 7–17 m volume (Fig. 3.8a) resulting in an integrated NSTM layer total flux of ~6 Wm^{-2}. This rate of heating yielded a total radiative heat input of 2.1 MJm^{-2} to the late summer NSTM layer over the 4 day ice camp; however, not all this heat was retained in the NSTM layer during the first two days of the time series (Fig. 3.4d). Model output of eddy viscosity (K_m) (Fig. 3.8b) and Ri_{bulk} (Fig. 3.7f) show that moderate turbulent mixing occurred in the NSTM layer during the YD 222 and 223.4 wind events. These periods of active turbulence transported heat upwards and out of the late summer NSTM layer (Fig. 3.8c).

Large buoyancy fluxes were also observed with the YD 223.4 mixing event (Fig. 3.8d). These fluxes were elevated during this event for two reasons: 1) the mix down of freshwater added by the w_p term in the LTC submodel (based on freshwater storage observations) and 2) the turbulent transport of salt upward from the early summer halocline. These two processes resulted in tightening of the isohalines between 10 and 20 m and likely contributed to the formation of the late summer halocline. This was based on the observations of the near-surface N^2 maximums that appeared in the model and the observations around 15 m depth (Figs. 3.7d and 3.4b).

The late summer NSTM layer began to warm immediately after the YD 223.4 mixing event, in both the observations (Fig. 3.4c-d) and the LTC model (3.7e). To assess the relative significance of radiative and turbulent fluxes on the evolution of the late summer NSTM over the last two days of the time series, we present time-averaged depth profiles of turbulent heat flux convergence (dF_H/dz), turbulent buoyancy flux convergence ($d<w'b'>/dz$), and radiative flux convergence ($dF_{rad-ocn}/dz$) in Figs. 3.9a and 3.9b. The peak in turbulent heat and buoyancy flux convergence occurred at ~6 m and was above the late summer NSTM layer (Fig. 3.9a). Time integration of the turbulent heat fluxes in the 7–17 m layer (Fig. 3.9c, black line) suggests these fluxes did not contribute to NSTM layer heating. However, the convergence of turbulent buoyancy fluxes had a significant influence on increasing stratification near the top of the NSTM layer. This increase in stratification can be seen in the model N^2 values (Fig. 3.9d) which show an intensifying peak around 8m depth. The displacement of this N^2 peak below the buoyancy flux peak is likely associated with the stronger turbulent mixing present at the base of the active mixing layer (Fig. 3.8b). The N^2 peak marks the development of the late summer halocline, which occurs just above the developing late summer NSTM (small red dots). The observed N^2 values (contours for values >3 x 10^{-3} s^{-2}) and NSTM (large red dots) are also plotted on Fig. 3.9d and show similar depths and orientation to the model features. Development of the summer halocline is a key event for the development of NSTM since it prevents significant turbulence from penetrating into the NSTM layer (Figs. 3.7f and 3.8b).

About two thirds of solar radiative flux was absorbed in the top 7 m of the water column (Fig 3.8a); however, heat storage in this layer was small (Fig. 3.4c), because this heat was readily transported to the ice base where it caused melting (Fig. 3.8c). In the NSTM layer, absorbed solar radiation was considerably less, but as previously discussed, buoyancy fluxes near the top of the NSTM layer substantially inhibited turbulence penetration below 7 m depth (Fig. 3.9b). As a result, model (Fig. 3.9c, blue dashed) and observed (blue solid) heat storage increased in the late summer NSTM layer. Integration of absorbed radiative heat fluxes in the NSTM layer (Fig. 3.9c, red dashed) indicates sufficient solar heat was available to support development of the NSTM. After YD 225,

model and observed NSTM heat storage decreased due to a slight increase in mixing (Fig. 3.8b), which entrained heat from the upper portions of the layer (Figs. 3.4c and 3.7e). These results show that the source of heat to the developing late summer NSTM during the last two days of the time series was solar radiative flux absorbed within the NSTM layer. Additionally, increases to buoyancy above (Fig. 3.9b) and within the NSTM layer (Fig. 3.8d) aided the retention of this heat by inhibiting turbulent mixing.

4. Wind and Buoyancy Sensitivity Testing

Results from the previous section show that the NSTM develops from an interplay between wind-driven mixing, buoyancy forcing, and proximity to shortwave radiative heating. In this section, we investigate the influence of these processes on NSTM development by systematically varying LTC inputs for wind and freshwater.

We start by presenting four case study examples. In Case I, winds are increased 25% from observed and freshwater input is kept at the observed level of 0.1 m. The increased wind forcing completely mixes away the late summer NSTM in the model (Fig 3.10a). In Case II, winds are increased 50% and freshwater input is doubled to 0.2 m. Some warming of the NSTM layer occurs (Fig. 3.10b); however, the signal is reduced and it occurs deeper than the observed NSTM. This indicates that the large increase in freshwater established a pycnocline to protect the NSTM from mixing; however, the stronger winds deepened the protective pycnocline further from the radiative source resulting in smaller heat storage. In Case III, winds are reduced 25% and freshwater input is as observed. The NSTM develops near the top of the 7–17 m control volume (Fig. 3.10c) and the peak temperature is higer than the observed NSTM. These results suggest that the turbulent boundary layer shoaled in response to the weaker wind forcing, moving the summer halocline closer to the radiative source. In Case IV, winds remain unchanged and freshwater is reduced 25%. The late summer NSTM develops at nearly the same depth and timing as the control run and the observations, but at a lower temperature (Fig 3.9d). This indicates that the weaker summer halocline was less able to prevent turbulent mixing from entraining heat out of the NSTM layer.

54

The sensitivity study was expanded to 24 different combinations of wind and freshwater input to determine which of these forcings more heavily controlled development of the late summer NSTM. Fig. 3.11 shows the cumulative heat storage gain in the 7–17 m control volume across the time series for each of these 24 cases, which tested scenarios of wind and freshwater content between ±50% of the observed values. Results show that the mean difference in heat storage between the 150% and 50% wind categories equaled +2.03 MJm^{-2}. This indicates that changes in wind forcing greatly affected the amount of heat storage accumulated in the model NSTM layer. The mean differences in heat storage between the 50% and 150% freshwater content categories yielded +1.18 MJm^{-2}, which was 42% less than the LTC model wind response. These results show that, under this range of model conditions, development of the late summer NSTM was primarily controlled by the character of the wind forcing.

### 5.	Evolution of Turbulent Eddies through the NSTM Layer

For the NSTM to survive, sufficient stratification must be established near the top of the NSTM layer to prevent subsequent mixing events from transporting heat out of the layer. This is consistent with the lack of turbulence observed in the NSTM layer from the Turbulence Frame and the high Ri_{bulk} values predicted by the LTC model at the Frame deployment depths (Fig. 3.7f, gray dots). However, low-level turbulence was observed by the Turbulence Frame in the NSTM layer around YD 225.65 (see Figs. 3.7f and 3.8b for time/depth reference, green dots). This event is investigated in the analysis below to understand how turbulent eddies behave in weak summer halocline stratification.

To study the evolution of turbulent eddies within, and near, the late summer halocline and NSTM, we analyze vertical velocity spectra from the Turbulence Frame flux packages. McPhee and Martinson (1994) show that the turbulent energy peak found in the vertical velocity spectrum scaled by the wavenumber ($kS_{ww}(k)$) can be used to find the peak mixing length (λ) in the ocean boundary layer by

$$\lambda_{peak} = \frac{0.85}{k_{max}},$$
(3.15)

where k_{max} is the wave number associated with the turbulent peak. Conversion of the frequency-space spectrum to a wavenumber-space spectrum was accomplished by using the Taylor frozen field hypothesis (Taylor 1938). In $kS_{ww}(k)$ spectrum, the k multiplier changes the -5/3 power law expected of the inertial subrange (Kolmogorov 1941) to -2/3. Using a scaling of the S_{ww} spectrum within the inertial subrange, turbulent kinetic energy (TKE) dissipation (ε) can be found using the inertial-dissipation method (Hinze 1975; McPhee 1994)

$$\varepsilon = [\frac{3}{4\alpha_\varepsilon} S_{ww}(k) k^{\frac{5}{3}}]^{\frac{3}{2}}, \tag{3.16}$$

where α_ε is the Kolmogorov constant (0.51), $S_{ww}(k)$ is the vertical velocity power auto-spectrum, and k is the wavenumber.

The presence of a well-developed inertial subrange in the Turbulence Frame measurements for the 40-minute period around YD 225.65 (Fig. 3.12) confirms the existence of fully developed turbulence at the 9 m (blue) and 15 m (green) sensor depths. For comparison, a turbulent spectrum from a high wind event (~10 ms^{-1}, magenta) at AOFB 29 on YD 251 is plotted and demonstrates how weak turbulence was within the late summer halocline and NSTM layer. The turbulent energy peaks from the Turbulence Frame auto-spectra were 1–2 decades lower than the high wind case. Turbulent mixing in the NSTM layer was able to penetrate despite the presence of the late summer halocline because density gradients were very weak ($d\rho/dz \sim 0.02$ kgm^{-3}m^{-1}) when compared to the early summer halocline ($d\rho/dz \sim 0.2$ kgm^{-3}m^{-1}). For comparison, the 1-hr average Richardson number across the Turbulence Frame around YD 225.65 was ~0.5; however, application of the same shear values to the early summer density gradients yields an average Ri of ~8.

Estimations of the turbulent mixing length (λ) from Eqn. (3.15) show λ decreased from ~25 cm near the top (9 m) of the NSTM layer to ~10 cm near the bottom (15 m) (Fig. 3.12). These values are similar to the model predicted λ_{LTC} of 16 cm for both levels. Estimated TKE dissipation (ε) using Eqn. (3.16) showed ε_{fp1} were 4 times ε_{fp2}, but the

upper flux package dissipation was 1/4 that of the strong wind case ε estimated at the 2.5 m level (magenta). Analysis of turbulent spectra adjacent in time to this event (Fig. 3.12, green dashed line) indicate that for most of the period when the NSTM was present, turbulence levels were below the very low noise floor of the acoustic travel-time velocimeters. These results suggest, that despite the presence of weak turbulence, transport rates were too small to remove significant amounts of heat from the NSTM layer.

6.   Comparing the Early and Late Summer NSTMs

The analysis of the MIZ-KOPRI Ice Camp conditions at MIZ C5 reveal that the late summer NSTM develops under a delicate balance of weak wind-forced ice-ocean interface stresses and modest buoyancy fluxes, but how does this balance differ for the early summer NSTM? To examine this science question we model the formation of the early summer NSTM at MIZ Cluster 2 (C2) and then compare these results to the late summer NSTM case.

a.   *LTC Model Initial and Boundary Conditions at MIZ C2*

To successfully compare the early and late summer NSTM cases, the LTC model must be able to reasonably reproduce the observed conditions at MIZ C2 in early summer. Similar to MIZ C5, the observations made at MIZ C2 were extensive and provided an excellent characterization of the ice-ocean system in order to properly initialize the LTC model and update the boundary conditions. For the initial conditions, we use the upper ocean salinity and temperature observations from AOFB 33 at 4.5 m merged with observations from ITP-V 77 made between 6.5 and 60 m (refer to Section B.2 in Chapter II for ITP-V description). For the boundary conditions, observations of air-ice wind stress were not made at MIZ C2, therefore the LTC model was driven by ice speeds obtained from differencing 5 min GPS positions at AOFB 33. Sea ice temperature gradients were provided by the 16-element temperature string on AOFB 33. The sea ice percolation velocity (w_p) was set to zero except on YD 189 when the equivalent of 0.25 m of freshwater was introduced based on the melt pond drainage estimates made by Gallaher et al. (2016). The LTC model was updated with the MIZ C2 underice drag

coefficient of 3.0 x 10^{-3} ($Cd_{(ice\text{-}ocn(4.5m))}$) based on measurements made by the turbulence package on AOFB 33. For shortwave radiative input (Q^H), we set the fractional solar radiation terms in Eqn. (3.14) ($fsw \cdot Frad$) to the ocean radiative fluxes estimated by Gallaher et al. (2016) at MIZ C2. All other model parameters, constants, and setups remain as outlined in Section III.C. The model simulation period begins after the mixing event on YD 184 and ends on YD 198.

b.   *LTC Model Representation of the Early Summer NSTM at MIZ C2*

The LTC model run for the early season case reasonably reproduces the observed conditions (see Fig. 2.8 b-c for C2 observations). The observed early summer halocline (Fig. 3.13a, yellow dots) matched well with the depth of the modeled near-surface N^2 maximum. Likewise, the depth of the observed NSTM (Fig. 3.14b, red dots), based on Jackson et al. (2010) criteria, was reasonably close to the depth of LTC temperature maximum, with only minor deviations betweenYDs 194 and 196. These model results corroborate the assertions of Gallaher et al. (2016) that melt pond drainage in early July 2014 led to the development of the summer mixed layer, summer halocline, and associated NSTM. To compare the relative influences of ice motion and meltwater input on development of the early summer haolcline and NSTM, we decompose the bulk Richardson number (Eqn. (3.7)) into its shear (ΔV^2) and buoyuancy ($\Delta b = g\Delta\rho/\rho_{sw}$) components. These components were evaluated from the LTC model across the summer mixed layer (Δh) defined from the model surface (0.6 m) to the summer haolcline depth (near-surface N^2 maximum). As expected, the buoyancy component (Fig. 3.13c) increased substantially (0.004 ms^{-2}) on YD 189; however, a corresponding increase in the Ri_{bulk} did not immediately occur (Fig. 3.13e) due to the very shallow surface mixed layer (small Δh) following the simulated melt pond drainage event. After the early period increase, Δb values decreased to just below the model period average of 0.0022 ms^{-2} (blue dashed) and were well above the late summer modeling study mean (red dashed). These increases in upper ocean buoyancy led to a high Ri_{bulk} condition throughout the early summer case with average Ri_{bulk} values nearly three times the late summer case, at 11.5 and 4.3, respectively (Fig. 3.13e). This indicates stratification within the early summer halocline greatly inhibited turbulent mixing despite the slightly higher average

58

ΔV^2 component (Fig. 3.13d). These results suggest the early summer halocline and associated NSTM are dominated by buoyancy forcing in contrast to the wind sensitive late summer case.

c.   LTC Model Comparisons of the Early and Late Summer NSTM under MIZ C5 Conditions

The under-ice drag coeficient for the early summer case at C2 was smaller than at the MIZ C5 site, implying that the sea ice at C2 was smoother. To ensure these differences in ice-ocean drag, ice speed, basal melt rate, and wind forcing did not affect the conclusions made by the early summer model study; we impose the melt pond drainge event on the model settings and forcings of MIZ C5 to compare the early and late summer NSTM under identical interface stresses. As with the MIZ C2 case, the percolation velocity (w_p) was setup to deliver 0.25 m of freshwater to the ocean boundary layer over a 1-day period (YD 223 for this case). Results show that a distinctive near-surface N^2 maximum and temperature maximum appear in the model (Figs. 3.14a-b) following the release of the simulated melt pond water. Inspection of the early (Figs. 3.14a-b) and late (Figs. 3.14d-e) summer cases side-by-side show that the NSTM is ~50% warmer (0.3°C versus 0.2°C) than the early summer case and was supported by a stronger halocline. In Figs. 3.14c and 3.14f, the Ri_{bulk} critical value ($R_c = 0.65$) and the next three multiples of the critical value (i.e., $2Ri_c$, $3Ri_c$, and $4Ri_c$) are plotted to compare the vertical distribution of the halocline stratification. In the early summer case, the vertical gradient is tight indicating a high Ri_{bulk} condition in the upper early summer halocline. Conversely, the late summer contour gradient is relaxed suggesting moderate increases in stress could easily overcome the late summer halocline stratification.   As observed during the C2 case, evaluation of the early summer Δb and Ri_{bulk} values are consistenly greater than the late summer case (Figs. 3.15a and 3.15c). More importantly, the depth of the early and late summer haloclines shoaled at different rates following the YD 223 buoyancy and wind events. The early summer halocline immediately shallowed to 6 m while the late summer halocline slowly ascended to 8 m over the next 1.5 days (Fig. 3.15d). Rapid shoaling of the early summer halocline placed the remnant mixed

layer closer to the higher radiative fluxes near the surface (Fig. 3.15e) and resulted in higher heat storage gains in the early summer case (Fig. 3.15f).

To assess the sensitivity of the early summer case to wind forcing, we increased model winds by 50% resulting in an average wind of ~4 ms^{-1} and peak wind of 9 ms^{-1} (conditions similar to MIZ C2). Model results show that the early summer NSTM is cooler and deeper, but remains a distinctive feature in the upper 20 m of the modeled ocean (Figs. 3.16a-b). This is in contrast to the late summer case which completely mixes out under the increased stresses with no temperature maximum present (Figs. 3.16c-d). These findings suggest that the early summer halocline and NSTM is heavily buoyancy forced (melt pond drainage) and can develop over a board range of ice-ocean interface stresses.

E.   DISCUSSION

1.   NSTM Formation

In this study, we were able to successfully reproduce observed NSTMs in the early stages of development using the LTC 1-D turbulent boundary layer model. Model results show that the increase in heat storage associated with development of the NSTM was largely due to the absorption of solar radiative fluxes just below the summer halocline stratification (Fig. 3.9), consistent with the findings of Jackson et al. (2010) and Steele et al. (2011). Model results also showed that there was no evidence of vertical heat flux convergence through turbulent processes in the NSTM layer; however, the balance of turbulent momentum fluxes with buoyancy fluxes in the surface ocean had a large influence on the depth and strength of the summer halocline. The depth of the summer halocline is the most important factor for determining the amount of solar radiation absorbed in the NSTM layer (Figs. 3.9b-c, 3.15d-f) while the strength of the protective summer halocline controls the amount of heat removed from NSTM by turbulent transport (Figs. 3.11, 3.16). The depth of the NSTM relative to the N^2 maximum was consistently deeper by 2–5 m (Figs. 3.9d, 3.13a-b). This was likely due to the higher levels of turbulence in the upper summer halocline, which were confirmed by eddy viscosity estimates from the LTC model (Fig. 3.8b) and by observations from the

turbulence frame (Fig. 3.12). Even when turbulent eddies intermittently entered the NSTM layer, observations suggest the decrease in turbulent mixing length and intensity of these eddies strongly limited the amount of heat transported out of the NSTM layer (Fig. 3.12). Overall, these findings suggest the NSTM is dependent on the characteristics of the overlying summer halocline, which, in turn, is a function of the surface ocean shear and buoyancy production terms in the turbulent kinetic energy balance.

2. Survivability of the Early and Late Summer NSTM

These comprehensive observations from early and late summer allowed us to investigate the similarities and differences between the two NSTM events. The results of this study show that NSTM formation mechanisms were similar; however, the differences in early and late summer buoyancy forcing affected the intensity and survivability of the NSTM signal.

In early summer, the drainage of melt ponds substantially increased the strength of the summer halocline and increased the survivability of the NSTM. These conditions made formation of the early summer NSTM virtually inevitable since it would have taken a strong storm event to erode the summer halocline stratification (Figs. 3.16a-b) in this high Richardson number environment (Figs. 3.13e). Comparison of the early and late summer NSTMs show that the early summer case heats nearly twice as fast as the late summer case during initial development (Fig. 3.15f). This enhanced heating was a consequence of the rapid shallowing by the surface mixed layer in response to strong buoyancy fluxes, which brings the residual mixed layer closer to the solar source (Figs. 3.15 d-e). Furthermore, the strength of the early summer halocline reduces the number of turbulent events that can penetrate the NSTM layer allowing it to continue to accumulate solar input. The survivability of this accumulated heat storage is well documented (Timmermans 2015; Jackson et al. 2012; Jackson et al. 2010; Steele et al. 2011) and confirmed in the late summer observations of this study (Fig. 3.3). Along with the initial buoyancy increases provided by melt pond drainage, the persistence of the early summer halocline allows basal meltwater to be stored in the thin surface mixed layer and further enhances summer halocline stratification. In addition to these processes, Ekman pumping

in the Canada Basin (Proshutinsky et al. 2009) adds additional freshwater to the summer mixed layer and deepens the NSTM further from ice-ocean interface stresses. These well-timed seasonal events in the ice-ocean system ensure development and preservation of the early summer NSTM, which can then be a source of heat to the fall/winter ice-ocean boundary layer.

In late summer, the limited freshwater inputs from the sea ice greatly reduced the strength of the summer halocline and survivability of the NSTM. Freshwater fluxes were generally constrained to the collection of freshwater in leads due to lateral melt (Paulson and Pegau 2001; Hayes and Morison 2008), and basal melt due to ocean-to-ice heat fluxes. Basal melt rates during the MIZ-KOPRI Ice Camp were small (LTC model melt rate at C5 ~0.7 cm-day^{-1}) due to the large areal coverage of sea ice, low melt pond fraction, light winds, and reduced solar input in late summer. However, 6 cm of freshwater was introduced to the boundary layer prior to NSTM formation and was likely a result of meltwater mixed down from the surrounding leads during the YD 223.4 wind event. The is consistent with SHEBA observations and model studies which show that lead surface fresh layers mix out when winds increase to 6–7 ms^{-1} and wind stresses approach 0.1 Nm^{-2} (Skyllingstad et al. 2005). In addition to freshening from above, observations and model results suggests that salt was entrained upward from the early summer halocline (Fig. 3.8d), which further tightened the near-surface isohalines (Fig. 3.4b). This suggests that the presence of the deeper early summer halocline may have assisted development of the late summer halocline. Nevertheless, the large disparity between early and late summer freshwater inputs made the late summer halocline and NSTM a marginally stable system. These results suggest that the late summer halocline and NSTM are transient features that can only be sustained during periods of weak winds.

F.   CONCLUSIONS

Although the late summer NSTM was admittedly inconsequential from a heat storage perspective, the timely development of this feature within a comprehensive set of ice-ocean sensors provided an excellent laboratory for studying NSTMs in general. This

study shows that a weak late summer NSTM can develop over a deeper, established, early-summer NSTM during weak wind conditions. As found in previous studies, our results show that the primary source of heating to the NSTM layer is penetrating solar radiation. However, the major findings of this study focus on the less studied background conditions that facilitate NSTM formation and the turbulent boundary layer processes that sustain or erode the NSTM.

Results from this study show that summer season buoyancy and wind events within the Canada Basin air-ice-ocean system facilitate the development of shallow haloclines and NSTMs. In early summer, rapid melt pond drainage supplies the buoyancy required to support the immediate development of the early summer halocline. The substantial buoyancy forcing provided by this meltwater generates a high Richardson number environment in the summer halocline that is able to endure elevated levels of ice-ocean interface stresses. Numerical model results show that the early summer NSTM continues to survive despite wind increases of 50% above the observed conditions. Furthermore, the strength of the early summer halocline prevents substantial turbulent fluxes from transporting heat out of the NSTM layer and ensures its survivability into late summer and fall.

In late summer, freshwater fluxes from the sea ice decrease considerably; however, during periods of weak winds, shallower haloclines may form above the early summer halocline. However, the weaker freshwater inputs in late summer permit only gradual shoaling of the surface mixed layer resulting in a 50% reduction in NSTM warming during initial development. The late summer halocline was less protective and permitted turbulent eddies to penetrate the NSTM layer, even during weak wind forcing. However, turbulence measurements from inside the late summer halocline and NSTM suggest that these turbulent eddies decrease in size and intensity and are not energetic enough to transport significant amounts of heat out of the NSTM layer. Wind and buoyancy sensitivity studies showed that the late summer NSTM was easily mixed out by wind increases above observed conditions even when buoyancy forcing was increased by 50%. These results show that the reduced availability of freshwater makes the late

summer balance between interfaces stresses and buoyancy tenuous, and the survival of the NSTM primarily dependent on local wind conditions.

Overall, the magnitude and fate of the NSTM depends on the strength and depth of the protective overlying summer halocline and wind forcing. In the Canada Basin, observations (Gallaher et al. 2016) and the numerical simulations of this study suggest the buoyancy event that leads to the persistent multi-seasonal summer halocline and associated NSTM is likely the drainage of melt ponds in early summer.

IV. MAJOR FINDINGS AND FUTURE WORK

A. NEW CONTRIBUTIONS

Here we have examined the Canada Basin ice-ocean boundary layer and ocean mixed layer during summer using field observations from the Office of Naval Research MIZ field program. The data sets generated by the MIZ experiment autonomous sensor arrays, remote sensing assets, and manned Ice Camp instruments were extraordinary and opened a window to the dominant air-ice-ocean processes driving the development of open water areas in the Canada Basin seasonal ice zone. The subsections below outline the new contributions to the field of Arctic ice-ocean science discovered during this study.

1. The Influence of Melt Ponds on the Early Summer Evolution

The expansion and drainage of melt ponds on the sea ice surface had a considerable influence on the upper ocean in early summer. The shortwave radiative parameterization used in this study estimates that ocean radiative fluxes more than doubled following the expansion of melt ponds. One week later, melt pond drainage added substantial buoyancy to the near-surface ocean shoaling the turbulent boundary layer and placing the underlying residual mixed layer closer to the solar radiative source. Warming in this residual mixed layer led to significant heat storage gains and accounted for over 50% of the summer total heat storage increase and development of the early summer NSTM. Deepening of the active mixing layer during the subsequent wind event led to the development of the summer mixed layer and early summer halocline, which persisted throughout the summer. These results suggest the upper ocean evolution is strongly linked to the evolution of melt ponds on the sea ice surface. These findings were consistent across the Canada Basin and explain the sharp increase in early summer heat and freshwater storage observed in previous studies.

2. Enhanced Melting in the Marginal Ice Zone

Basal melt rates increased three-fold following the formation of the summer mixed layer. These enhanced basal melt rates were attributed to the expansion of open water areas in the seasonal ice zone and the ~40% increase in surface mixed layer turbulent stresses following summer mixed layer development. Wind stress curl observations from MIZ *in-situ* instruments show that wind-force sea ice divergence was a catalyst for the initial expansion of open water areas in the Canada Basin. As a result of these larger open water areas, radiative fluxes to the ocean surface were estimated to have increased by nearly 50% in just 9 days. These results suggest that the late summer ice-ocean boundary layer is very efficient at converting absorbed solar radiation into latent heat losses at the ice base. This ice-ocean interaction was responsible for over three-quarters of the study period ice melt and was likely an important contributor to the ice-ocean albedo feedback mechanism in the Canada Basin.

Basal ice melt was found to be exceptionally episodic in the marginal ice zone when light winds prevailed. Ocean-to-ice heat fluxes ranged from 0 to 200 Wm^{-2} and basal ice melt rates were from 0 to 6 cm-day^{-1}. Observations of upper ocean temperature show that the thermal structure of the upper ocean was spatially heterogeneous due to the differential heating of the ice-covered and ice-free areas of the marginal ice zone. Extreme basal melting events occurred when winds moved the instrument ice floe over adjacent open water areas. These results show that significant melting can occur in the marginal ice zone well away (100-200 km) from the sea ice edge.

3. The Thermodynamic Marginal Ice Zone

The Canada Basin marginal ice zone developed over a large area covering over 50,000 km^2 (Fig. 2.1b). Results from the 1-D local heat budget of the upper ocean show that almost 90% of the observed basal sea ice melt and heat storage came from solar radiation absorbed locally. These findings suggest that the late summer Canada Basin seasonal ice zone is largely a "thermodynamic marginal ice zone" where the sea ice essentially melts in place due to local thermodynamic forcing. This process differs significantly from the open

ocean Eastern Arctic and Bering Sea marginal ice zones which develop under strong edge forcing (mechanical and thermodynamic) over narrow regions.

4.   Early and Late Summer NSTM Development

The initial stages of NSTM formation were observed and modeled as part of this study. Model results show that the increase in heat storage associated with NSTM formation was largely due to the absorption of solar radiative fluxes below a protective summer halocline with no significant contributions from turbulent vertical heat flux convergence. Although the NSTM is a thermodynamic feature, its formation and survival were found to be dependent on the dynamic balance between surface buoyancy forcing and shear stresses, which determine the strength and depth of the summer halocline.

Observations from the MIZ-KOPRI Ice Camp at MIZ C5 confirm that two NSTMs can exist simultaneously with a shallow late summer NSTM overlaying a deeper early summer NSTM. The formation of these NSTM features was found to be connected to summer season buoyancy and wind events. For the early summer NSTM, numerical simulations from this study suggest the buoyancy event that leads to the persistent multi-seasonal summer halocline and associated NSTM is the drainage of melt ponds in early summer. In late summer, limited freshwater inputs from the sea ice greatly reduce the strength of the summer halocline causing the NSTM to be an ephemeral feature that can only be preserved during periods of weak winds.

B.   FUTURE WORK

Several areas of the 2014 ONR MIZ data set are still unexplored and many science questions still remain. In the subsections below, recommended areas of continued research are provided in order of priority.

1.   Defining the Thermodynamic Marginal Ice Zone

Unlike the Eastern Arctic MIZ, the Western Arctic MIZ is less defined and covers an extensive area. In this study, we defined the MIZ as the buffer zone between compact ice (sea ice concentration >70%) and open water (Wadhams 2000); however, this classification was based upon observations of previously studied edge forced MIZs with

narrow transition zones. Results of this study show the Western Arctic MIZ develops well away from the ice edge over wide transition zones. A set of repeatable criteria are required to properly identify and characterize this transition region in the Western Arctic.

2. Increased Turbulent Mixing in the Summer Mixed Layer

Turbulence measurements near the ice-ocean interface showed momentum fluxes increased following summer mixed layer development, despite a slight decrease in mean wind speed in late summer. The precise reason for this increase was not evident in this study; however, we speculated that momentum fluxes were concentrated in the thin summer mixed layer. Another possible explanation could be the increase in air-ice and ice-ocean drag in late summer as ice floe edges becoming more prominent making the sea ice surfaces rougher. More research is needed to determine if this observation was unique to our study site, and if not, determine the specific mechanism(s) responsible for the enhancement of turbulent stresses in the summer mixed layer.

3. Use of Large Scale Imagery during Weak Wind Conditions

Results from the 1-D local heat budget show the use of large scale SAR and visible satellite imagery to estimate areal averages of ocean absorbed solar radiative fluxes was generally effective. However, a sizable imbalance occurred in the local heat budget as the instrument array drifted through the MIZ during weak wind forcing. These conditions generated very local heterogeneities in the upper ocean thermal structure resulting in an underestimation of open water fraction by large scale SAR imagery. Further research is needed to develop a relationship between ice velocity and imagery scale to capture the appropriate open water fraction during weak wind conditions in the MIZ.

4. Impact of an Expanded Canada Basin Seasonal Ice Zone

The Canada Basin SIZ continues to expand. During the 2014 season, development of the MIZ was determined to be driven primarily by local solar radiative forcing; however, future expansion of the SIZ will provide more fetch for the development of wind and swell surface gravity waves in late summer. Modeling studies are needed to

determine the impact this enhanced mechanical edge forcing will have on the thermodynamically conditioned/weakened sea ice in the Canada Basin SIZ.

5.   Improvements to Ice-Ocean Coupled Modeling

One of the primary goals of the 2014 MIZ Program was to gain a predictive capability of future sea ice conditions in the summertime Arctic Ocean. Coupled air-ice-ocean models are the primary tool for providing this predictive capability; however, computational capacity is limited and ice-ocean observations are scarce. Given these constraints, choices on which component of the coupled air-ice-ocean model to improve depends on its relative influence on the Arctic System. Based on the findings of this study, the sea ice component had the largest influence on initiating the summer thermodynamic evolution of the upper ocean.   To be more specific, the expansion and drainage of melt ponds exhibited the greatest control and generated the following summer evolution events:

1.   Modulated shortwave radiative input to the ocean

2.   Shoaled the ocean boundary layer increasing ocean heat storage

3.   Developed the summer mixed layer increasing basal melt rates

4.   Developed the NSTM to carry summer heat to subsequent seasons

These findings suggest that improvements to sea ice morphology and permeability in the model, along with sea ice thickness, will generate the largest gains in model performance during the summer period. Recent work by Hunke et al., (2013) to explicitly represent surface melt pond coverage based on sea ice morphology is one example of the important steps being taken toward addressing through-ice radiative input. However, buoyancy input from melt pond drainage proved to have an even greater effect on the upper ocean evolution requiring that more emphasis and validation be placed on internal sea ice processes that provide pathways for surface meltwater to drain through the ice (permeability and flaws) to the upper ocean.
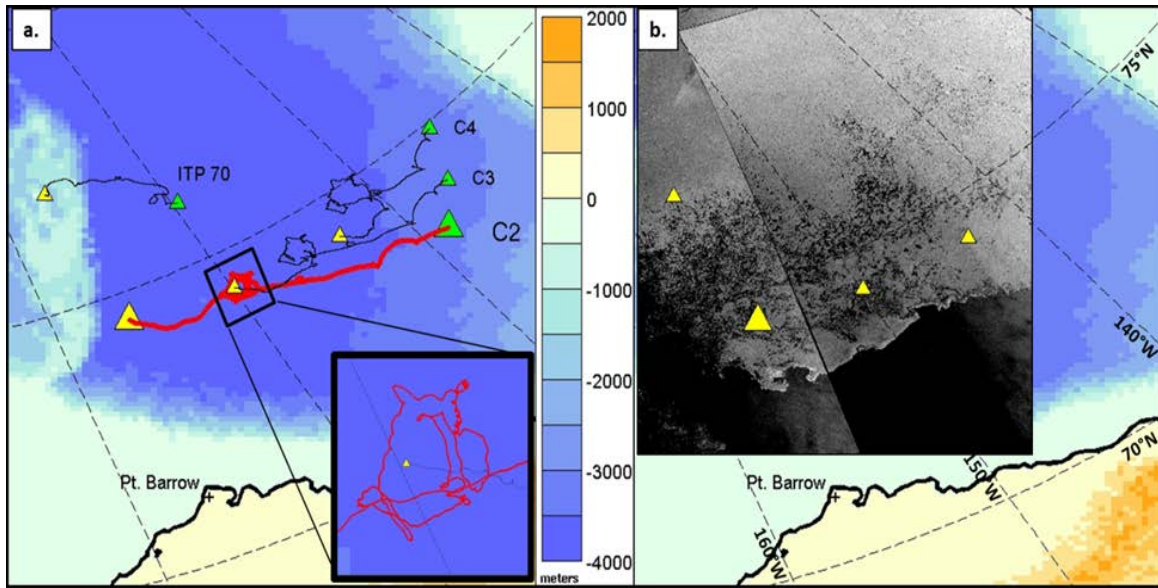
THIS PAGE INTENTIONALLY LEFT BLANK
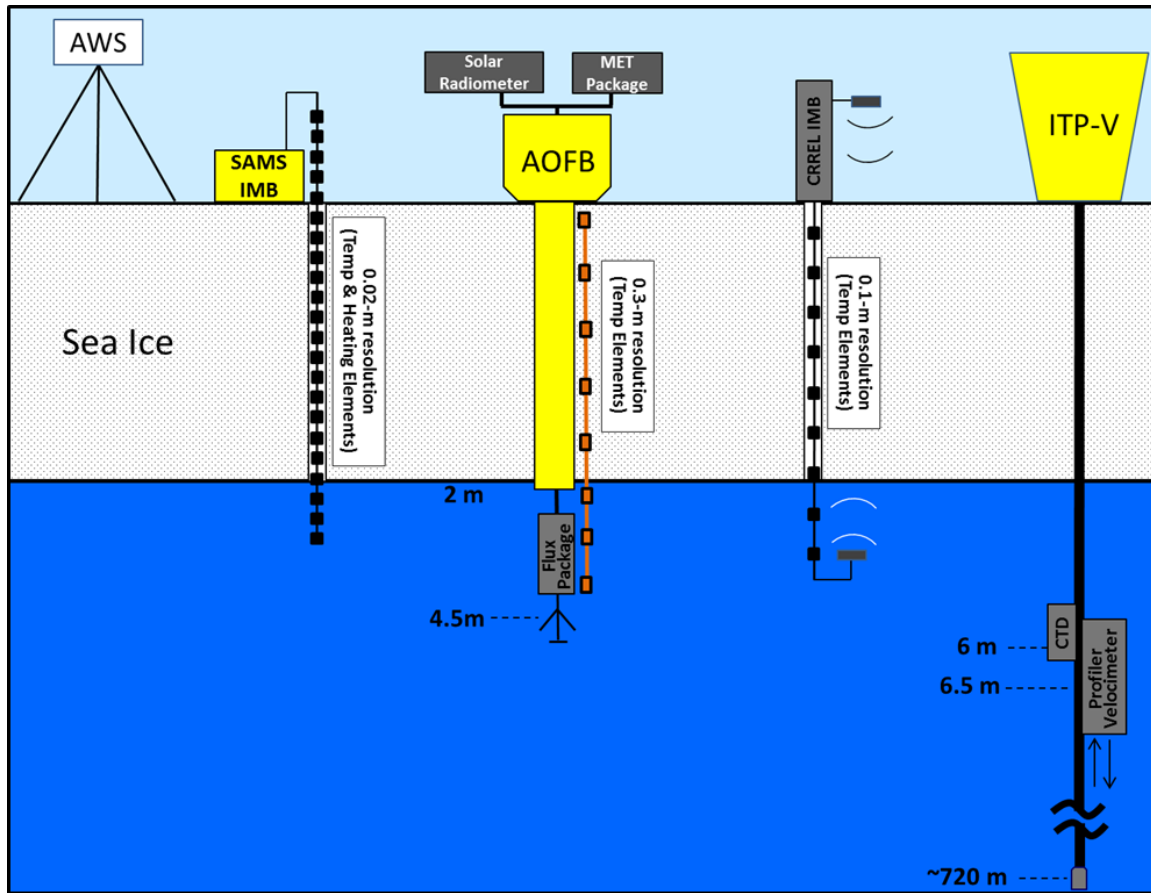
V. FIGURES
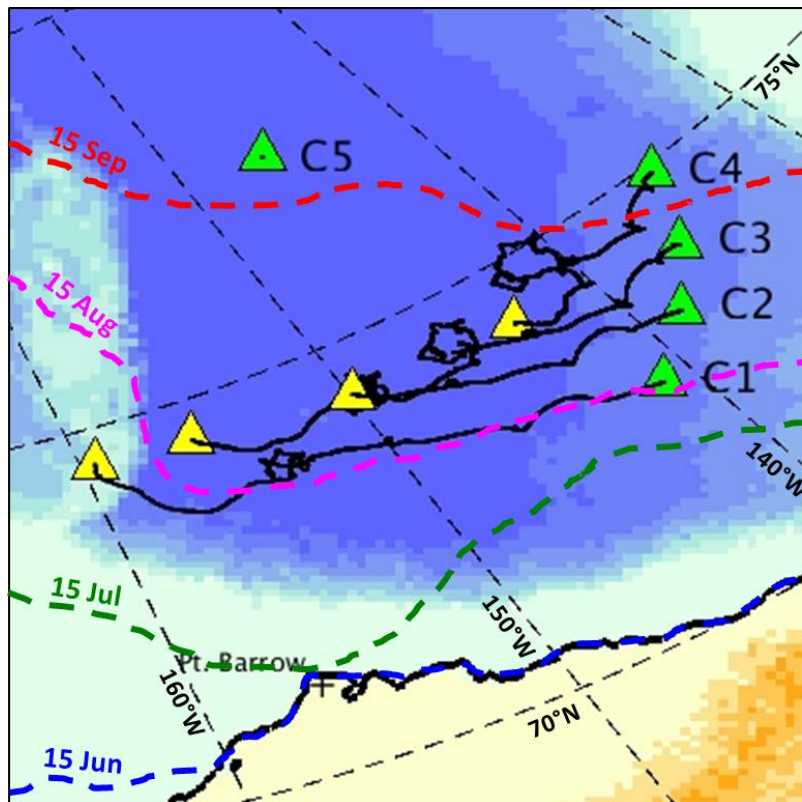

(a) Topo-bathymetric map background of the Canada Basin showing the time series start positions (green triangles) of MIZ clusters 1–4 on 30 May (YD 150), and end positions (yellow triangles) on 19 August (YD 231). The green triangle at Cluster 5 indicates the position of the ONR-KOPRI Ice Camp conducted between 9 and 14 August (YDs 221–226). Dashed lines with dates indicate the estimated position of the ice edge (< 15% ice concentration) based on Passive Microwave and RadarSat-2 SAR imagery.

Figure 1.1.   Summer Migration of the Sea Ice Edge with Marginal Ice Zone Sensors

71

(a) Topo-bathymetric map background of the Canada Basin showing the time series start positions (green triangles) of ITP-V 70 and MIZ clusters 2–4 on 30 May (YD 150), and end positions (yellow triangles) on 19 August (YD 231), with the exception of ITP-V 70 which terminated on 15 July (YD 196). Cluster 2 is the primary focus of this study (red track). (b) Merged RadarSat-2 images from 19 and 21 August (YDs 231 and 233) with end positions of clusters 2–4 and ITP-V 70. Light/white areas represent ice covered portions of the ocean.

Figure 2.1.   Drift Tracks of Marginal Ice Zone Experiment Sensor Arrays

Schematic diagram showing relative vertical positions of instruments deployed on the MIZ C2 ice floe.

Figure 2.2.　　MIZ Cluster 2 (C2) Sensor Schematic
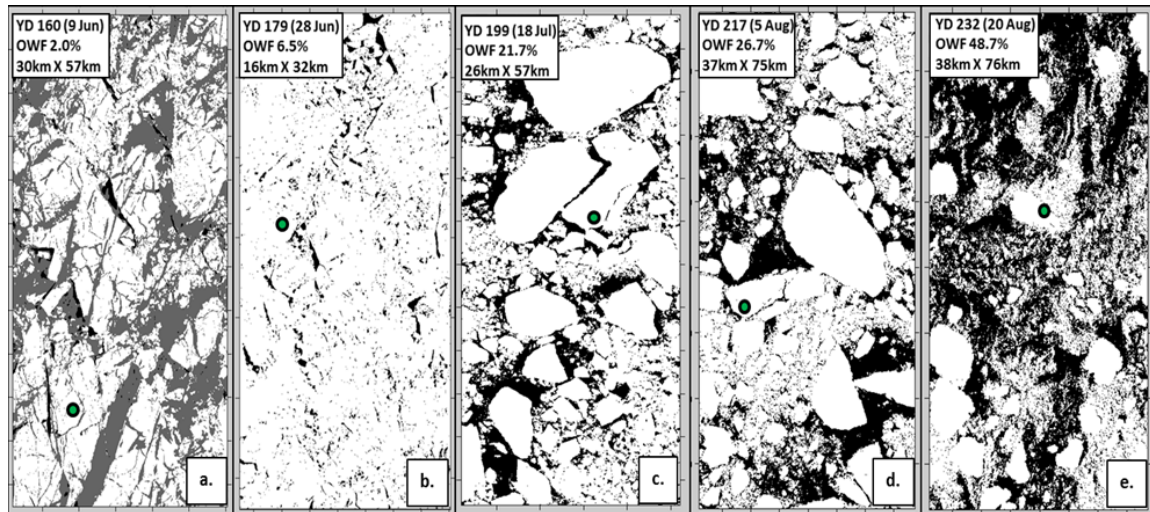
(a-e) 5 of the 21 TerraSAR-X satellite images used to estimate open water fraction (A_{OWF}) for the ocean radiative flux calculation. The location of the MIZ cluster 2 (C2) instrument array is represented by the green circle. These images document the progression of the MIZ C2 locale from compact sea ice in late spring (a) toward a marginal ice zone condition with large open water areas at the end of summer (e).

Figure 2.3.   Open Water Fraction Estimates from SAR Satellite Imagery
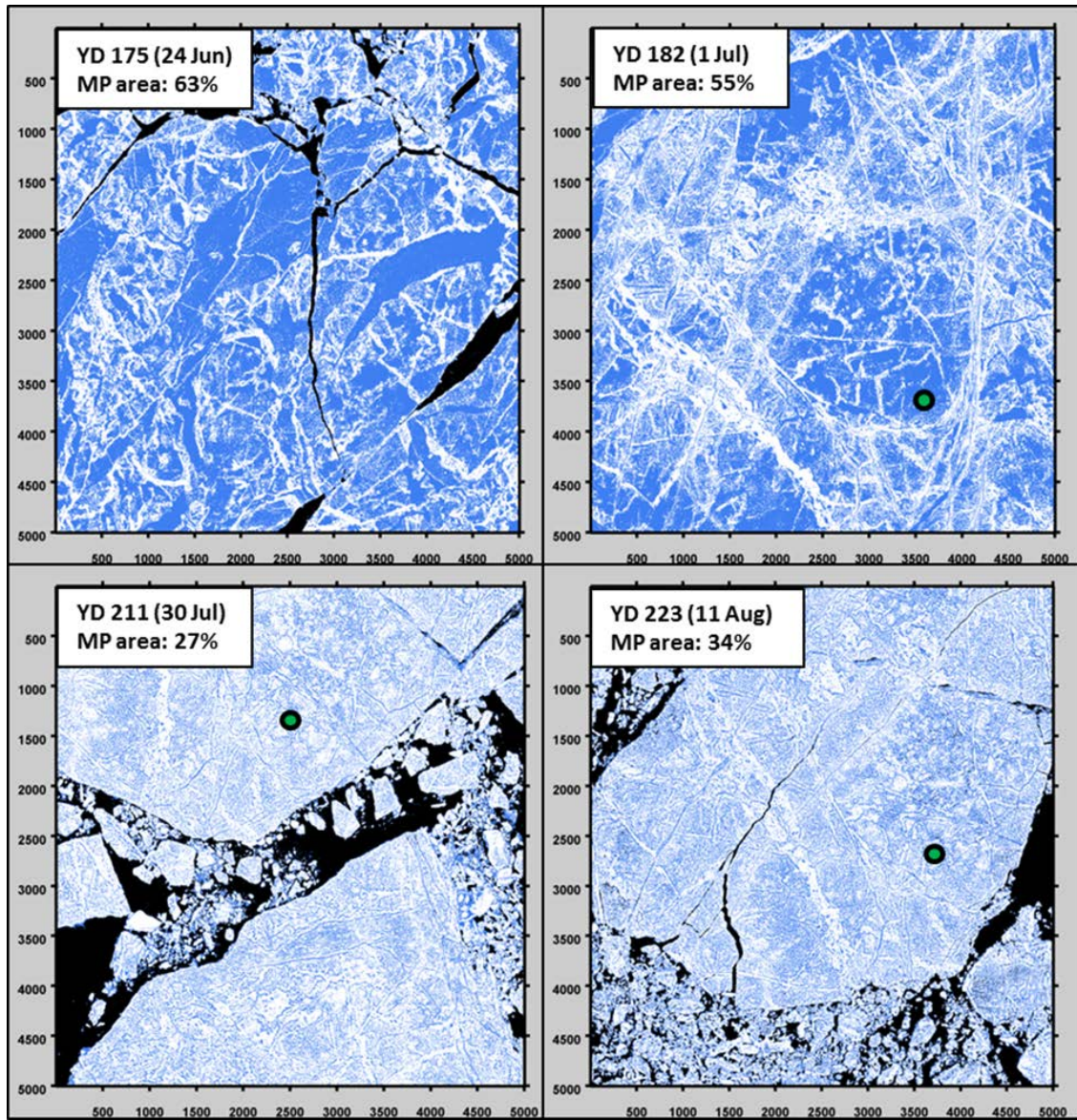
(a-d) False color visible satellite images (1-m res.) showing the evolution of melt pond coverage (light blue) at MIZ C2 (green dots) and were used to estimate the through-ice component of radiative flux to the ocean.

Figure 2.4.   Melt Pond Fraction Estimates from Visible Satellite Imagery
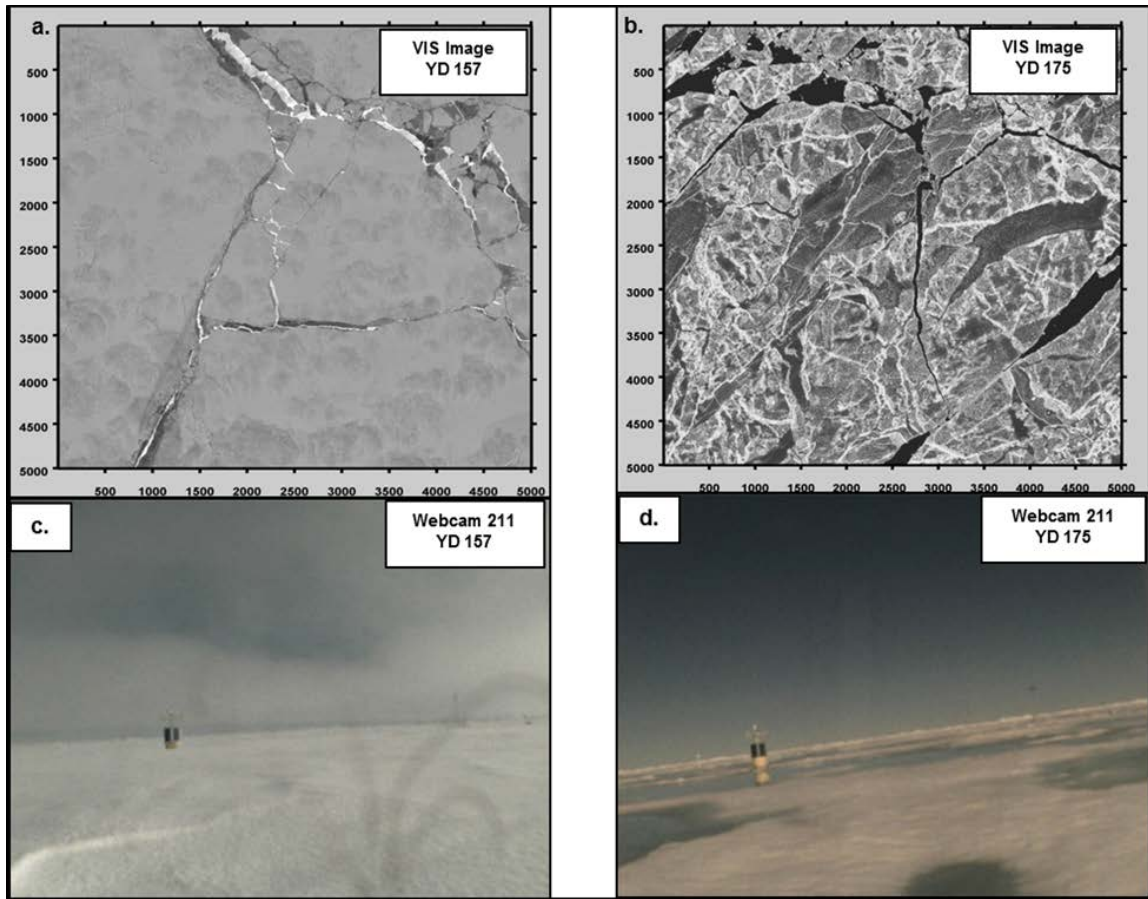
(a, b) 1-m resolution visible satellite imagery and (c, d) webcam images near C2 showing significant melt pond development during Stage I. The AOFB instrument is visible in the webcam images.

Figure 2.5.　　　Images of Melt Pond Development in Early Summer
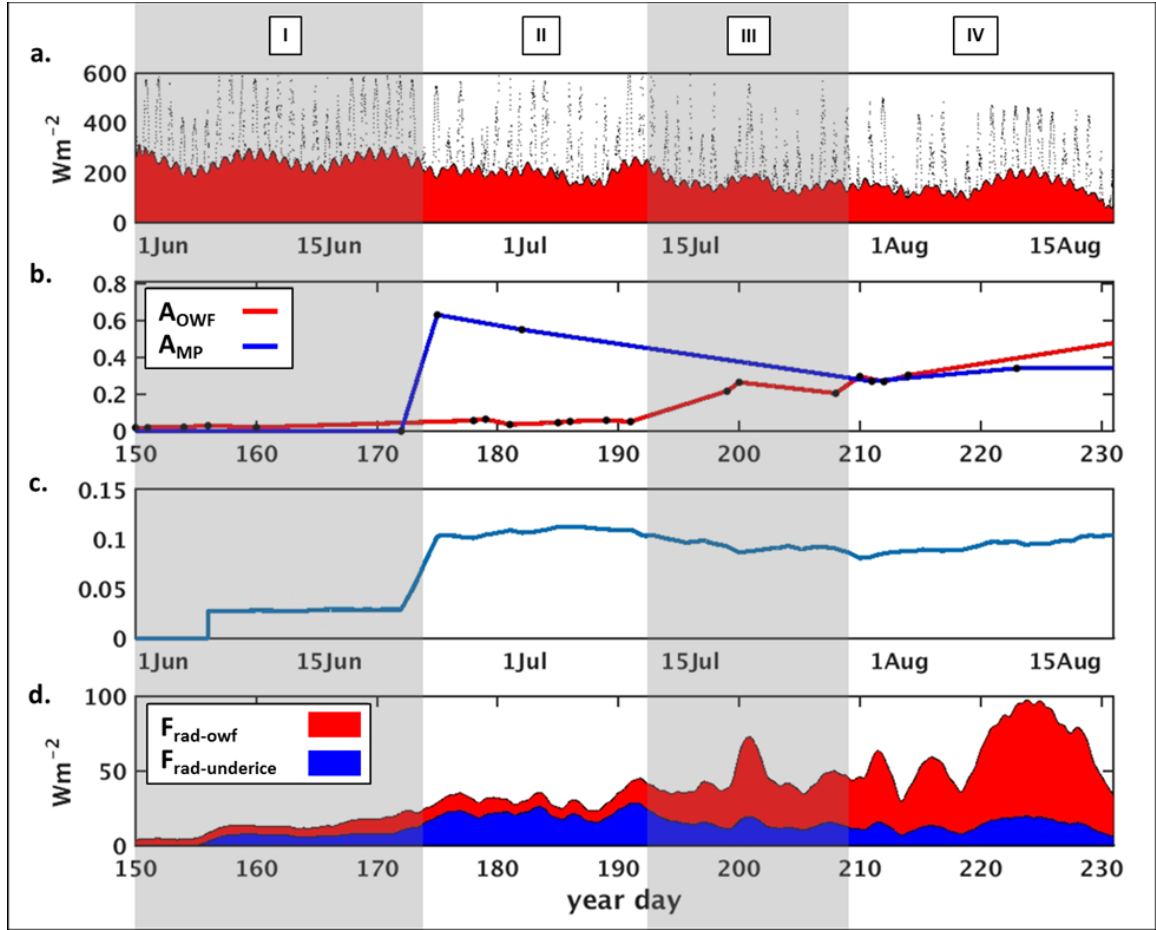
(a) 3-day averaged (red area) and 15-min (black dots) incident solar irradiance observations, (b) linear interpolation of open water (A_{OWF}, red) and melt pond (A_{MP}, blue) fractions based on SAR and visible satellite imagery observations (black dots), (c) estimated sea ice transmittance ($F_{rad-underice}/F_{rad}$), and (d) 3-day averaged open-water ($F_{rad-owf}$) and under-ice ($F_{rad-underice}$) radiative fluxes into the ocean. Time periods of the IOBL-OML stage (I-IV) evolution are gray shaded and labeled on all overview figures.

Figure 2.6. Air-Ocean Shortwave Radiation Overview at MIZ C2
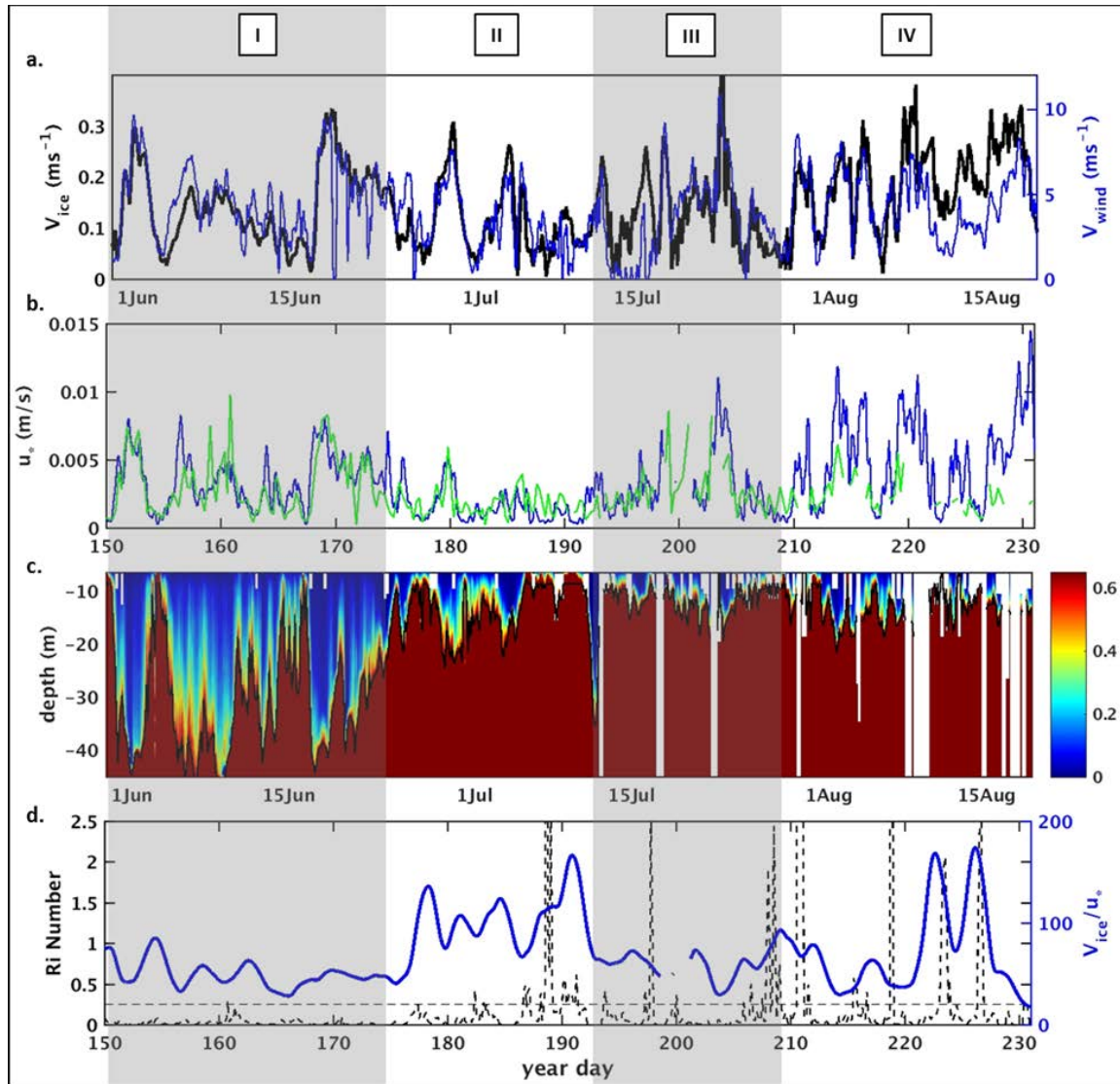
(a) 2 m winds (blue) and ice speeds (black), (b) 4.5 m (blue) and 6.5 m (green) turbulent friction velocities, (c) bulk Richardson number (Ri_{bulk}) showing estimated turbulent penetration ($Ri_c = 0.65$), and (d) the ratio of ice speed to 4.5 m friction velocity ($V_{ice}/u_{*(4.5\,m)}$) (blue) and the 5.5 m Richardson number (Ri) (black).

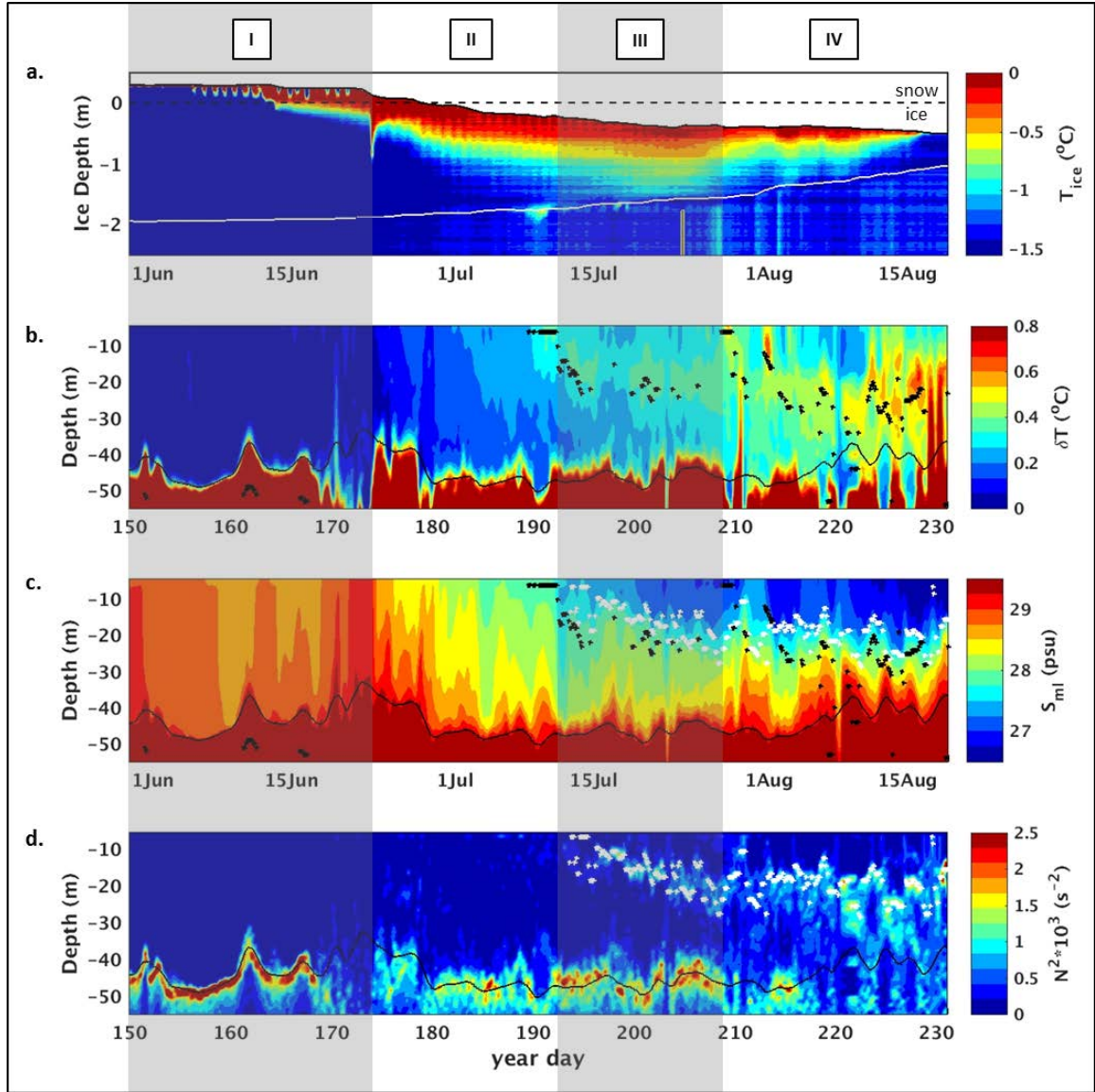Figure 2.7.   Ice-Ocean Boundary Layer Processes Overview at MIZ C2

(a) IMB ice temperatures with top (black) and bottom (white) interfaces, (b) upper ocean departure from freezing (δT) and depth of the NSTM (black dots), (c) upper ocean salinity, depth of summer halocline (white dots), and depth of NSTM, and (d) upper ocean N^2 and summer halocline (white dots). In Figs. 2.8b, 2.8c, and 2.8d, the black line between 40 and 50 m depth represents the winter pycnocline as defined by the 1023.5 kgm^{-3} isopycnal.

Figure 2.8.   Ice-Ocean Properties Overview at MIZ C2

1-D Heat Budget Overview at MIZ C2 to estimate the magnitude of ocean absorbed solar radiation (source) and how it is redistributed between latent heat losses (sink #1) and heat storage (sink #2). (a) Winter mixed layer heat budget: 3-day averaged time series of shortwave source term $Q_{rad\text{-}ocn}$ (black line), wML heat storage sink term Q_{wML} (gray), and latent heat sink term Q_{lh} (blue). (b) Summer mixed layer heat budget: 3-day averaged time series of shortwave source term $Q_{rad\text{-}ocn}$ (black line), sML heat storage sink term Q_{sML} (green), and latent heat sink term Q_{lh} (blue). (c) The 3-day averaged latent heat flux term F_{lh} (blue) and OML heat storage flux terms F_{wML} (gray) and F_{sML} (green), and (d) the 3-day averaged ocean radiative flux term $F_{rad\text{-}ocn}$ (red), sum of latent heat and OML heat storage flux terms $F_{lh} + F_{oml}$ (gray line), and turbulent heat fluxes at 4.5 m and 6.5 m ($F_{H(4.5m/6.5m)}$, black and green lines, respectively).

Figure 2.9.   1-D Heat Budget Overview at MIZ C2

80
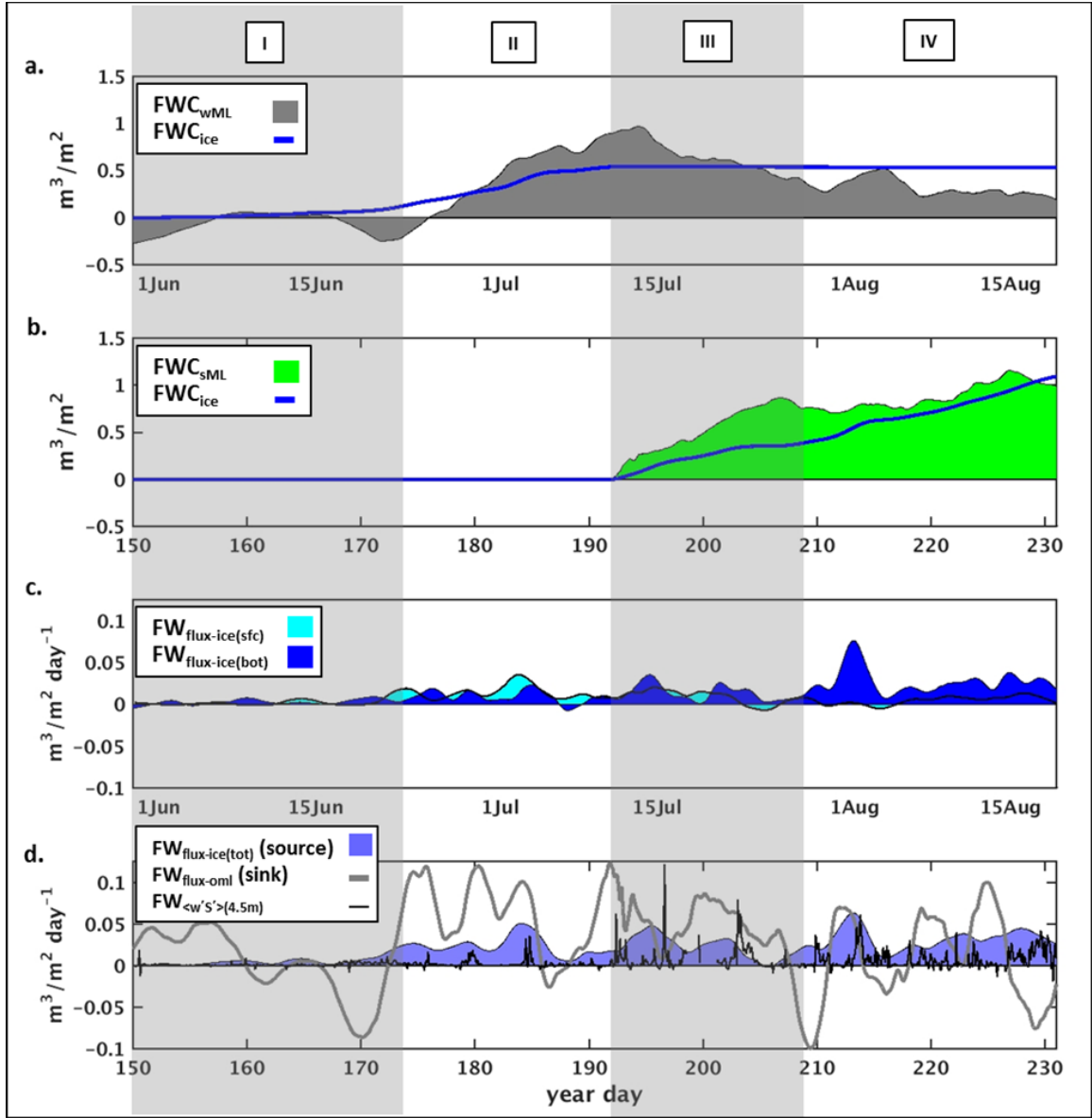
(a) Winter mixed layer freshwater budget: 3-day averaged integrated freshwater flux from top and bottom ice melting term FWC_{ice} (source term, blue line) and wML freshwater storage sink term FWC_{wML} (gray). (b) Summer mixed layer freshwater budget: 3-day averaged integrated freshwater flux from top and bottom ice melting term FWC_{ice} (source term, blue line) and sML freshwater storage sink term FWC_{sML} (green). (c) 3-day averaged freshwater flux from melting of the sea ice surface ($FW_{flux-ice(sfc)}$, light blue) and the sea ice bottom ($FW_{flux-ice(bot)}$, dark blue). (d) 3-day averaged total freshwater flux from the sea ice ($FW_{flux-ice(tot)}$, purple area), OML freshwater storage fluxes ($FW_{flux-oml}$, gray line), and freshwater fluxes inferred from turbulent salt fluxes at 4.5 m ($F_{<w'S'>(4.5m)}$, black line).

Figure 2.10.   1-D Freshwater Budget Overview at MIZ C2

81
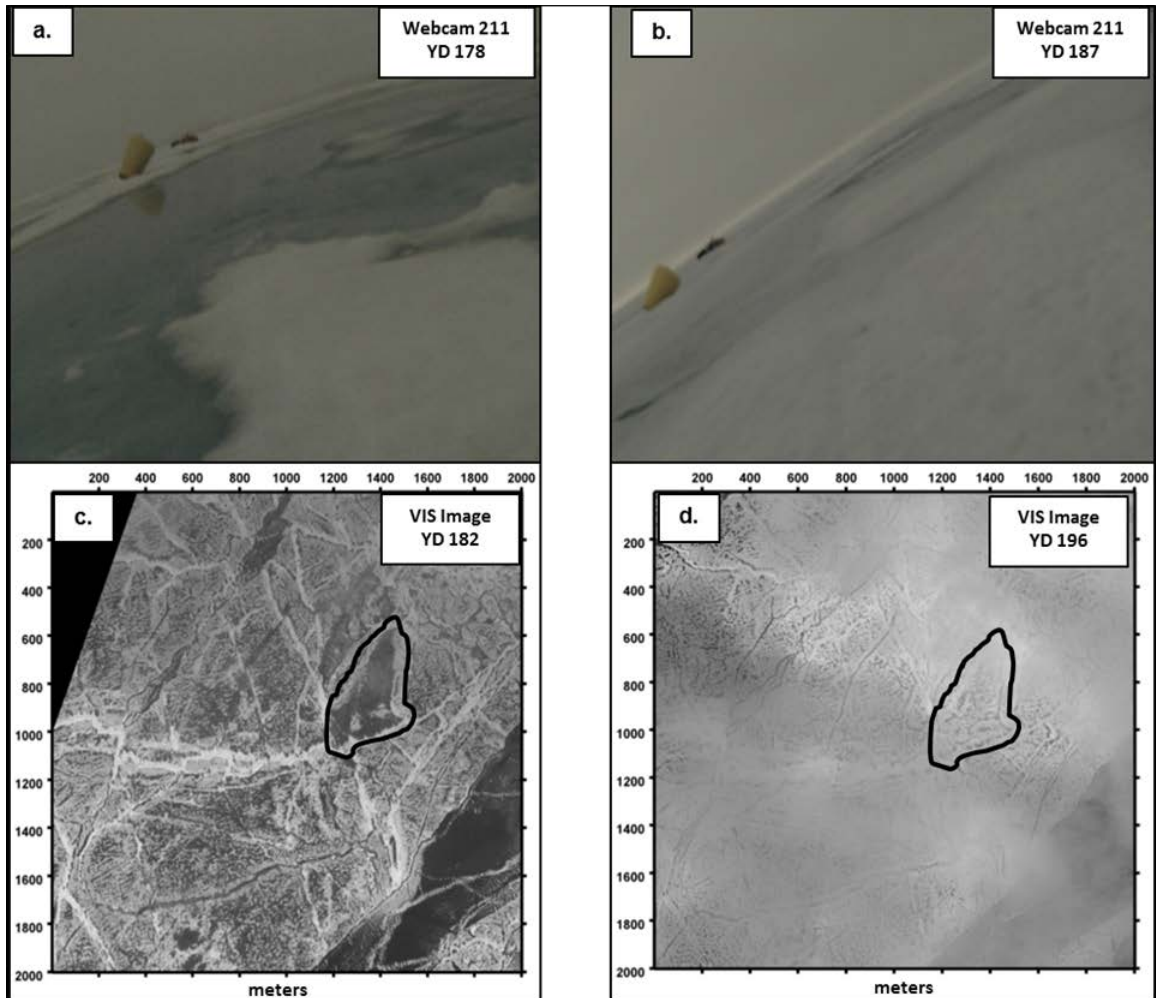
Webcam images from C2 showing (a) peak melt pond coverage on YD 178, and (b) full melt pond drainage by YD 187. Visible satellite imagery taken on YD 182 (c) and YD 196 (d) also show extensive melt pond drainage in the areas surrounding C2. The area outlined in black in (c) and (d) highlights a large melt pond that drained by YD 196.

Figure 2.11.   Images of Melt Pond Drainage at MIZ C2
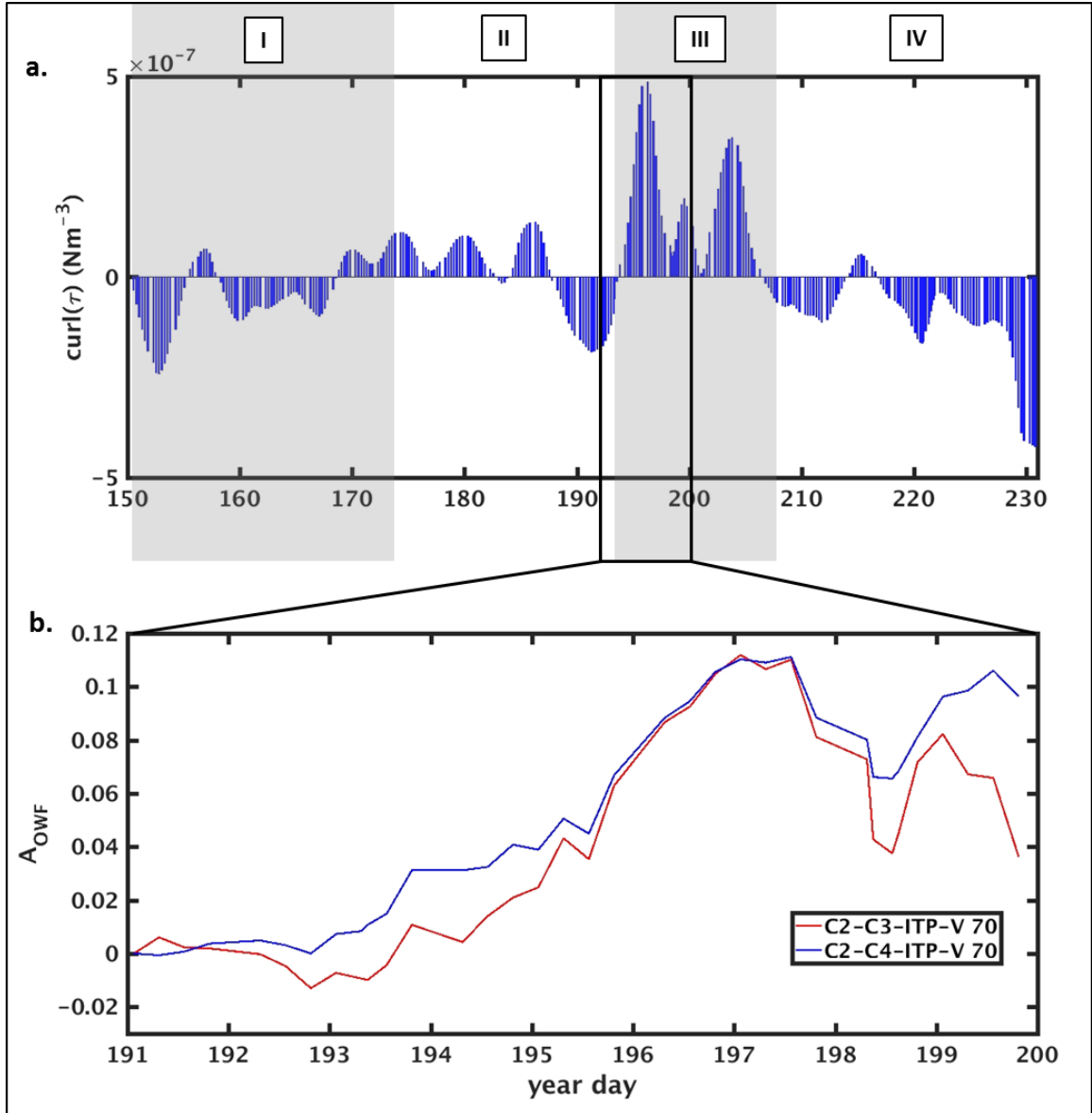
a) 2-day averaged wind stress curl (curl(τ)) estimated from MIZ C2-C4 and ITP-V 70 observations in the Canada Basin. (b) Estimation of open water fraction (A_{OWF}) from divergence between the MIZ sensors using the triangle area differencing method (Stanton et al. 2012). Triangle area differencing was calculated on C2, C3, and ITP-V 70 (red) and C2, C4, and ITP-V 70 (blue) every 6 h.

Figure 2.12.   Wind Stress Curl and Sea Ice Divergence from Observations

83
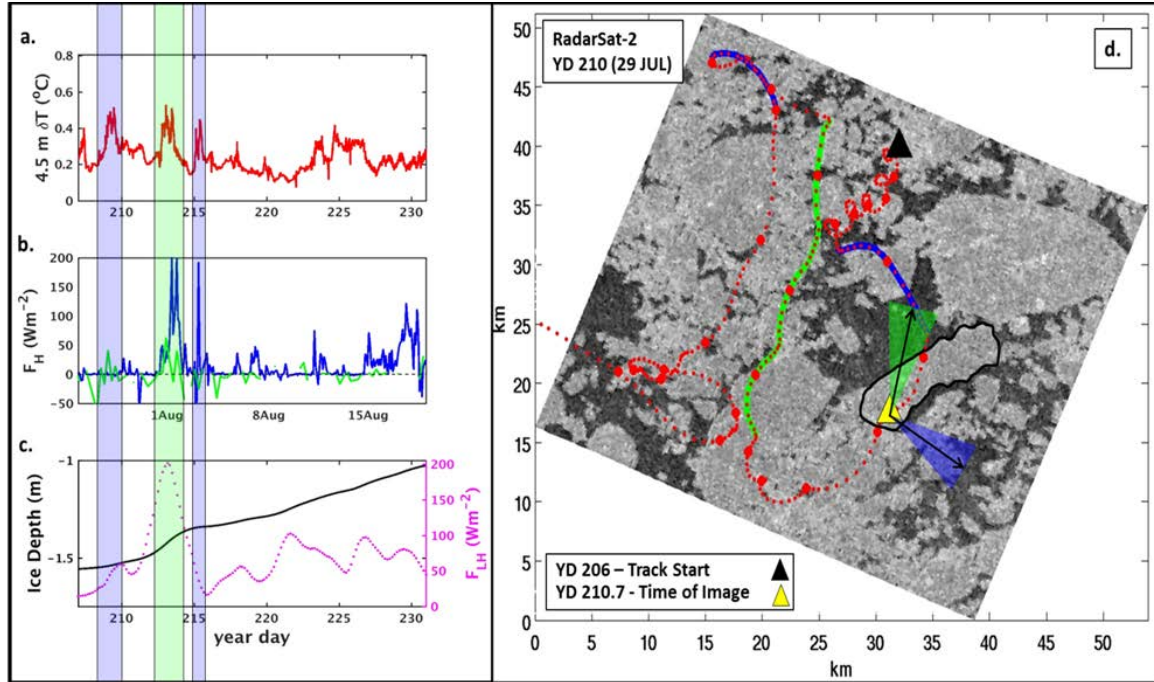
(a) 4.5 m δT, (b) 4.5 m (blue) and 6.5 m (green) turbulent heat fluxes, (c) 3-day averaged sea ice bottom interface depth (black) and latent heat fluxes (magenta dots), and (d) RadarSat-2 image (YD 210.7) overlaid with MIZ C2 GPS track (red dots) between YD 206 (black triangle, start time of time series plots in Figs. 2.13a, 2.13b, and 2.13c) and YD 216. The time periods of interest are color coded in blue and green along the GPS track and on the corresponding supporting plots (a, b, c). To determine the direction of ice motion during the different time periods, color coded vector triangles with direction arrows are plotted over the location of C2 at the time the image was acquired (yellow triangle).

Figure 2.13.   MIZ Upstream Conditions (CASE I): Spatially
Heterogeneous Upper Ocean
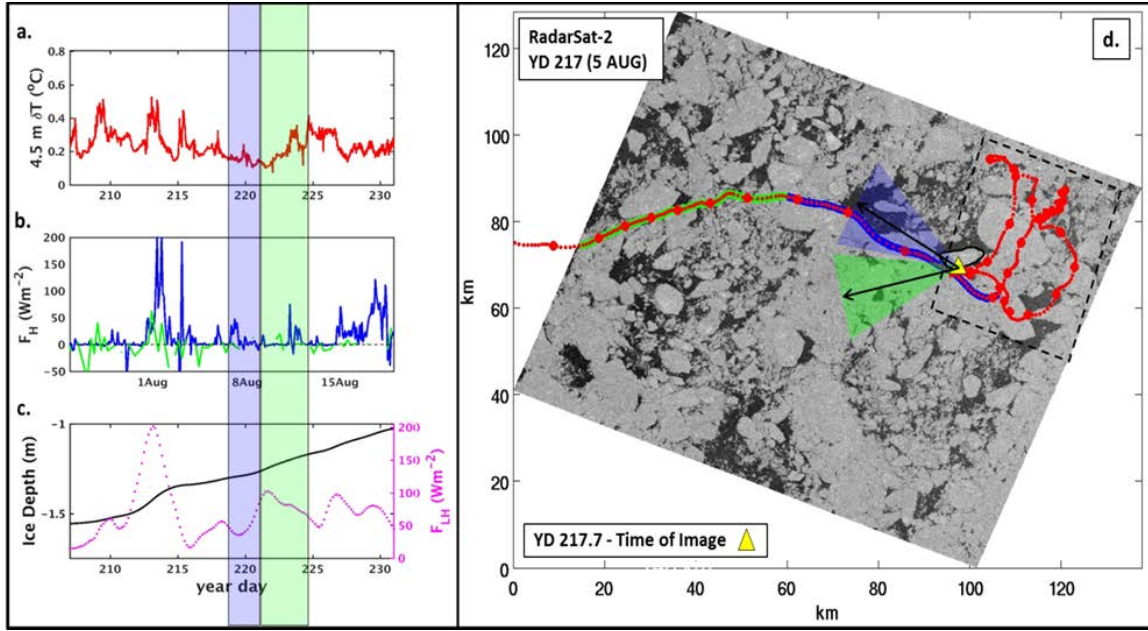
Same format as Fig. 2.13 for a RadarSat-2 image taken on YD 217.

Figure 2.14.   MIZ Upstream Conditions (CASE II): Spatially
Homogeneous Upper Ocean
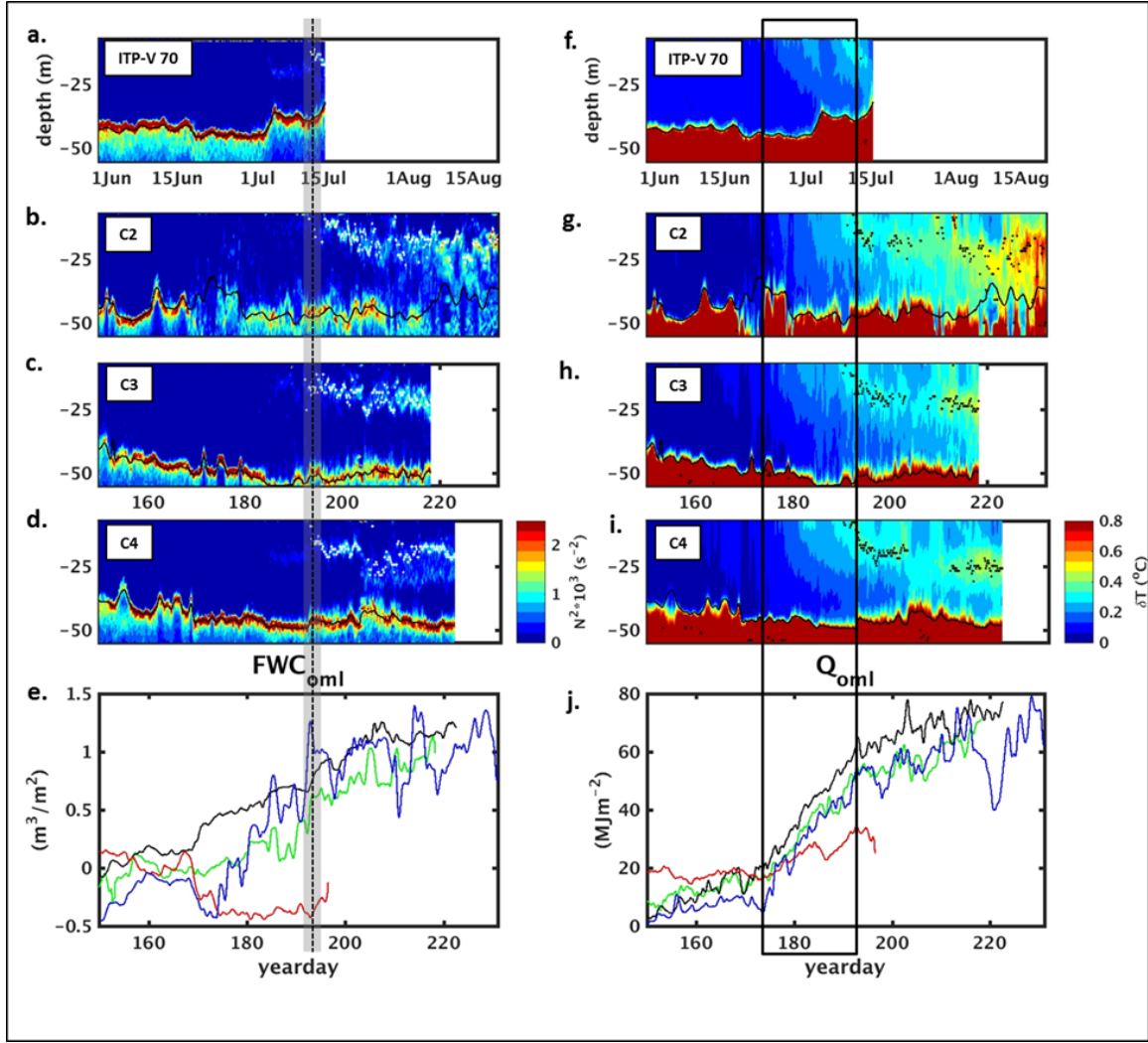
(a) ITP-V 70, (b) C2, (c) C3, and (d) C4 of upper ocean N^2 and summer halocline depth (white dots), and (e) OML freshwater storage for ITP-V 70 (red), C2 (blue), C3 (green), and C4 (black). Vertical dashed line indicates date of summer halocline development (~YD192). On the right hand side (f, g, h, i), corresponding upper ocean δT and NSTM (black dots), and (j) OML heat storage are presented. Black box highlights the Stage II period of the summer evolution (YDs 173–192).

Figure 2.15.   Regional Comparisons of the Summer Mixed Layer, NSTM, Heat Balance, and Freshwater Balance
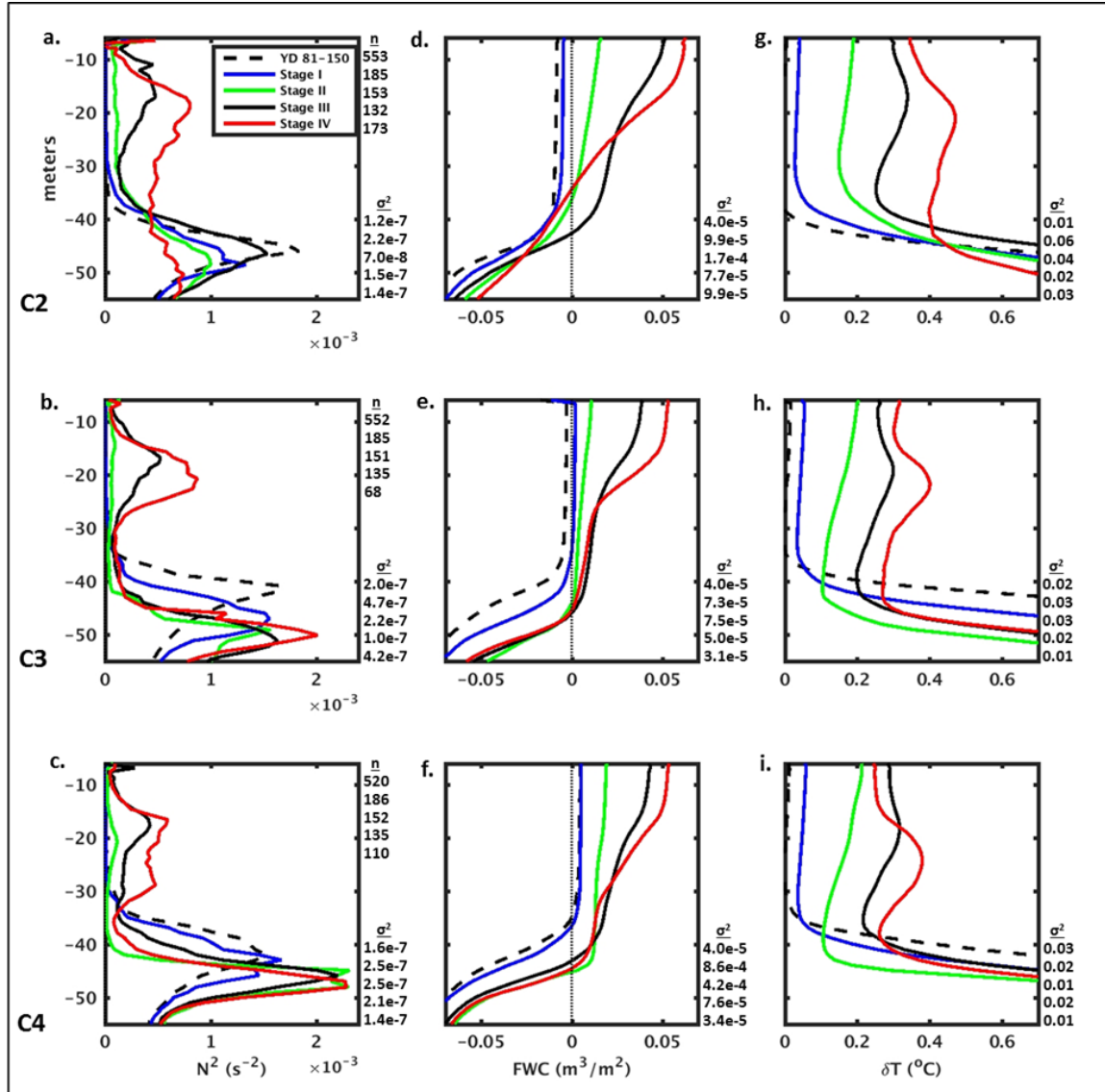
Upper ocean profiles of stage-averaged (a, b, c) N^2, (d, e, f) freshwater storage (*FWC*), and (g, h, i) δT for clusters 2–4 (see legend). Rows correspond to observations from C2, C3, and C4, respectively. Number of profiles (n) and the mean variance statistics (σ^2) across all depths for each stage are provided on the right side of the plot.

Figure 2.16.   Regional Comparisons of Summer Evolution Stage Profiles
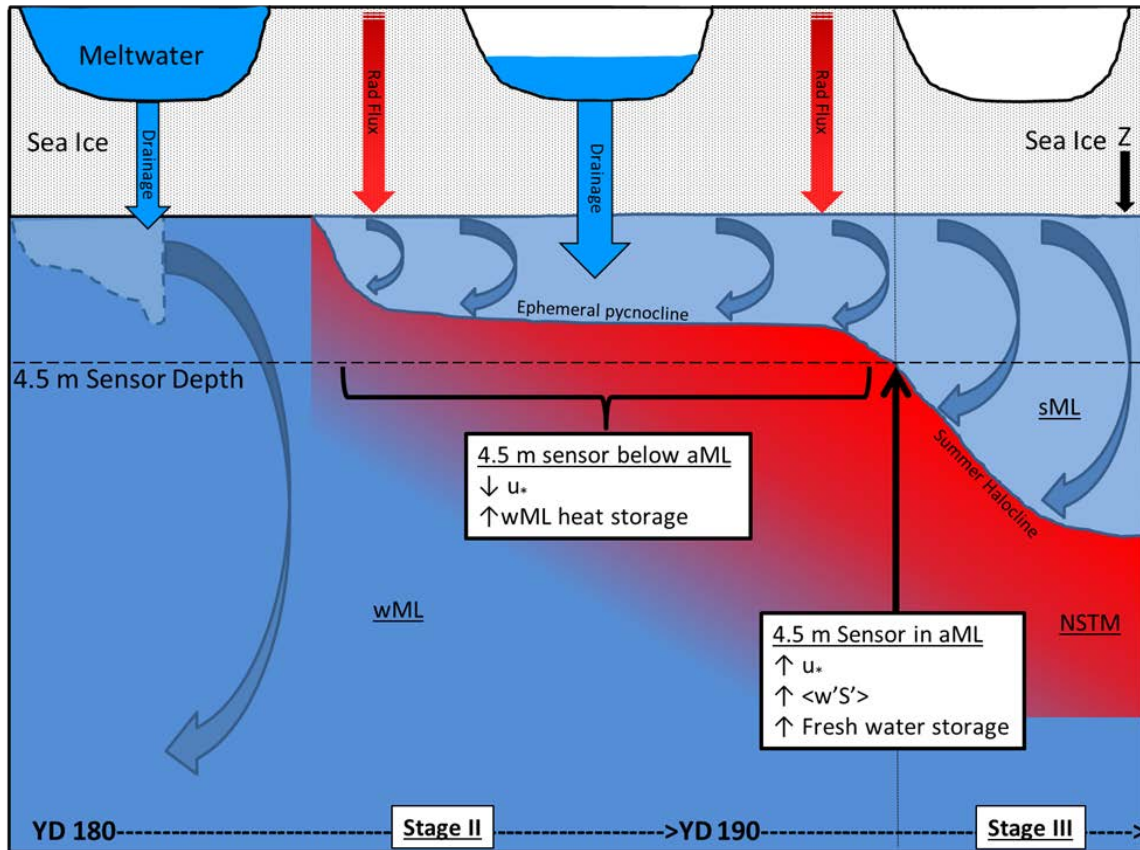
A depiction of the sea ice and the upper ocean showing the influence drained melt pond water had on the IOBL-OML system between YDs 180 and 195. Initially, small amounts of meltwater are easily mixed out during wind events (between about YD 180 and 185, left side of cartoon). As meltwater input to the OML increased, primarily due to melt pond drainage, the active mixing layer (aML) contracts resulting in substantial wML heat storage gain, and development of the NSTM (middle portion of cartoon). Following melt pond drainage, the sML develops during the subsequent wind event as turbulent processes deepened the fresh, near-surface mixing layer below the shallowest sensor (4.5 m), resulting in immediate increases to u_*, salt fluxes ($<w'S'>$), and sML freshwater storage (right side of cartoon).

Figure 2.17.   Process Schematic of Summer Mixed Layer and NSTM Development
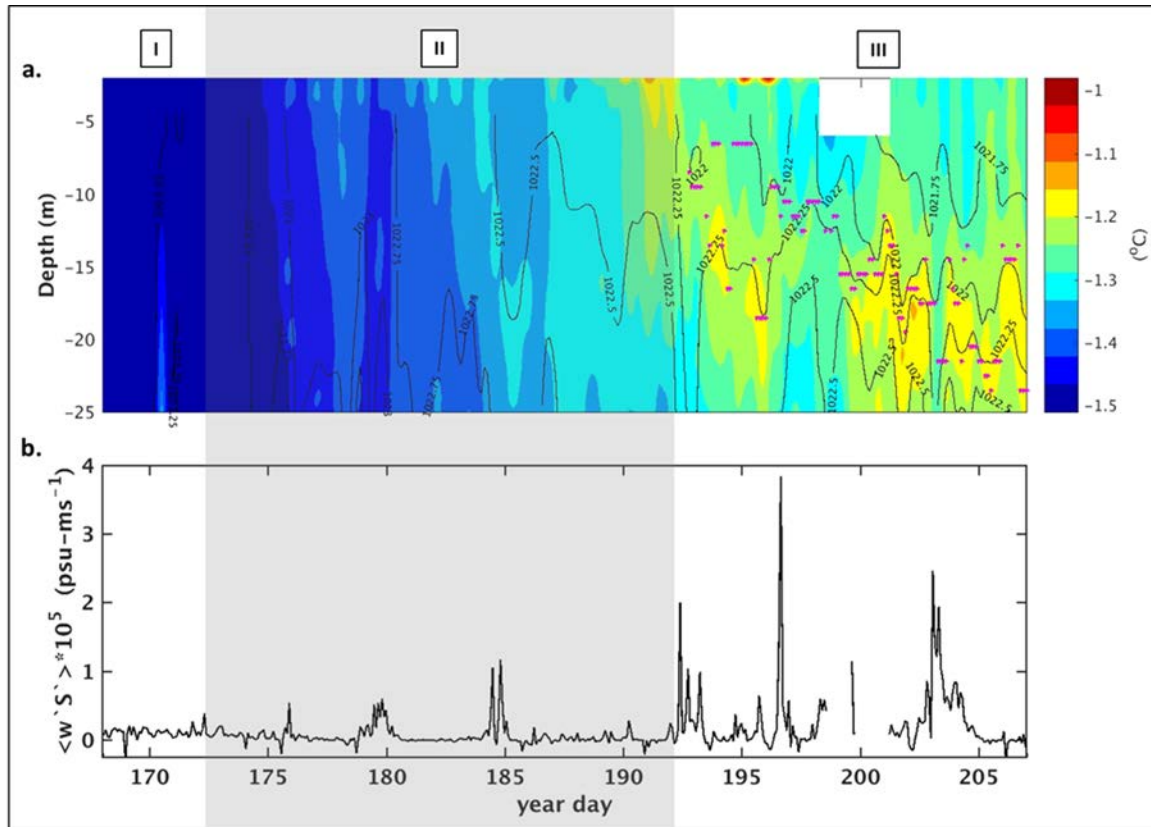
(a) Ocean temperature above 25 m plotted to include the AOFB temperature string data from 2.3-4.5 m. Black lines are isopycnals every 0.25 kgm^{-3} and magenta lines indicates the near-surface N^2 maximum defining the developing summer halocline. Missing observations near the interface between YDs 198–201 were due to a temporary power outage at AOFB 33. Bottom panel (b) is turbulent salt flux from the 4.5 m sensor. Large turbulent salt fluxes (YDs 192 and 196) are observed following enhanced warming at 2.3 m suggesting these features were fresh meltwater near the ice-ocean interface which was mixed down to form the summer halocline.

Figure 2.18.   Turbulent Salt Fluxes Following Melt Pond Drainage
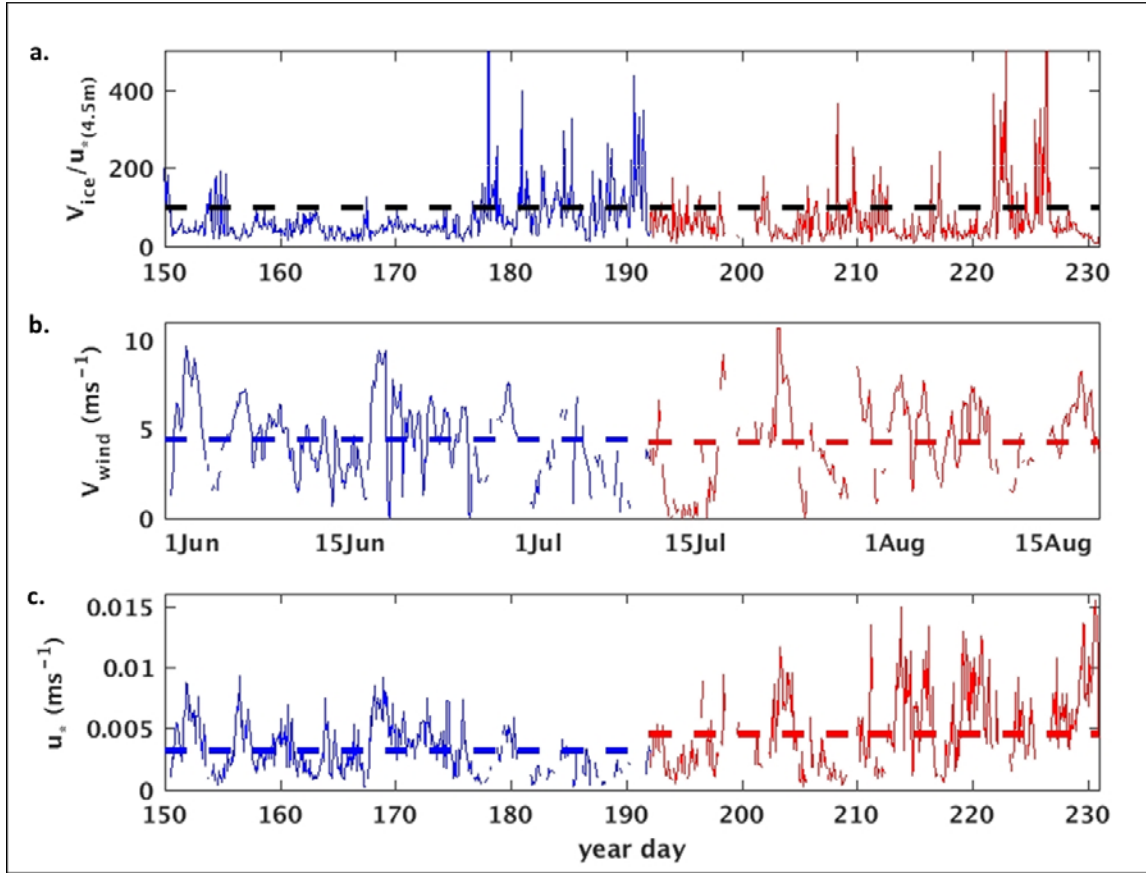
(a) Pre-sML (blue) and post-sML (red) ratio of ice speed to 4.5 m friction velocity (V_{ice}/u_*) with critical value of 100 indicated (black dashed line). Values of $V_{ice}/u_* > 100$ indicate periods when the 4.5 m turbulence sensor was decoupled from the ice-ocean interface stresses by near-surface meltwater. (b) 2 m winds and, (c) friction velocity with $V_{ice}/u_* > 100$ removed. Dashed lines indicate the average pre-sML (blue) and post-sML (red) values.

Figure 2.19.   Turbulent Stress Comparisons before and after Summer
Mixed Layer Formation
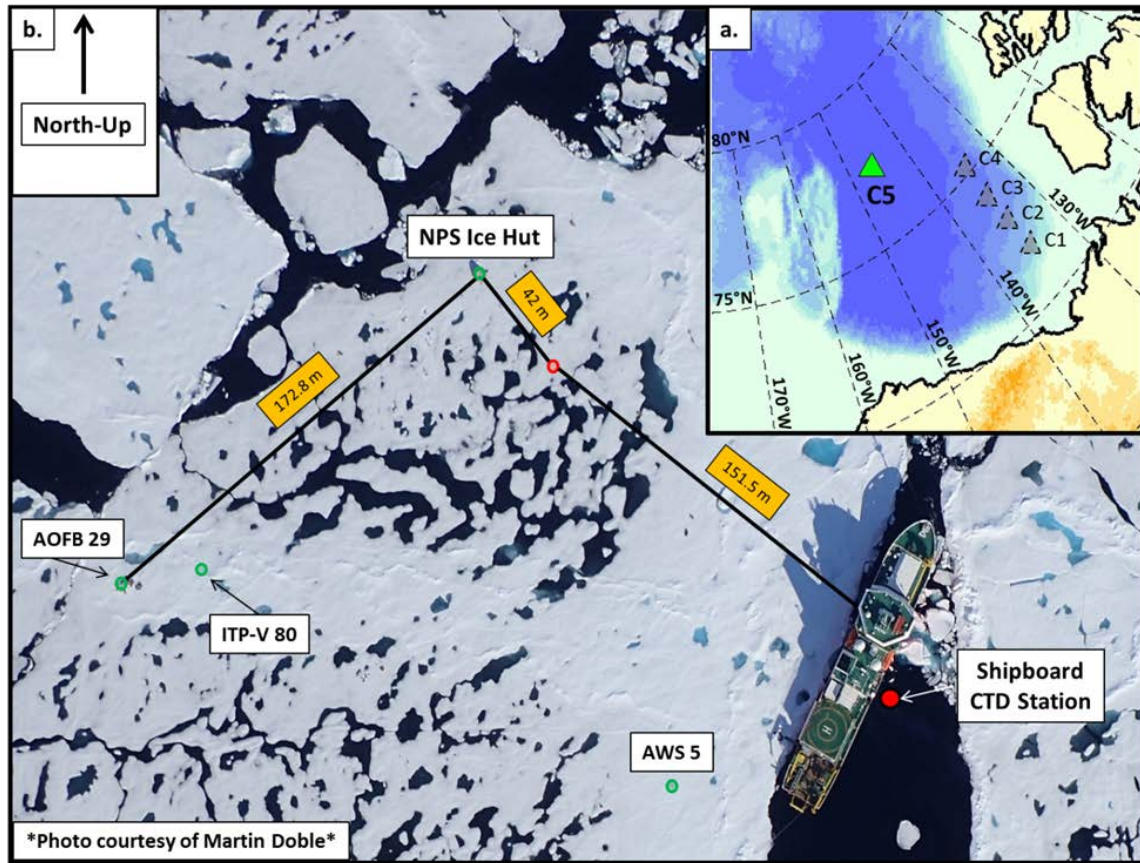
(a) Topo-bathymetric map background of the Canada Basin showing the location of the joint ONR-KOPRI Ice Camp at MIZ Cluster 5 between 9 and 14 August 2014 (green triangle). Also shown are the initial positions of MIZ Clusters 1–4 deployed in early spring. (b) Image of the ONR-KORPI Ice Camp taken from a Maritime Helicopters BELL 206 at 600 m. Ice Camp image is annotated with the locations of the on-ice instruments to include the Autonomous Ocean Flux Buoy (AOFB) 29, Automated Weather Station (AWS) 5, the R/V Araon CTD station, Ice-tethered Profiler - V 80 (ITP-V 80), and NPS Ice Hut used to deploy the Turbulence Frame.
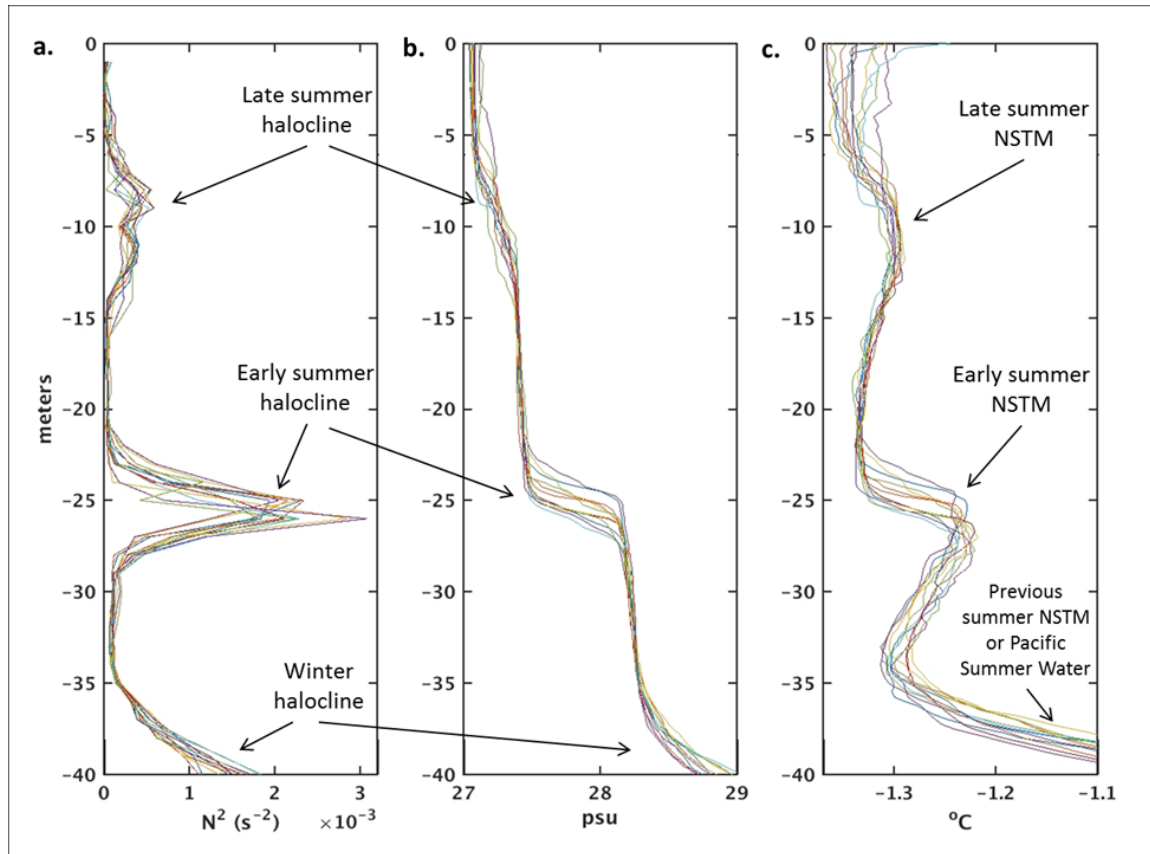
Figure 3.1.   ONR-KOPRI Ice Camp Overview at MIZ Cluster 5 (C5)
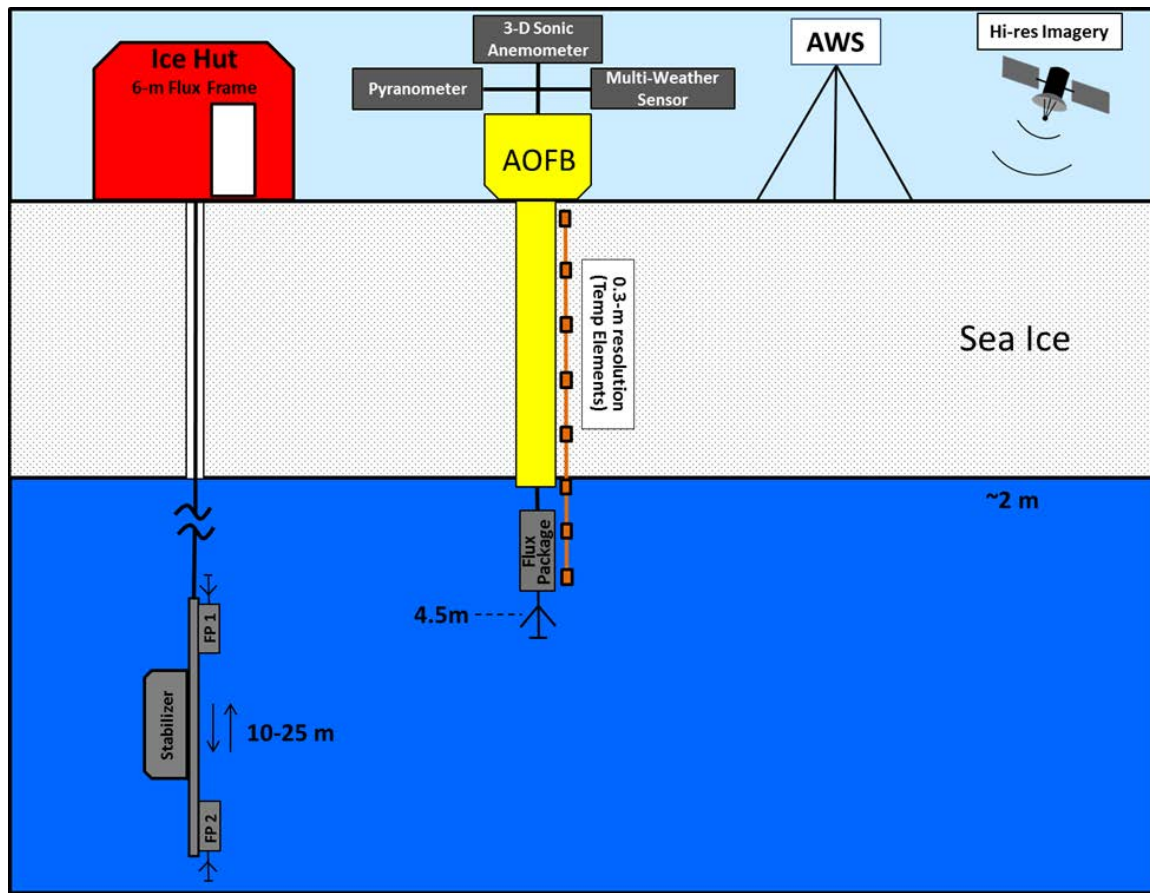
Sensor schematic (vertical view) of the on-ice instruments at the MIZ-KOPRI Ice Camp shown on Fig. 3.1b.

Figure 3.2.   MIZ C5 Sensor Schematic

R/V Araon CTD profiles of (a) N^2, (b) salinity, and (c) temperature for the last two days of the MIZ-KOPRI Ice Camp (YDs 223.8-225.8). Peaks in temperature and stratification highlight the respective levels of the early and late summer haloclines and NSTMs.

Figure 3.3.   Defining the Early and Late Summer Halocline and NSTM

93
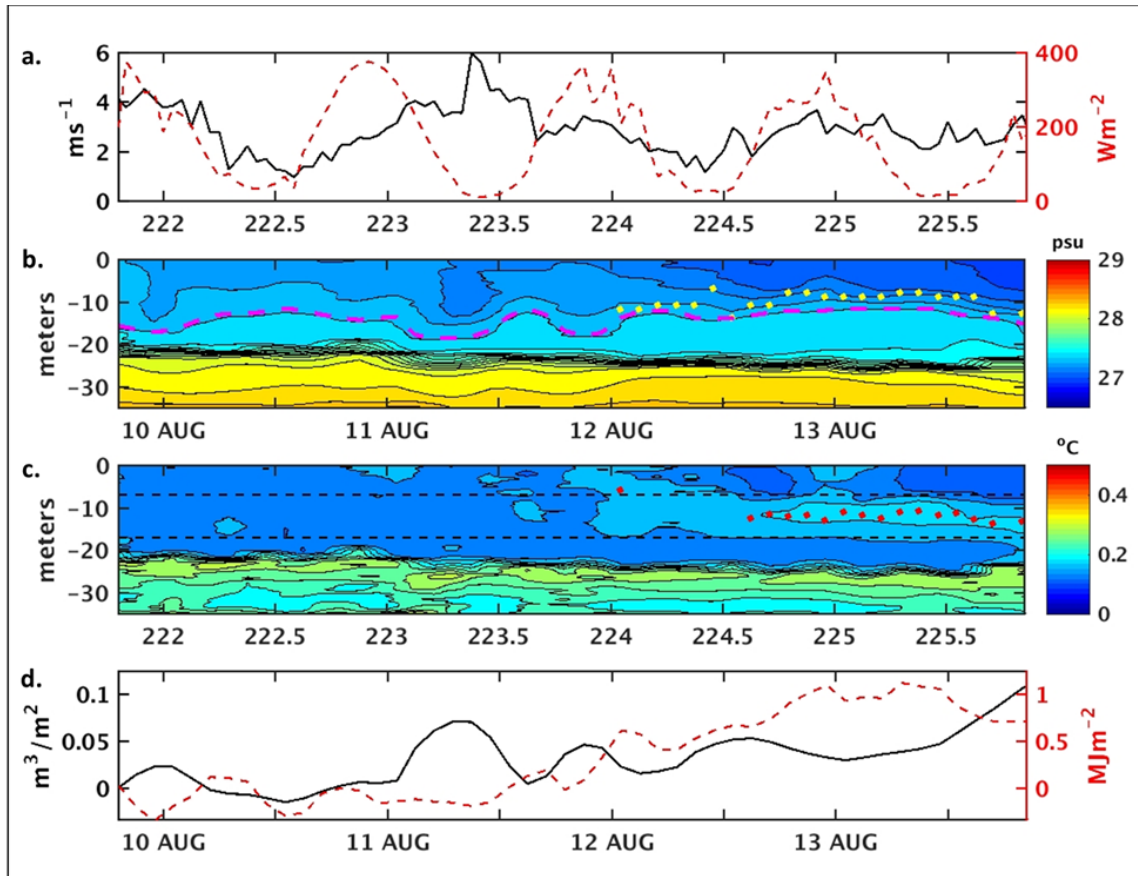
(a) 2 m wind speed (black) and incoming solar radiation from AWS 5 and AOFB 29. (b) Salinity collected from R/V Araon CTD casts binned every 0.25-m with the near-surface N^2 maximum (yellow dots) and 1022 kgm^{-3} isopycnal (magenta) overlaid to show the lower integration limit for freshwater content calculations (*FWC*). (c) 0.25-m binned temperature above freezing data with depth of the late summer NSTM (red dots) and NSTM layer control volume (black dashed). (d) Cumulative *FWC* (black) in the surface mixed layer and cumulative heat storage (red dashed) in the NSTM layer.
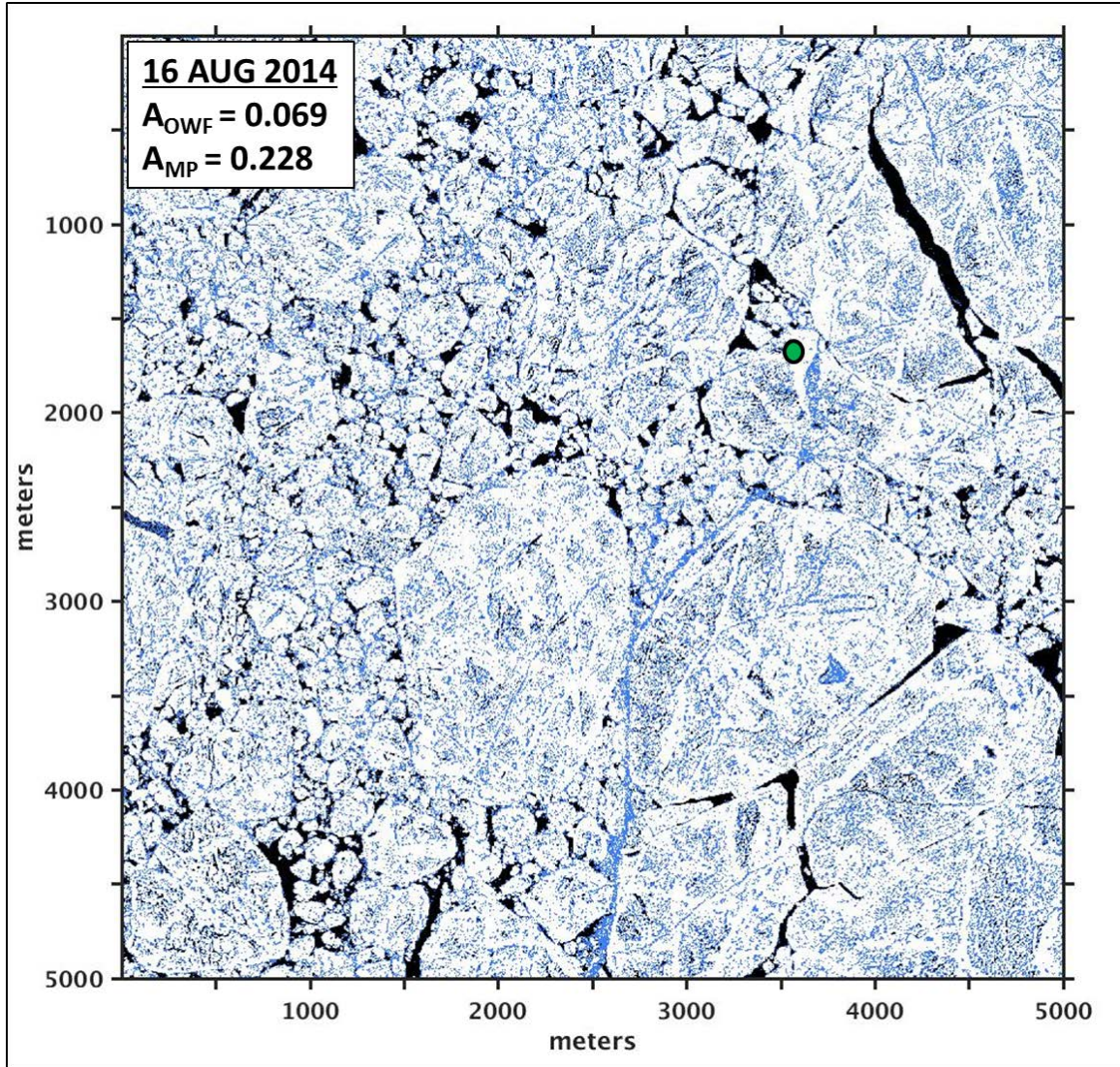
Figure 3.4.   MIZ-KOPRI Ice Camp In-situ Observations
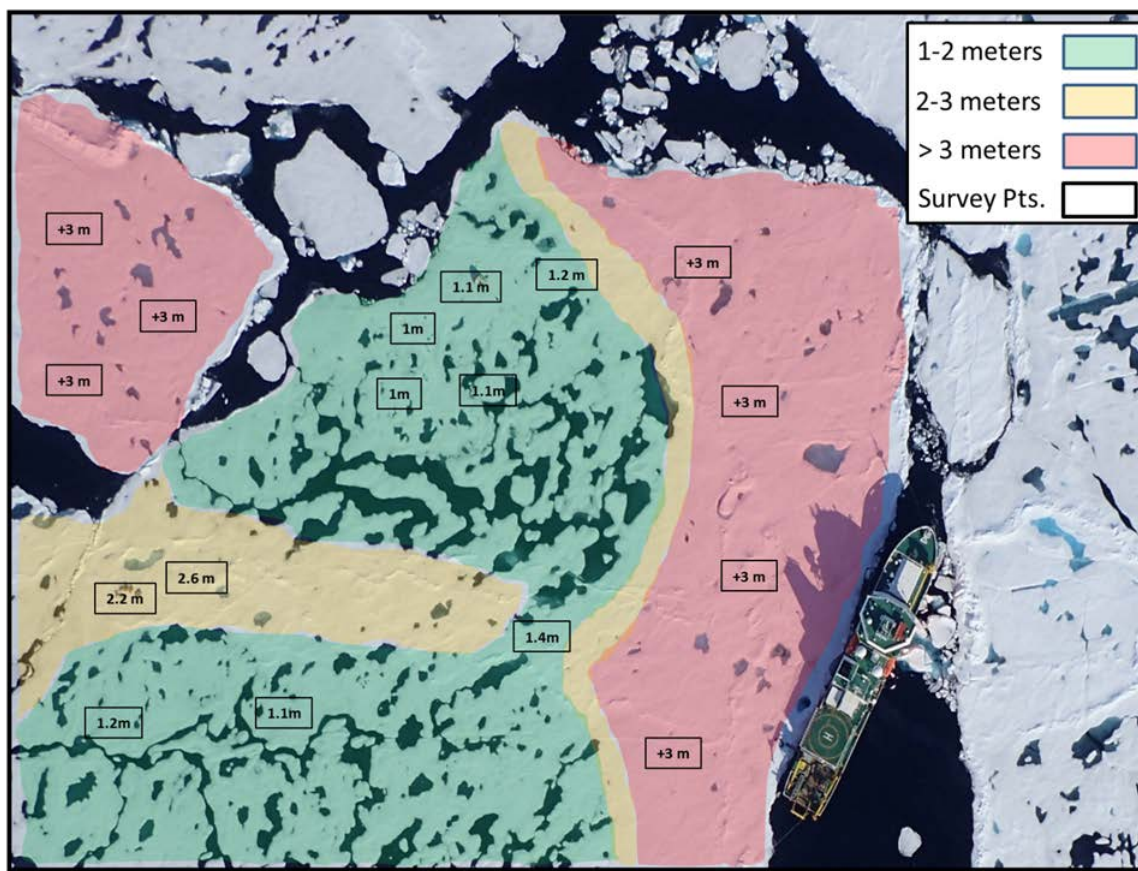
A rough contour map of sea ice depth at the MIZ-KOPRI Ice Camp derived from ice surveys conducted between 9 and 14 August.

Figure 3.5.   Sea Ice Thickness Survey at MIZ C5

Masked high-resolution (1-m) visible satellite image showing open water (A_{OWF}, false color black), melt ponds (A_{MP}, false color light blue), and bare sea ice (white). The areal coverage of open water, melt ponds, and sea ice were used to estimate the fraction of solar radiative fluxes penetrating the sea ice (f_{sw}) for use in the LTC model. Location of MIZ cluster 5 is indicated by the green dot.

Figure 3.6.   Masked High-Resolution Visible Satellite Image of MIZ C5
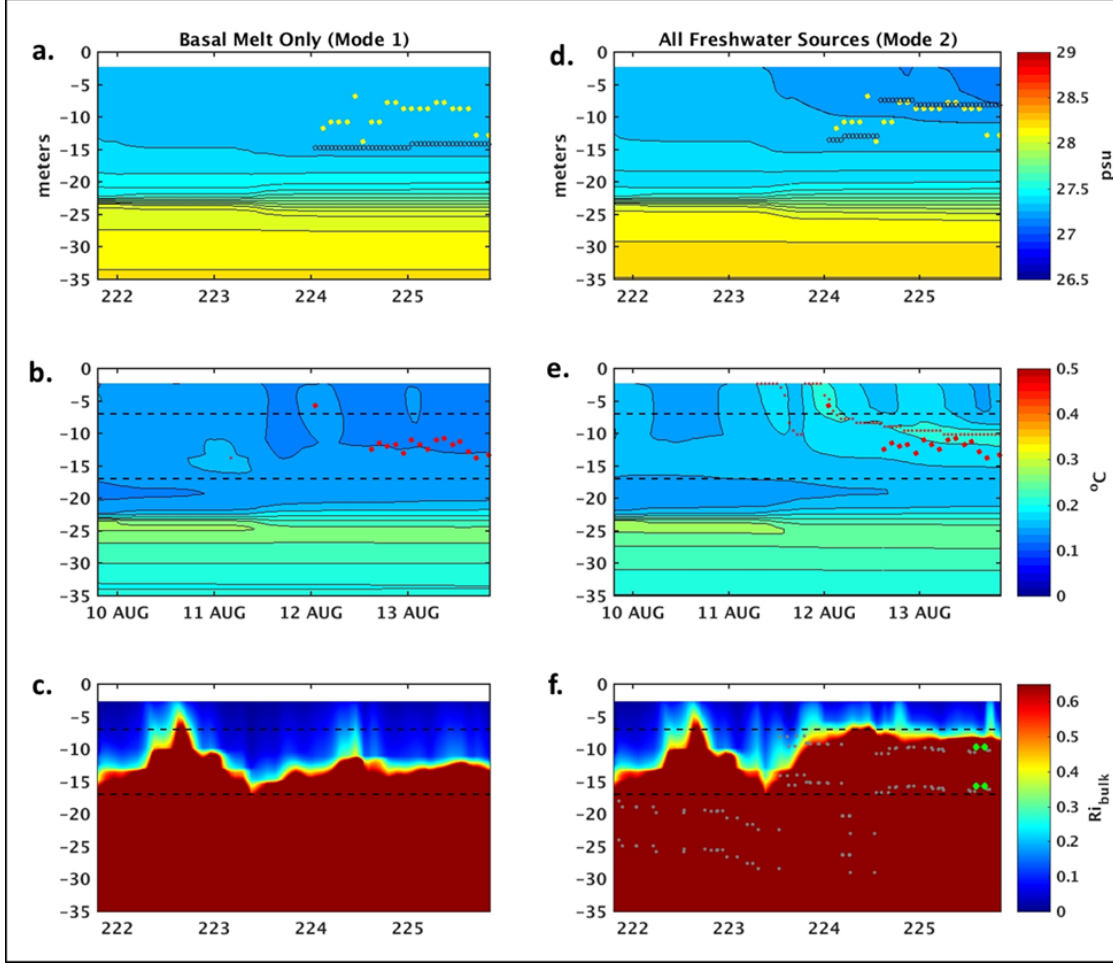
LTC model results of the late summer halocline and NSTM for (a-c) basal melt only ($w_p = 0$) and (c-e) for all freshwater inputs (basal melt + w_p) as observed at the MIZ-KOPRI Ice Camp. Panels (a) and (d) are salinity with modeled (black circles) and observed (yellow dots) near-surface N^2 maximums. Panels (b) and (e) are temperature above freezing with modeled (small red dots) and observed (large red dots) NSTM overlaid. Panels (c) and (f) are the bulk Richardson number (Ri_{bulk}) estimates of the upper ocean using Eqn. (3.7). The NSTM layer is indicated by horizontal black lines. Gray dots on Fig. 3.7f are the deployment depths of the NPS Turbulence Frame during the C5 Ice Camp with the green highlighted period indicating the YD 225.65 case study.

Figure 3.7.   LTC Model Simulations of the Late Summer Halocline and NSTM
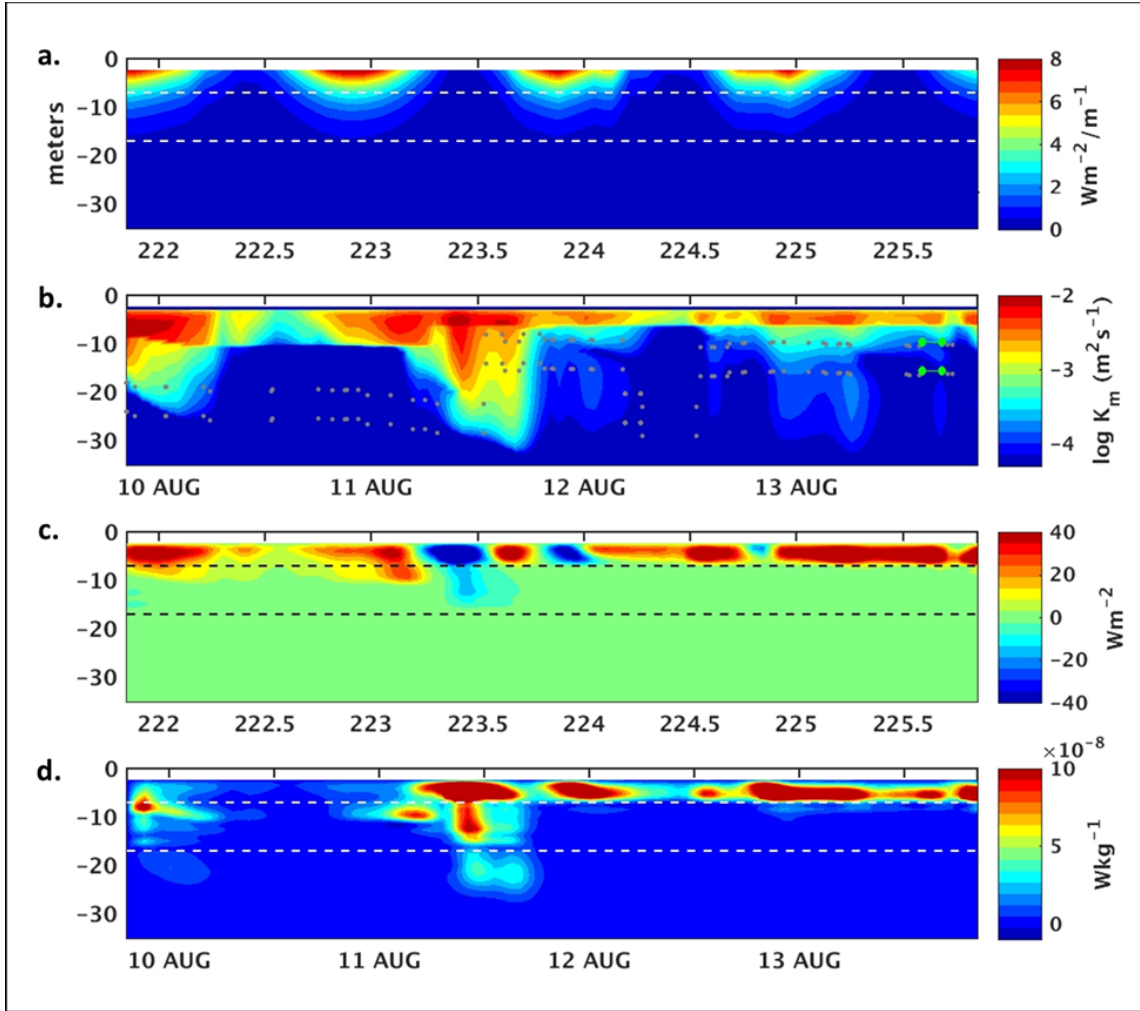
LTC model output from the MIZ-KOPRI Ice Camp showing the (a) upper ocean absorbed solar radiative flux, (b) eddy viscosity (K_m), (c) dynamic heat flux, and (d) buoyancy flux. The horizontal white and black dashed lines on each panel denote the NSTM layer. Gray dots on Fig. 3.8b indicate the deployment depths of the NPS Turbulence Frame with the green highlighted period indicating the YD 225.65 case study.

Figure 3.8.   LTC Model Radiative and Turbulent Fluxes
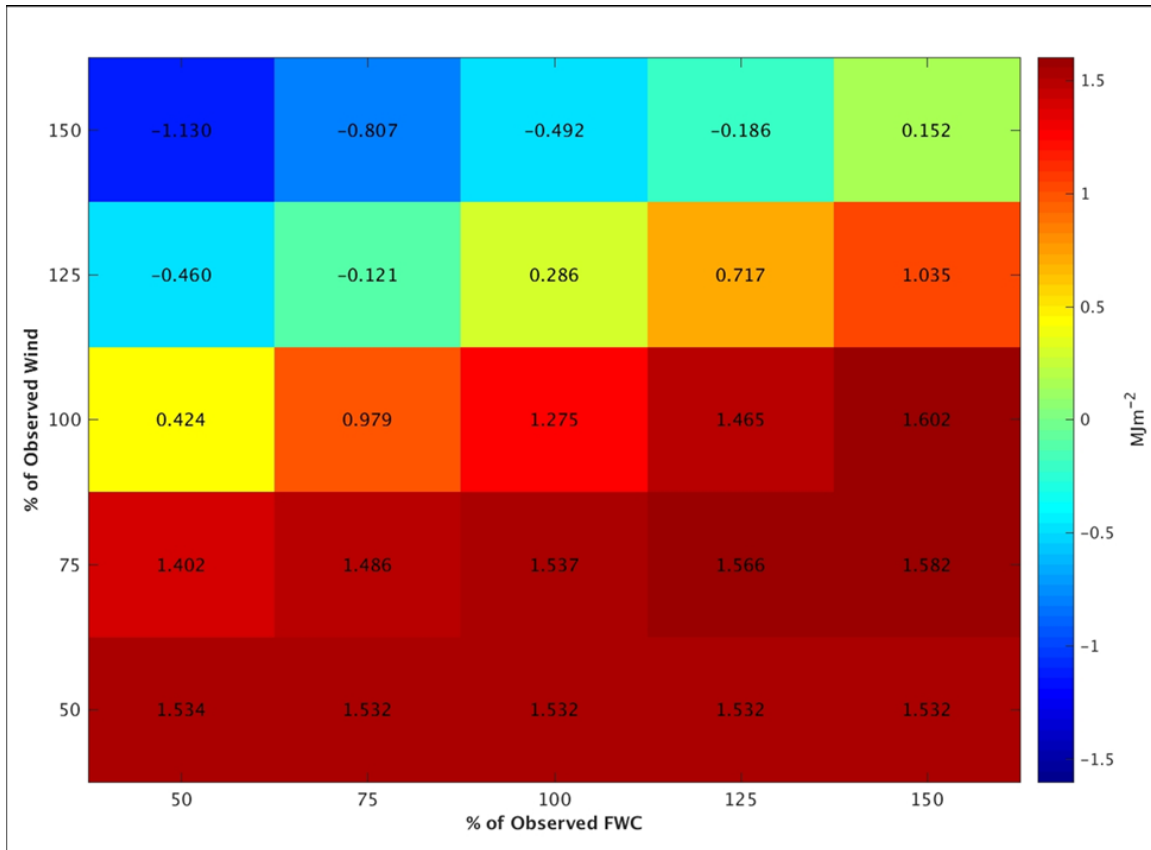(Late Summer Case)
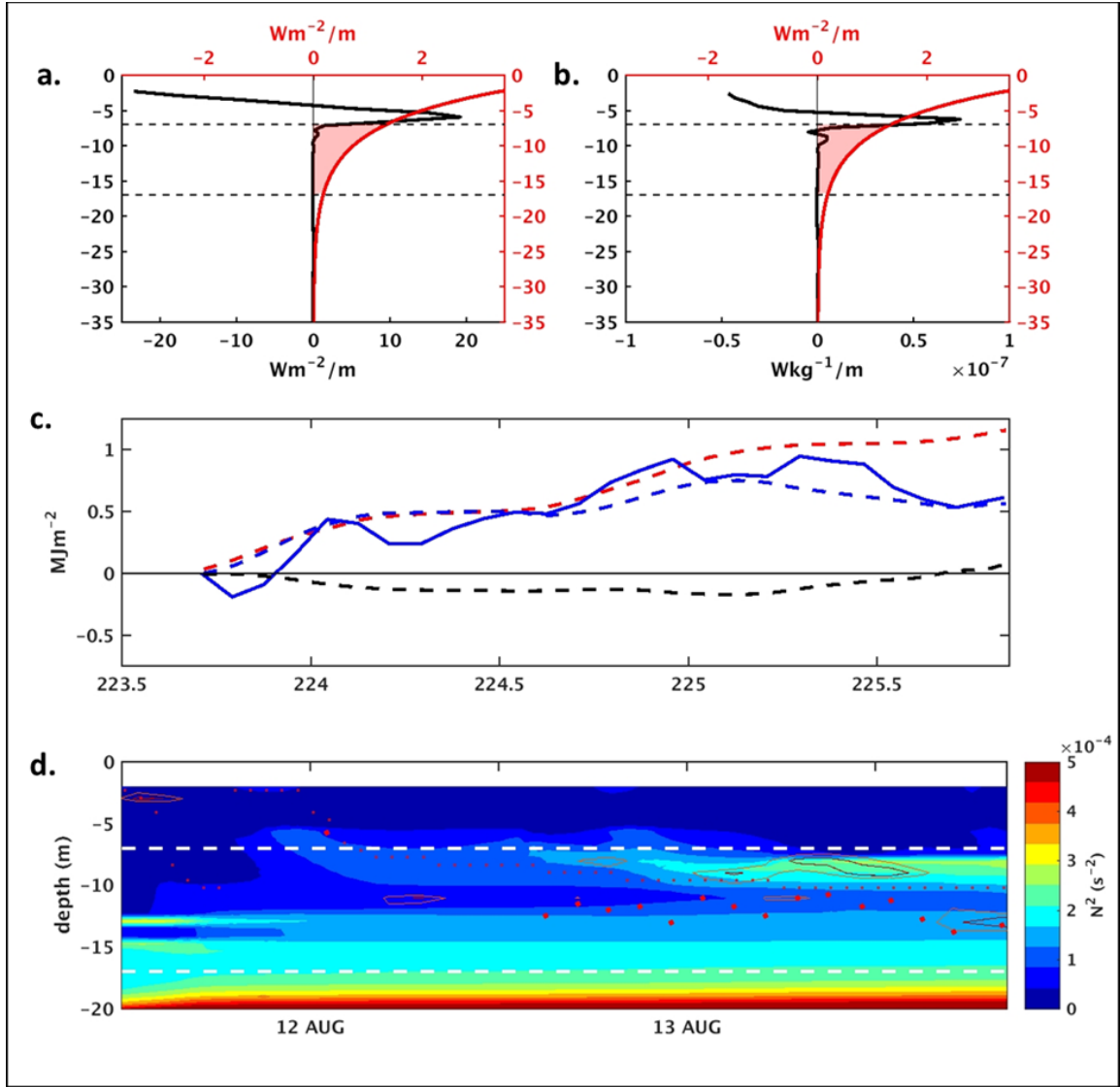
LTC model output of the (a) dynamic heat flux convergence (black), (b) buoyancy flux convergence (black), and (b-c) radiative flux convergence (red) averaged between YDs 223.7 to 225.8. Red shaded areas show absorbed radiative flux overlapping the NSTM layer. (c) Model output displaying the cumulative NSTM layer heat storage (blue dashed), integrated absorbed radiative fluxes (red dashed), and integrated dynamic heat fluxes (black dashed) with the observed NSTM layer cumulative heat storage (blue). (d) Plot of the LTC model N^2 (colorfill) and observed N^2 (contours >4 x 10^{-4} s^{-2}) showing the relative depths of the summer halocline to the modeled (small red dots) and observed (large red dots).

Figure 3.9.   Late Summer Halocline Stratification and NSTM Heat Flux Convergence

99
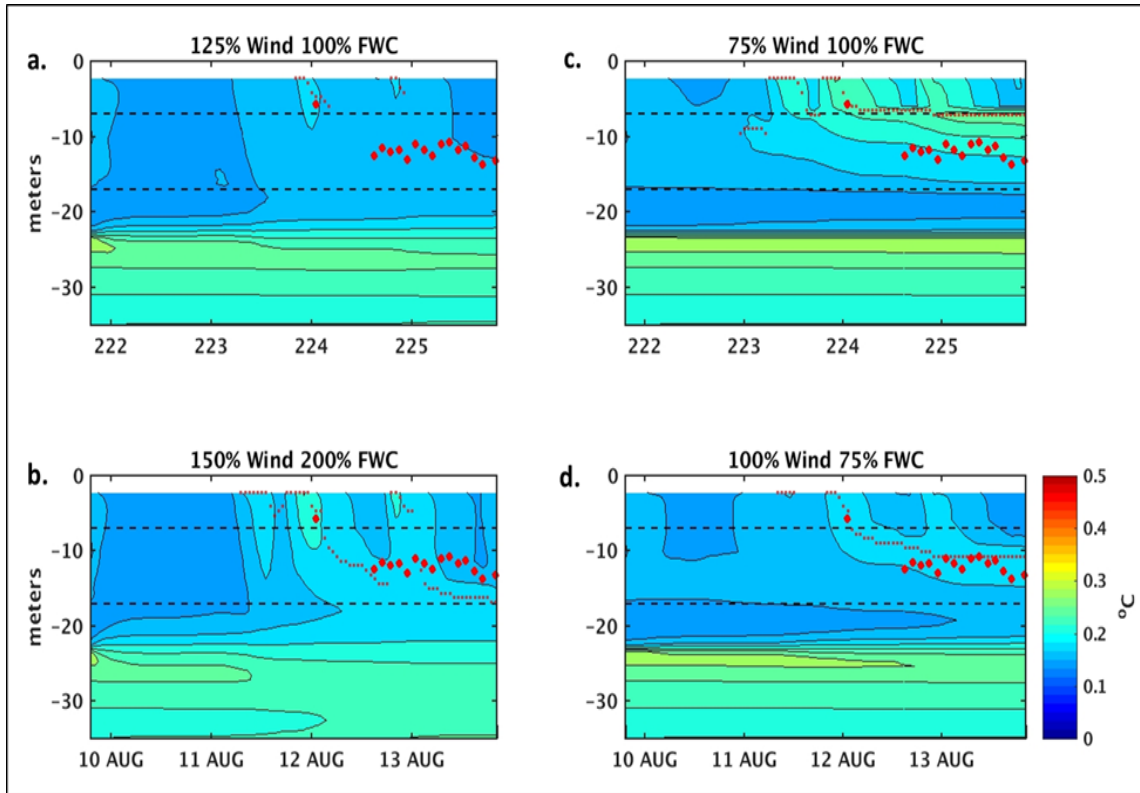
(a-d) LTC model output of the temperature above freezing for the wind and buoyancy sensitivity test cases. Modeled (small red dots) and observed (large red dots) NSTM depths are annotated on each plot. Test case modifications to observed winds and freshwater input (*FWC*) are indicated above each plot.

Figure 3.10.   LTC Model Wind-Buoyancy Sensitivity Tests for the Late Summer NSTM

LTC model results of the 25 different wind and buoyancy test scenarios conducted on the late summer NSTM. Numbers in the matrix indicate the cumulative heat storage gain/loss in the NSTM layer (7-17 m) across the time series (YDs 221.8-225.8).

Figure 3.11.   Heat Storage Matrix of Wind-Buoyancy Sensitivity Testing
(Late Summer NSTM)
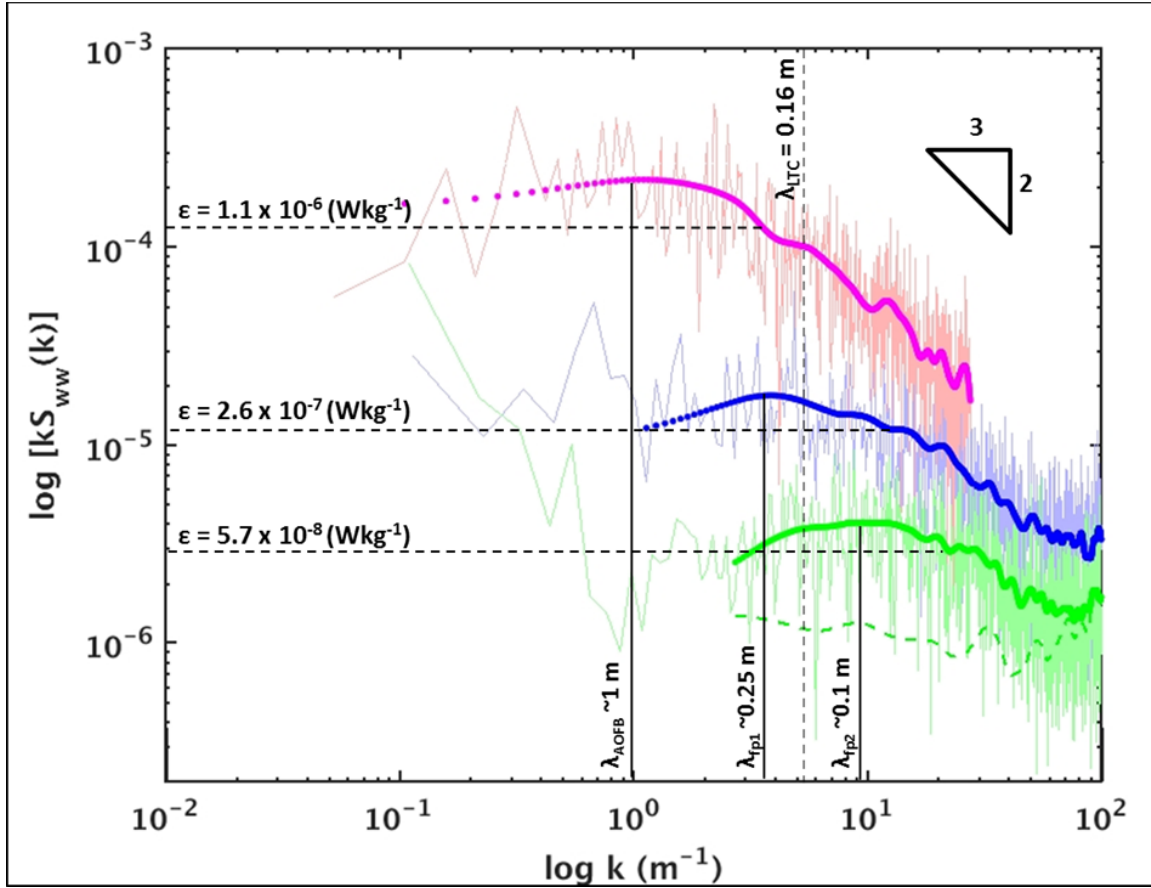
Wave number scaled vertical velocity power spectra for the high wind case at AOFB 29 (magenta), upper Flux Frame package at 9 m depth (blue), and lower Flux Frame package at 15 m depth (green). In this k-scaled spectrum, the k multiplier changes the -5/3 power law expected of the inertial subrange (Kolmogorov 1941) to -2/3. Convolution filter results (solid lines) highlight the turbulent energy peaks for each spectrum and the corresponding wavenumbers (k_{max}, black vertical lines) by which estimates of mixing length (λ) were estimated using Eqn. (3.15). Corresponding LTC model λ is indicated by the vertical dashed line. Estimates of turbulent kinetic energy (TKE) dissipation (ε) were made for each spectrum using the inertial-dissipation method (Eqn. (3.16)) to characterize turbulent eddy intensity in the NSTM layer. The green dashed line represents the spectral results from the lower Flux Frame package for the periods adjacent to the YD 225.65 event.

Figure 3.12.   Spectral Estimates of Turbulent Mixing Length inside the
Late Summer NSTM
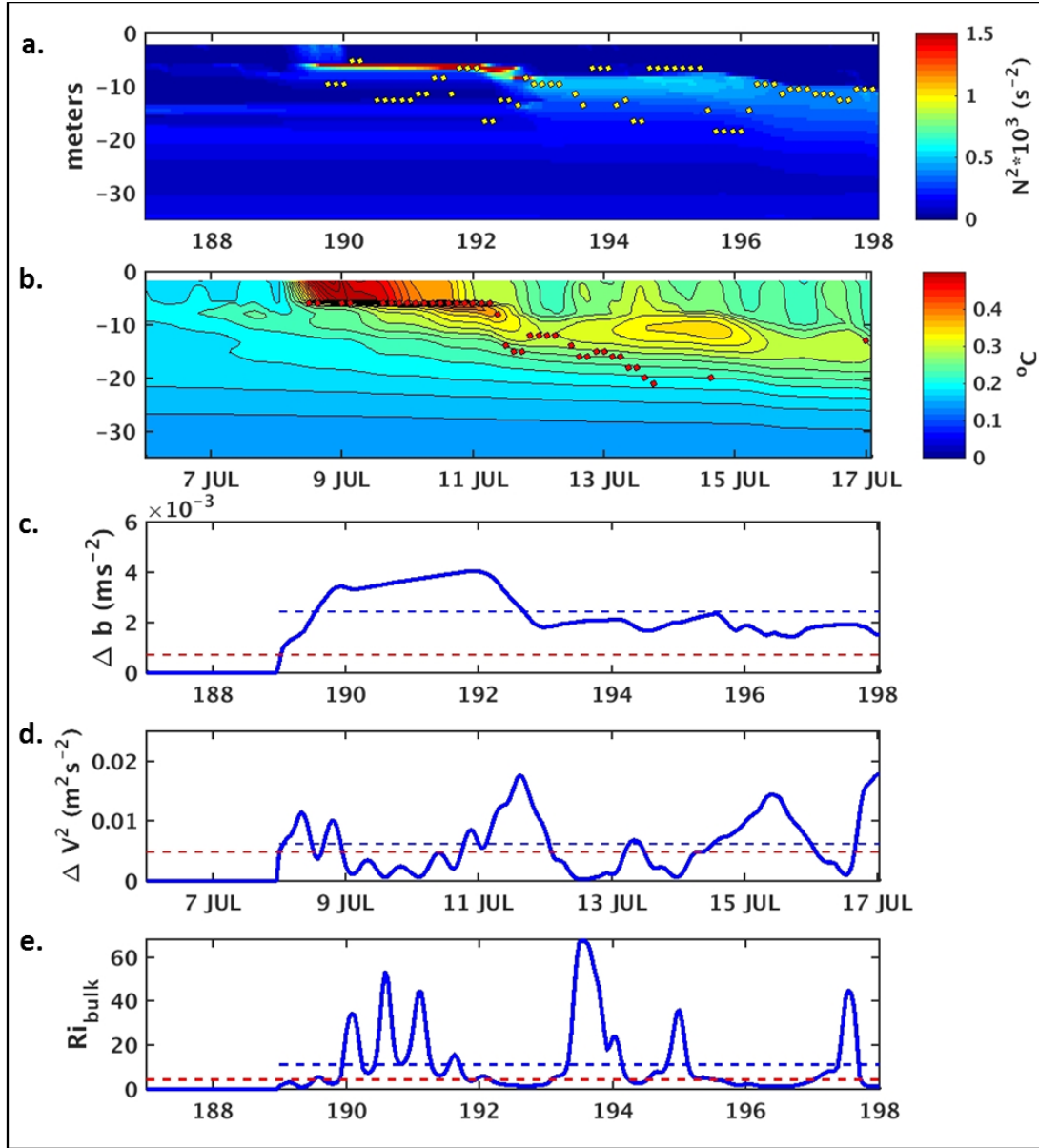
LTC model results of the early summer case using the air-ice-ocean conditions at MIZ C2. Plotted are the (a) modeled N^2 with observed summer halocline depths (yellow dots) and (b) modeled temperature above freezing with observed NSTM depths (red dots, Jackson et al. (2010) criteria). In this case, 0.25 m of freshwater was added to the model on YD 189 to simulate the observed melt pond drainage. (c) Corresponding model buoyancy (Δb) and (d) shear (ΔV^2) components of the (e) bulk Richardson number (Ri_{bulk}) are presented along with mean values (blue dashed) for each. For comparison, the mean values of the Ri_{bulk} parameters from the late summer case at MIZ C5 are also provided (red dashed). Evaluation of the Ri_{bulk} and its components begin after the melt pond drainage event.

Figure 3.13.   LTC Model Simulations of the Early Summer Halocline and NSTM (MIZ C2 Case/Conditions)
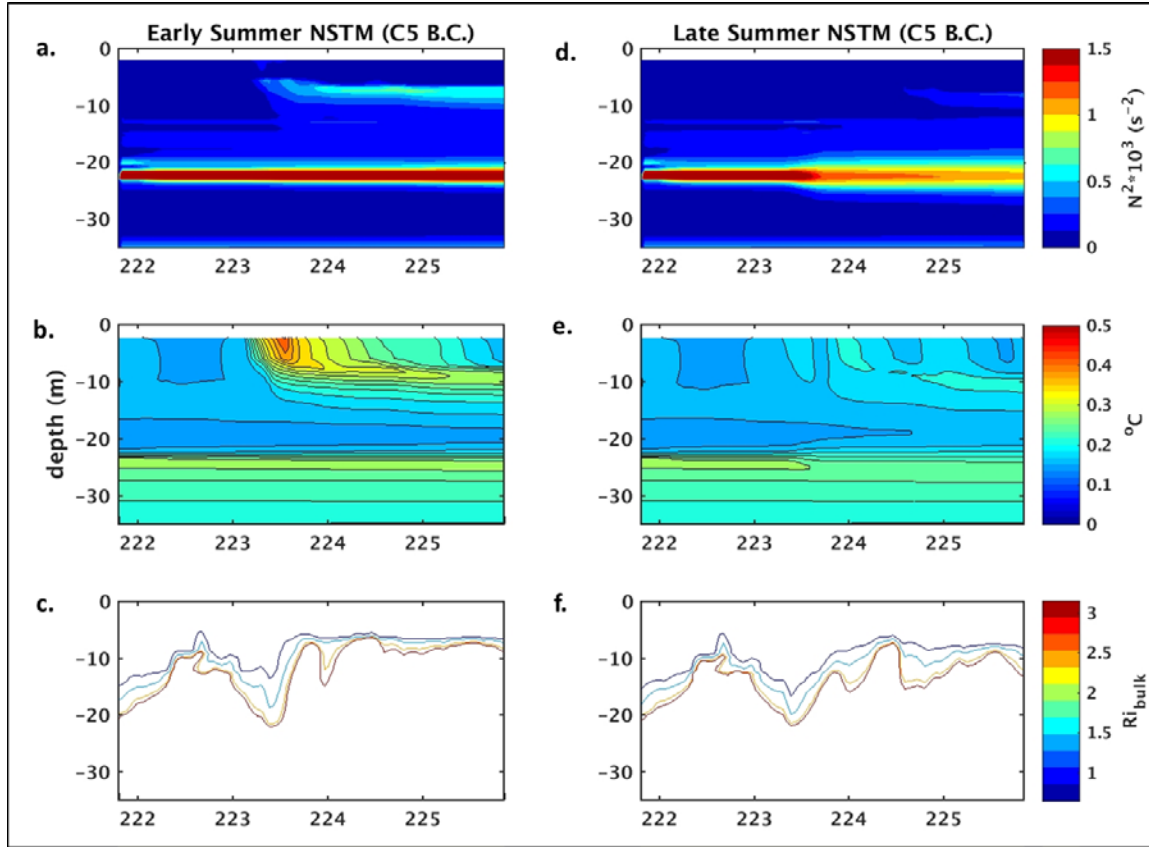
LTC model output of the (a) N^2 and (b) temperature above freezing, and (c) contours of Ri_{bulk} (0.65, 1.3, 1.95, 2.6) for the early summer case using MIZ C5 air-ice-ocean conditions. For this case, 0.25 m of freshwater was added to the model on YD 223. (d-f) Same format as the left-hand panels but for the late summer case using observed freshwater input (0.1 m) during the MIZ-KOPRI Ice Camp.

Figure 3.14. LTC Model Simulations of the Early and Late Summer Halocline and NSTM (MIZ C5 Case/Conditions)
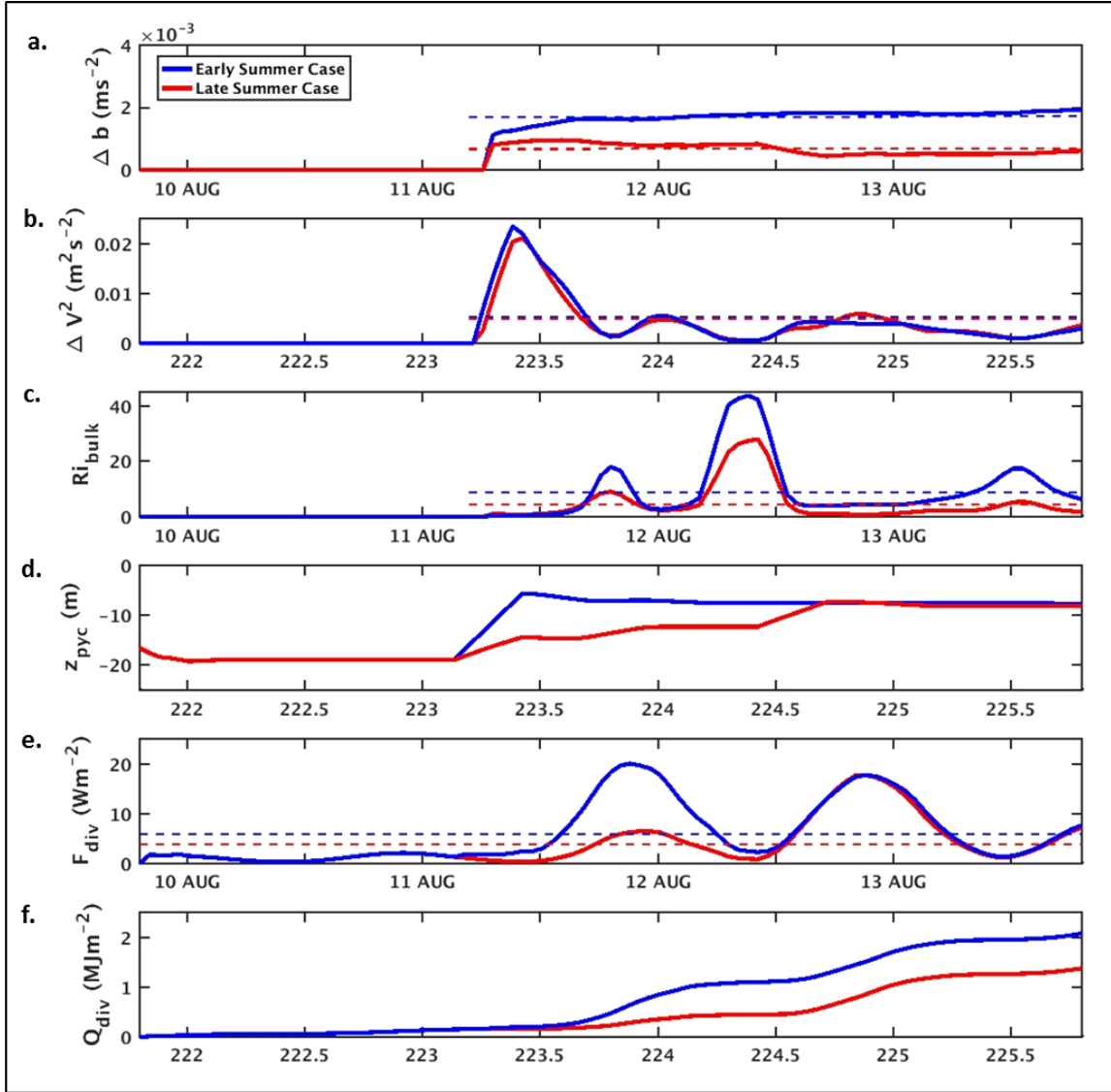
Plotted are the early (blue) and late (red) summer (a) buoyancy (Δb) and (b) shear (ΔV^2) components of the (c) bulk Richardson number (Ri_{bulk}) from the LTC model results presented on Fig. 3.14. Evaluation of the Ri_{bulk} and its components begin after the first buoyancy event on YD 223.1. Below these panels are the corresponding values of the (d) summer halocline depth (z_{pyc}), (e) the depth integrated absorbed solar flux below the summer halocline, and (f) the cumulative solar heat input below the summer halocline (Q_{div}).

Figure 3.15.   Model Comparisons of the Early and Late Summer Halocline
Bulk Richardson Number and NSTM Heating (MIZ C5
Case/Conditions)

105
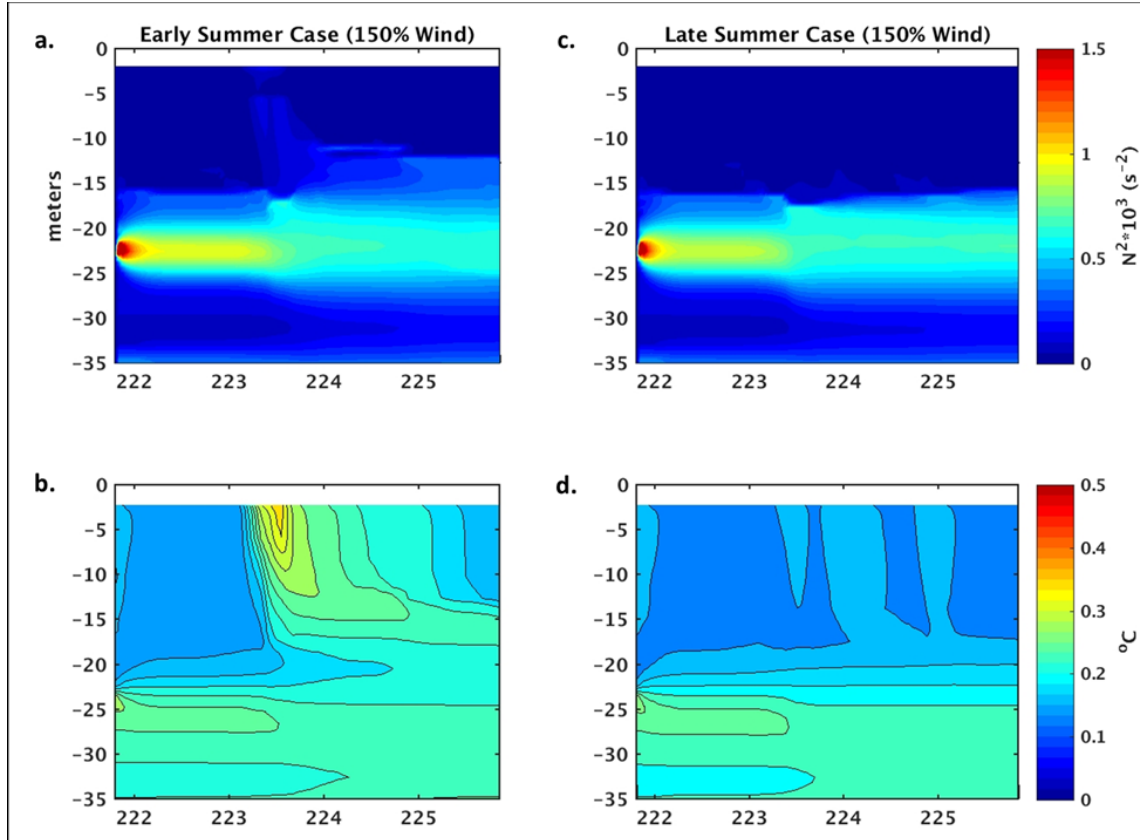
LTC model results of (a, c) N^2 and (b, d) δT for the high wind test (50% increase) conducted on the early (a-b) and late (c-d) summer NSTM using the air-ice-ocean conditions from MIZ C5.

Figure 3.16.   LTC Model High Wind Tests of the Early and Late Summer
Halocline and NSTM (MIZ C5 Case/Conditions)

LIST OF REFERENCES

Cole, S. T., M.-L. Timmermans, J. M. Toole, R. A. Krishfield, and F. T. Thwaites, 2014: Ekman veering , internal waves, and turbulence observed under Arctic sea ice. *J. Phys. Oceanogr.*, **44**(5), 1306–1328, doi.org/10.1175/JPO-D-12-0191.1.

Cole, S. T., F. T. Thwaites, R. A. Krishfield, and J. M. Toole, 2015: Processing of velocity observations from Ice-Tethered Profilers. *Proc. IEEE Conf. on Oceans 2015*, Washington, DC, Marine Technology Society, 1–10.

Comiso, J. C., C. L. Parkinson, R. Gersten, and L. Stock, 2008: Accelerated decline in the Artic sea ice cover. *Geophys. Res. Lett*, **35**, L01703, doi:10.1029/2007GL031972.

Comiso, J. C., 2012: Large decadal decline of the arctic multiyear ice cover. J. *Clim*, **25**(4), 1176–1193, doi:10.1175/JCLI-D-11-00113.1.

Eicken, H., H. R. Krouse, D. Kadko, and D. K. Perovich, 2002: Tracer studies of pathways and rates of meltwater transport through Arctic summer sea ice. *J. Geophys. Res.*, **107**(C10), 8046, doi:10.1029/2000JC000583.

Frey, K. E., D. K. Perovich, and B. Light, 2011: The spatial distribution of solar radiation under a melting Arctic sea ice cover. *Geophys. Res. Lett* , **38**, L22501, doi:10.1029/2011GL049421.

Gallaher, S.G., T. P. Stanton, W. J. Shawn, S. T. Cole, J. M. Toole, J. P. Wilkinson, T. Maksym, and B. Hwang, 2016: Evolution of a Canada Basin ice-ocean boundary layer and mixed layer across a developing thermodynamically forced marginal ice zone. *J. Geophys. Res.*, **121**, doi:10.1002/2016JC011778.

Hayes, D. R., and J. Morison, 2008: Ice-ocean turbulent exchange in the Arctic summer measured by an autonomous underwater vehicle. *Limnol. Oceanogr.*, **53**(5_part_2), 2287–2308, doi:10.4319/lo.2008.53.5_part_2.2287.

Hinze, J. O., 1975: *Turbulence*. McGraw-Hill, New York, 790 pp.

Hsu, S. A., E. A. Meindl, and D. D. Gilhousen, 1994: Determining the power-law wind profile exponent under near-neutral stability conditions at sea. *J. Appl. Meteorol.*, **33**, 757–765, doi:10.1175/1520-0450(1994)033<0757:DTPLWP>2.0.CO;2.

Hunke, E. C., D. A. Hebert, and O. Lecomte, 2013: Level-ice melt ponds in the Los Alamos sea ice model, CICE. *Ocn. Mod.*, **71**, 26–42, doi:10.1016/j.ocemod.2012.11.008.

Jackson, J. M., E. C. Carmack, F. A. McLaughlin, S. E. Allen, and R. G. Ingram, 2010: Identification, characterization, and change of the near-surface temperature maximum in the Canada Basin 1993–2008. *J. Geophys. Res.*, **115**, C05021, doi:10.1029/2009JC005265.

Jackson, J. M., S. E. Allen, F. A. McLaughlin, R. A. Woodgate, and E. C. Carmack, 2011: Changes to the near-surface waters in the Canada Basin, Arctic Ocean from 1993–2009. *J. Geophys. Res.*, **116**, C10008, doi:10.1029/2011JC007069.

Jackson, J. M., W. J. Williams, and E. C. Carmack, 2012: Winter sea-ice melt in the Canada Basin, Arctic Ocean. *Geophys. Res. Lett.,* **39**, L03603, doi:10.1029/2011GL050219.

Jackson, K., J. Wilkinson, T. Maksym, D. Meldrum, J. Beckers, C. Haas, and D. Mackenzie, 2013: A novel and low-cost sea ice mass balance buoy. *J. Atmos. Oceanic. Technol.*, **30**(11), 2676–2688, doi:10.1175/JTECH-D-13-00058.1.

Kim, T. S., K. A. Park, M. S. Lee, J. J. Park, S. Hong, K. L. Kim, and E. Chang, 2013: Application of bimodal histogram method to oil spill detection from a satellite synthetic aperture radar image. *Korean J. Remote Sens.*, **29**(6), 645–655, doi:10.7780/kjrs.2013.29.6.7.

Kolmogorov, A. N., 1941: Dissipation of energy in a locally isotropic turbulence. *Dokl. Akad. Nauk. SSSR* **32**: 141. (English translation in *Proc. R. Soc. London A* **434**: 15, 1991).

Krishfield, R., J. Toole, A. Proshutinsky, and M-L. Timmermans, 2008: Automated ice-tethered profilers for seawater observations under pack ice in all seasons. *J. Atmos.Oceanic. Technol.*, **25**(11), 2091–2105, doi:10.1175/2008JTECHO587.1.

Lane, L. S., 1997: Canada Basin, Arctic Ocean: Evidence against a rotational origin. *Tectonics*, **16**(3), 363–387, doi:10.1029/97TC00342.

Large, W. G., J. C. McWilliams, and S. C. Doney, 1994: Oceanic vertical mixing: A review and a model with a nonlocal boundary layer parameterization. *Rev. Geophys.*, **32**(4), 363–403, doi:10.1029/94RG01872.

Lee, C. M., and Coauthors, 2012: Marginal Ice Zone (MIZ) Program: Science and experiment plan. *Technical Report APL-UW 1201*, Applied Physics Laboratory, 48pp, University of Washington, Seattle, WA.

Light, B. T., T. C. Grenfell, and D. K. Perovich, 2008: Transimission and absorption of solar radiation by Arctic sea ice during the melt season. *J. Geophys. Res.*, **113**, C03023, doi:10.1029/2006JC003977.

Macdonald, R. W., E. C. Carmack, F. A. McLaughlin, K. K. Falkner, and J. H. Swift, 1999: Connections among ice, runoff and atmospheric forcing in the Beaufort Gyre. *Geophys. Res. Lett.*, **26**(15), 2223–2226, doi:10.1029/1999GL900508.

Maykut, G. A., 1985: An introduction to ice in polar oceans. Technical *Report APL-UW 8510*, Applied Physics Laboratory, 116pp, University of Washington, Seattle, WA.

Maykut, G. A., and M. G. McPhee, 1995: Solar heating of the Arctic mixed layer. *J. Geophys. Res.*, **100**, C12, doi:10.1029/95JC02554.

McPhee, M. G., 1987: A time-dependent model for turbulent transfer in a stratified oceanic boundary layer. *J. Geophys. Res.*, **92**(C7), 6977–7986, doi:10.1029/JC092iC07p06977.

McPhee, M. G., 1992: Turbulent heat flux in the upper ocean under sea ice. *J. Geophys. Res.*, **97**(C4), 5365, doi:10.1029/92JC00239.

McPhee, M. G., 1994: On the turbulent mixing length in the Oceanic Boundary Layer. *J. Phys. Oceanogr.*, **24**(9), 2014–2031, doi:/10.1175/1520-0485(1994)024<2014: OTTMLI>2.0.CO;2.

McPhee, M. G., 1998: Freshening of the upper ocean in the Arctic: Is perennial sea ice disappearing. *Geophys. Res. Lett.*, **25**(10), 1729–1732, doi:10.1029/98GL00933.

McPhee, M. G., 1999: Scales of turbulence and parameterization of mixing in the ocean boundary layer. *J. Mar. Sys.*, **21**, 55–65, doi:10.1016/S0924-7963(99)00005-6.

McPhee, M. G., 2002: Turbulent stress at the ice/ocean interface and bottom surface hydraulic roughness during the SHEBA drift. *J. Geophys. Res.*, **107**(C10), 8037, doi:10.1029/2000JC000633.

McPhee, M. G., 2008: *Air-Ice-Ocean Interaction: Turbulent Ocean Boundary Layer Exchange Processes*. Springer, New York, 215 pp.

McPhee, M. G., G. A. Maykut, and J. H. Morison, 1987: Dynamics and thermodynamics of the ice/upper ocean system in the marginal ice zone of the Greenland Sea. *J. Geophys. Res.*, **92**(C7), 7017, doi:10.1029/JC092iC07p07017.

McPhee, M. G., and D. G. Martinson, 1994: Turbulent mixing under drifting pack ice in the Weddell Sea. *Science*, **263**, 5144, doi:10.1126/science.263.5144.218.

McPhee, M. G., A. Proshutinsky, J. H. Morison, M. Steele, and M. B. Alkire, 2009: Rapid change in freshwater content of the Arctic Ocean. *Geophys. Res. Lett.*, **36**, L10602, doi:10.1029/2009GL037525.

MIZEX Group, 1986: MIZEX East 83/84: The summer marginal ice zone program in the Fram Strait/Greenland Sea. *Eos Trans. AGU*, **67***(23)*, 513–517, doi:10.1029/EO067i023p00513.

Morison, J. H., M. G. McPhee, and G. A. Maykut, 1987: Boundary layer, upper ocean, and ice observations in the Greenland Sea marginal ice zone. *J. Geophys. Res.*, *92*(C7), 6987–7011, doi:10.1029/JC092iC07p06987.

Nghiem, S. V., D. K. Hall, I. G. Rigor, P. Li, and G. Neumann, 2014: Effects of Mackenzie River discharge and bathymetry on sea ice in the Beaufort Sea. *Geophys. Res. Lett.,* **41**, 873–879, doi:10.1002/2013GL058956.

Paulson, C.A. and W. S. Pegau, 2001: The summertime thermohaline evolution of an Arctic lead: Heat budget of the surface layer. *Sixth Conf. on Polar Meteorology and Oceanography*, San Diego, CA, Amer. Meteor. Soc., 271–274.

Pegau, W., S. and C. A. Paulson, 2001: The albedo of Arctic leads in summer. *Ann. Glaciol*, **33**, 221–224. doi:10.3189/172756401781818833.

Perovich, D. K., and C. Polashenski, 2012: Albedo evolution of seasonal Arctic sea ice. *Geophys. Res. Lett.*, **39**, L08501, doi:10.1029/2012GL051432.

Perovich, D. K., T. C. Grenfell, B. Light, and P. V. Hobbs, 2002: Seasonal evolution of the albedo of multiyear Arctic sea ice. *J. Geophys. Res.*, **107**(C10), 8044, doi:10.1029/2000JC000438.

Perovich, D. K., B. Light, H. Eicken, K. F. Jones, K. Runciman, and S. V. Nghiem, 2007a: Increasing solar heating of the Arctic Ocean and adjacent seas, 1979–2005: Attribution and role in the ice-albedo feedback. *Geophys. Res. Lett.*, **34**, L19505, doi:10.1029/2007GL031480.

Perovich, D. K., S. V. Nghiem, T. Markus, and A. Schweiger, 2007b: Seasonal evolution and interannual variability of the local solar energy absorbed by the Arctic sea ice-ocean system. *J. Geophys. Res.*, **112**, C03005, doi:10.1029/2006JC003558.

Perovich, D. K., W. Meier, J. Maslanik, and J. Richter-Menge, 2012: Sea ice cover [in State of the Climate in 2011]. *Bull. Am. Meteorol. Soc.,* **3**(7), S140-S142.

Persson, P. O. G., C. W. Fairall, E. L. Andreas, P. S. Guest, and D.K. Perovich, 2002: Measurements near the Atmospheric Surface Flux Group tower at SHEBA: Near-surface conditions and surface energy budget. *J. Geophys. Res.*, **107**(C10), 8045, doi:10.1029/2000JC000705.

Polashenski, C., D. Perovich, J. Richter-Menge and B. Elder, 2011: Seasonal ice mass-balance buoys: Adapting tools to the changing Arctic. *Ann. Glaciol*, **52**(57), 18–26. doi:10.3189/172756411795931516.

Polashenski, C., D. Perovich and Z. Courville, 2012: The mechanisms of sea ice melt pond formation and evolution. *J. Geophys. Res.*, **117**, C01001, doi:10.1029/2011JC007231.

Price, J. F., R. A. Weller, and R. Pinkel, 1986: Diurnal cycling: Observations and models of the upper ocean response to diurnal heating, cooling, and wind mixing. *J. Geophys. Res.,* **91***(*C7*),* 8411–8427, doi:10.1029/JC091iC07p08411.

Proshutinsky, A., R. Krishfield, M.-L. Timmermans, J. Toole, E. Carmack, F. McLaughlin, W. J. Williams, S. Zimmermann, M. Itoh, and K. Shimada, 2009: Beaufort Gyre freshwater reservoir: State and variability from observations. *J. Geophys. Res.*, **114**, C00A10, doi:10.1029/2008JC005104.

Saha, S., and Coauthors, 2010: The NCEP Climate Forecast System Reanalysis. *Bull. Am. Meteorol. Soc.*, **91**, 1015–1057, doi:10.1175/2010BAMS3001.1.

Salah, M. B., 2011: Multiregion image segmentation by parametric kernel graph cuts. *IEEE Trans. Image Process.*, **20**(2), 545–557, doi:10.1109/TIP.2010.2066982.

Shaw, W. J. and J. H. Trowbridge, 2001: The direct estimation of near-bottom turbulent fluxes in the presence of energetic wave motions. *J. Atmos. Oceanic Technol.*, **18**, 1540–1557, doi:10.1175/1520-0426(2001)018<1540:TDEONB>2.0.CO;2.

Shaw, W. J., T. P. Stanton, M. G. McPhee, and T. Kikuchi, 2008: Estimates of surface roughness length in heterogeneous under-ice boundary layers. *J. Geophys. Res.*, **113**, C08030, doi:10.1029/2007JC004550.

Shaw, W. J., T. P. Stanton, M. G. McPhee, J. H. Morison, and D. G. Martinson, 2009: Role of the upper ocean in the energy budget of Arctic sea ice during SHEBA. *J. Geophys. Res.*, **114**, C06012, doi:10.1029/2008JC004991.

Skyllingstad, E. D., and C. A. Paulson, 2005: Simulation of turbulent exchange processes in summertime leads. *J. Geophys. Res.*, **110**, C05021, doi:10.1029/2004JC002502.

Stanton, T. P., W. J. Shaw, and J. K. Hutchings, 2012: Observational study of relationships between incoming radiation, open water fraction, and ocean-to-ice heat flux in the Transpolar Drift: 2002–2010. *J. Geophys. Res.*, **117**, C07005, doi:10.1029/2011JC007871.

Steele, M., W. Ermold, and J. Zhang, 2008: Arctic Ocean surface warming trends over the past 100 years. *J. Geophys. Res. Lett.*, **35**, doi:10.1029/2007GL031651.

Steele, M., J. Zhang, and W. Ermold, 2010: Mechanisms of summertime upper Arctic Ocean warming and the effect on sea ice melt. *J. Geophys. Res.*, **115**, C11004, doi:10.1029/2009JC005849.

Steele, M., W. Ermold, and J. Zhang, 2011: Modeling the formation and fate of the near-surface temperature maximum in the Canada Basin of the Arctic Ocean. *J. Geophys. Res.*, **116**, C11015, doi:10.1029/2009JC006803.

Stegall, S. T. and J. Zhang, 2012: Wind field climatology, changes, and extremes in the Chukchi-Beaufort Seas and Alaska North Slope during 1979–2009. *J. Clim.*, **25**, 8075–8089, doi:10.1175/JCLI-D-11-00532.1.

Taylor, G. I., 1938: The Spectrum of Turbulence. *Proc. R. Soc. London A* **164**: 476.

Thomson, J. and E. Rogers, 2014: Swell and sea in the emerging Arctic Ocean. *Geophys. Res. Lett.*, **41**, 3136–3140, doi:10.1002/2014GL059983.

Timmermans, M. -L., 2015: The impact of stored solar heat on Arctic sea ice growth. *Geophys. Res. Lett.*, **42**, 6399–6406 doi:10.1002/2015GL064541.

Timmermans, M. -L., and Coauthors, 2014: Mechanisms of Pacific Summer Water variability in the Arctic's Central Canada Basin. *J. Geophys. Res.Oceans*, **119**, 7523–7548, doi:10.1002/2014JC010273.

Tivy, A., S. E. L. Howell, B. Alt, S. McCourt, R. Chagnon, G. Crocker, T. Carrieres, and J. J. Yackel, 2011: Trends and variability in summer sea ice cover in the Canadian Arctic based on the Canadian Ice Service Digital Archive, 1960–2008 and 1968–2008. *J. Geophys. Res.*, **116**, C03007, doi:10.1029/2009JC005855.

Tomasi, C. and R. Manduchi, 1998: Bilateral filtering for gray and color images. *Proceedings of the 1998 IEEE International Conference on Computer Vision,*839-846, Bombay, India, doi: 10.1109/ICCV.1998.710815.

Toole, J. M., M.-L. Timmermans, D. K. Perovich, R. A. Krishfield, A. Proshutinsky, J. A. Richter-Menge, 2010: Influences of the ocean surface mixed layer and thermohaline stratification on Arctic Sea ice in the central Canada Basin. *J. Geophys. Res.*, **115**, C10018, doi:10.1029/2009JC005660.

Toole, J. M., R. A. Krishfield, M.-L. Timmermans, and A. Proshutinsky, 2011: The Ice-Tethered Profiler: ARGO of the Arctic. *Oceanography*, **24**(3), 162–173, doi:10.5670/oceanog.2011.65.

U.S. Navy, 2014: *Arctic Roadmap*, U.S. Navy Task Force Climate Change, Oceanographer of the Navy, Washington, D. C., 30 pp.

UNESCO, 1983: Algorithms for computation of fundamental properties of seawater. *UNESCO Technical Papers in Marine Science*, **44**, 29–30.

Untersteiner, N., 1961: On the mass and heat budget of Arctic sea ice. *Arch. Meteorol. Geophys. Bioklimatol., Ser. A*, **12**, 151–182, doi:10.5670/oceanog.2011.65.

Vancoppenolle, M., T. Fichefet, and C. M. Bitz, 2006: Modeling the salinity profile of undeformed Arctic sea ice. *Geophys. Res. Lett.*, **33**, L21501, doi:10.1029/2006GL028342.

Vivier, F., J. K. Hutchings, Y. Kawaguchi, T. Kikuchi, J. H. Morison, A. Lourenco, and T. Noguchi, 2016: Sea ice melt onset associated with lead opening during the spring/summer transition near the North Pole. *J. Geophys. Res. Oceans*, **121**, 2499–2522, doi:10.1002/2015JC011588.

Wadhams, P., 2000: *Ice in the Ocean*., Gordon and Breach, London, 364 pp.

Yamamoto-Kawai, M., F. A. McLaughlin, E. C. Carmack, S. Nishino, K. Shimada, and N. Kurita, 2009: Surface freshening of the Canada Basin, 2003–2007: River runoff versus sea ice meltwater. *J. Geophys. Res.*, **114**, C00A05, doi:10.1029/2008JC005000.

Yang, J., 2006: The seasonal variability of the Arctic Ocean ekman transport and its role in the mixed layer heat and salt fluxes. *J. Clim.*, **19**(20), 5366–5387. doi:10.1175/JCLI3892.1.

Zhang, J., R. Lindsay, and A. Schweiger, 2013: The impact of an intense summer cyclone on 2012 Arctic sea ice retreat. *Geophys. Res. Lett.*, **40**, 720–726, doi:10.1002/grl.50190.

THIS PAGE INTENTIONALLY LEFT BLANK

INITIAL DISTRIBUTION LIST

1.   Defense Technical Information Center
        Ft. Belvoir, Virginia

2.   Dudley Knox Library
        Naval Postgraduate School
        Monterey, California